Unconstrained Iris Recognition

Mustafa Moh'd Husien AlRifaee

This thesis is submitted in partial fulfilment of the requirements

for the degree of Doctor of Philosophy.

School of Engineering and Sustainable Development

De Montfort University, UK.

September 2014

Dedication

This effort is dedicated to

My Father Mohammad Al-Rifaee

My Mother Wesal Mustafa

My beloved wife Rawan Qwadees

Acknowledgment

First, I would like to express my appreciation to my supervisor Prof. Raouf Hamzaoui for his support during my PhD research and for his helpful guidance. Also the fruitful discussions during the research and the writing period with my second supervisors Prof. Marwan Al-Akaidi and Dr. Ismail Jannoud should be acknowledged.

Many thanks also go to Dr. Proença Proença for his cooperation and helpful comments. Finally, the greatest appreciation goes to Al-Zaytoonah University for allowing me to use the university resources for testing the proposed methods over several databases.

Abstract

This research focuses on iris recognition, the most accurate form of biometric identification. The robustness of iris recognition comes from the unique characteristics of the human, and the permanency of the iris texture as it is stable over human life, and the environmental effects cannot easily alter its shape.

In most iris recognition systems, ideal image acquisition conditions are assumed. These conditions include a near infrared (NIR) light source to reveal the clear iris texture as well as look and stare constraints and close distance from the capturing device. However, the recognition accuracy of the-state-of-the-art systems decreases significantly when these constraints are relaxed. Recent advances have proposed different methods to process iris images captured in unconstrained environments. While these methods improve the accuracy of the original iris recognition system, they still have segmentation and feature selection problems, which results in high FRR (False Rejection Rate) and FAR (False Acceptance Rate) or in recognition failure.

In the first part of this thesis, a novel segmentation algorithm for detecting the limbus and pupillary boundaries of human iris images with a quality assessment process is proposed. The algorithm first searches over the HSV colour space to detect the local maxima sclera region as it is the most easily distinguishable part of the human eye. The parameters from this stage are then used for eye area detection, upper/lower eyelid isolation and for rotation angle correction. The second step is the iris image quality assessment process, as the iris images captured under unconstrained conditions have heterogeneous characteristics. In

addition, the probability of getting a mis-segmented sclera portion around the outer ring of the iris is very high, especially in the presence of reflection caused by a visible wavelength light source. Therefore, quality assessment procedures are applied for the classification of images from the first step into seven different categories based on the average of their RGB colour intensity. An appropriate filter is applied based on the detected quality.

In the third step, a binarization process is applied to the detected eye portion from the first step for detecting the iris outer ring based on a threshold value defined on the basis of image quality from the second step. Finally, for the pupil area segmentation, the method searches over the HSV colour space for local minima pixels, as the pupil contains the darkest pixels in the human eye.

In the second part, a novel discriminating feature extraction and selection based on the Curvelet transform are introduced. Most of the state-of-the-art iris recognition systems use the textural features extracted from the iris images. While these fine tiny features are very robust when extracted from high resolution clear images captured at very close distances, they show major weaknesses when extracted from degraded images captured over long distances. The use of the Curvelet transform to extract 2D geometrical features (curves and edges) from the degraded iris images addresses the weakness of 1D texture features extracted by the classical methods based on textural analysis wavelet transform. Our experiments show significant improvements in the segmentation and recognition accuracy when compared to the-state-of-the-art results.

Table of Contents

CHAPTER 1. INTRODUCTION 12

1.1 OBJECTIVES 15
1.2 CONTRIBUTIONS 16
1.3 THESIS OUTLINE 17

CHAPTER 2. BACKGROUND 19

2.1 INTRODUCTION 19
2.2 ANATOMY OF THE IRIS 19
2.3 IRIS RECOGNITION 20
2.3.1 Image Acquisition 21
2.3.2 Image Processing 22
2.3.3 Feature Extraction 29
2.3.4 Template Matching 30
2.4 IRIS RECOGNITION SYSTEMS 31
2.5 MAIN PREVIOUS EXPERIMENTS 32
2.6 APPLICATION OF IRIS RECOGNITION 37
2.7 CONCLUSION 38

CHAPTER 3. IRIS IMAGES DATABASE 39

3.1 INTRODUCTION 39
3.2 IRIS IMAGE DATABASES 39
3.2.1 CASIA Iris database 40
3.2.2 BATH Iris Database 45
3.2.3 MMU Iris Database 47
3.2.4 ICE Iris Database 47
3.2.5 WVU Iris Database 48
3.2.6 UPOL Iris Database 49
3.2.7 UBIRIS V1 Iris Database 50
3.2.8 UBIRIS V2 Database 53
3.3 IMPORTANCE OF BEING RANDOM 54
3.4 COMPARISON OF IRIS DATABASES 56
3.5 CONCLUSION 59

CHAPTER 4. IRIS SEGMENTATION 60

4.1 INTRODUCTION 60
4.2 SEGMENTATION ALGORITHMS 63
4.2.1 Daugman's Method 63
4.2.2 Camus and Wildes Method 65
4.2.3 Roche and Avilla's Method 66
4.2.4 Wildes Method 67
4.2.5 Proença Method UBIRIS.v1 69
4.2.6 Proença Method UBIRIS.v2 71

4.2.7 Iris Segmentation Techniques *75*
4.3 PROPOSED METHOD 76
4.3.1 Proposed Sclera Detection Phase *79*
4.3.2 Flow chart in Figure 39. ..... *80*
4.3.3 Outer Ring Segmentation Phase (Iris-Sclera) *83*
..... *83*
4.3.4 Flow chart of Figure 42 ..... *84*
4.3.5 Inner Ring Segmentation Phase (Iris-Pupil) *87*
4.4 EXPERIMENTAL RESULTS 89
4.5 CONCLUSION 97

CHAPTER 5. FEATURE EXTRACTION 98

5.1 INTRODUCTION 98
5.2 VISIBLE WAVELENGTH IRIS IMAGES 99
5.3 IRIS FEATURE EXTRACTION TECHNIQUES 100
5.3.1 Daugman's Method *100*
5.3.2 Wildes Method *102*
5.3.3 Wavelet Packets *103*
5.3.4 Other Iris Encoding Methods *105*
5.4 PROPOSED METHOD 107
5.4.1 Curvelet *109*
5.4.2 Description of Curvelet Transform *112*
5.5 ROTATION INVARIANCE 116
5.5.1 Related Work *117*
5.5.2 Proposed Rotation Invariance Method *122*
5.6 CURVELET IMPLEMENTATION 123
5.7 MATCHING 125
5.8 EVALUATION AND EXPERIMENTAL SETTING 127
5.8.1 UBIRISv.1 ..... *128*
5.8.2 UBIRISv.2 ..... *132*
5.9 CONCLUSION 139

CHAPTER 6. CONCLUSION AND FUTURE WORK 140

6.1 CONCLUSION 140
6.2 LIMITATIONS 142
6.3 FUTURE WORK 142

REFERENCES 145

TABLE OF FIGURES

FIGURE 1 ANATOMY OF THE HUMAN EYE [40] 20
FIGURE 2 SEGMENTED IRIS USING DAUGMAN [11] METHOD 22
FIGURE 3 RUBBER SHEET MODEL (A) SEGMENTED IRIS, (B) RADIAL AND ANGULAR RESOLUTION (C) RECTANGULAR IMAGE 26
FIGURE 4 NOISE IN A NORMAL IRIS IMAGE (1. EYELASHES, 2. LIGHT REFLECTION, 3. SPECULAR REFLECTION, 4. EYELIDS, 5. PUPIL). 28
FIGURE 5 ADDITIONAL STEPS TO IMPROVE THE CURRENT IRIS RECOGNITION SYSTEMS [37] 33
FIGURE 6 CASIA-IRIS V1 (A) CAPTURING DEVICE, (B) CAPTURED IMAGE [40] 41
FIGURE 7 CASIA-IRIS V2 DEVICE 1 (A) IMAGING DEVICE (B) RESULT IMAGE [40] 41
FIGURE 8 CASIA-IRIS V2 DEVICE 2 (A) IMAGING DEVICE (B) RESULT IMAGE [40] 42
FIGURE 9 SAMPLES FROM CASIA-IRIS V3 INTERVAL [40] 43
FIGURE 10 SAMPLES FROM CASIA-IRIS V3 LAMP [40] 43
FIGURE 11 SAMPLES FROM CASIA-IRIS V3 TWINS [40] 43
FIGURE 12 CASIA-IRIS V4 DISTANCE (A) IMAGING DEVICE (B) RESULT IMAGE [40] 44
FIGURE 13 CASIA-IRIS V4 THOUSAND IMAGING DEVICE [40] 44
FIGURE 14 SAMPLES FROM CASIA-IRIS V4 SYN [40] 45
FIGURE 15 SAMPLES FROM BATH IRIS DATABASE [41] 46
FIGURE 16 BATH DATABASE FRAMEWORK [42] 46
FIGURE 17 SAMPLES IRIS IMAGES FROM MMU DATABASE [43] 47
FIGURE 18 SAMPLES IRIS IMAGES FROM ICE DATABASE [44] 48
FIGURE 19 SAMPLES IRIS IMAGES FROM WVU DATABASE [45] 49
FIGURE 20 SAMPLE FROM UPOL IRIS DATABASE [46] 49
FIGURE 21 UBIRIS V1 FRAMEWORK (A) UNDER ARTIFICIAL LIGHT SOURCE (B) UNDER SUN LIGHT SOURCE [47] 51
FIGURE 22 SAMPLES FROM UBIRIS V1 IRIS DATABASE [47] 52
FIGURE 23 SAMPLES FROM UBIRIS V2 IRIS DATABASE [48] 54
FIGURE 24 HAMMING DISTANCE AND EQUIVALENT FALSE MATCH [11] 55
FIGURE 25 SEGMENTED IRIS IMAGES 60
FIGURE 26 NIR IMAGE 61
FIGURE 27 VISIBLE WAVELENGTH IMAGE 61
FIGURE 28 (A) VISIBLE WAVELENGTH, (B) NIR [55] 62
FIGURE 29 PIXELS WITH MINIMUM INTENSITY VALUES [7]. 64
FIGURE 30 BEFORE AND AFTER CONTRAST ENHANCEMENT 65
FIGURE 31 EDGE MAP [6]. 68
FIGURE 32 A) INPUT IMAGE, B) EDGE MAP, WITH ONE EDGE ACT AS A CENTRE TO DRAW A CIRCLE WITH R RADIUS, C) DARK POINT REPRESENTS THE MAXIMUM INTERSECTION, D) THE CORRECT CENTRE WITH THE PRESENCE OF NOISE 69
FIGURE 33 PROENÇA AND ALEXANDRE SEGMENTATION METHOD FOR UBIRIS V1 [58] 69
FIGURE 34 MINIMAL INTENSITY RANGE [58]. 71
FIGURE 35 PROENÇA'S SEGMENTATION METHOD FOR UBIRIS V2 [57]. 72
FIGURE 36 A) HUE, B) CHROMATIC BLUE, C) CHROMATIC RED [57] 73
FIGURE 37 THE PROPORTION OF SCLERA IN ALL DIRECTION (A),(B)AND (C) FOR A STRAIGHT EYE IMAGE, (D),(E) AND (F) FOR GAZE DIVATED EYE [57]. 74
FIGURE 38 COARSE TO FINE SEGMENTATION [57] 75
FIGURE 39 FLOW CHART FOR SCLERA DETECTION 79

FIGURE 40 SCLERA DETECTION....81
FIGURE 41 SCLERA DETECTION FROM NOISY IRIS IMAGE....82
FIGURE 42 FLOW CHART FOR OUTER RING SEGMENTATION....83
FIGURE 43 RED COLOUR INTENSITY FOR DIFFERENT IRISES CATEGORIES....84
FIGURE 44 SEGMENTATION OUTPUT, BEFORE FILTER (LEFT), AFTER FILTER (RIGHT)....86
FIGURE 50 FLOW CHART FOR INNER IRIS SEGMENTATION....87
FIGURE 46 (A) ORIGINAL IMAGE, (B) HUE, (C) SATURATION, (D) VALUE, (E) MASKED IMAGE AND (F) FILTERED IMAGE.....88
FIGURE 47 OUTPUT OF THE PROPOSED SEGMENTATION ALGORITHM.....89
FIGURE 48 ACCURATE (LEFT) AND INACCURATE (RIGHT) SEGMENTATION. THE UPPER TWO IMAGES REPRESENT DAUGMAN'S METHOD AND THE LOWER IMAGES REPRESENT OUR SEGMENTATION METHOD....92
FIGURE 49 (A) MANUALLY SEGMENTED (NICE.II DATABASE), (B) AUTOMATICALLY SEGMENTED (OUR METHOD) FOR THE SAME IMAGE. 93
FIGURE 50 EXAMPLE OF RETINEX FILTER....95
FIGURE 51 NON-CIRCULAR IRIS IMAGE....96
FIGURE 52 PHASE INFORMATION [21] 102
FIGURE 53 WILDE'S PYRAMID....103
FIGURE 54 CURVELET COEFFICIENTS (A AND B) REPRESENT ZERO COEFFICIENTS WHILE (C) REPRESENTS A DISCRIMINATING COEFFICIENT [81] 111
FIGURE 55 WAVELET (LEFT) AGAINST CURVELET (RIGHT) [81] 111
FIGURE 56 (A) ORIGINAL IMAGE, (B) CURVELET COEFFICIENTS 112
FIGURE 57 CURVELET SHEAR [81] 113
FIGURE 58 CURVELET SCALES AND FREQUENCY DISTRIBUTION 114
FIGURE 59 WEDGES (SHEARS) ORIENTATIONS....115
FIGURE 60 MIRROR EXTENSION [82] 115
FIGURE 61 WRAPPING....116
FIGURE 62 BIT SHIFT PROCESS IN DAUGMAN'S SYSTEM....118
FIGURE 63 PLOTS OBTAINED BY MOTION ESTIMATION BETWEEN TWO NORMALIZED IMAGES (A) MATCH (B) NON-MATCH [91] 120
FIGURE 64 FREQUENCY SPECTRUM COVERAGE OF CURVELET USING FOUR SUB-BANDS [62]. 122
FIGURE 65 DETECTED IRIS CORNERS 123
FIGURE 66 NORMALIZED IRIS....123
FIGURE 67 RECONSTRUCTING IMAGE FROM CURVELET COEFFICIENTS 125
FIGURE 68 FRR AND FAR FOR UBIRISV.1 DATABASE 130
FIGURE 69 THRESHOLD FOR FRR AND FAR....130
FIGURE 70 CURVELET COEFFICIENTS 135
FIGURE 71 BEFORE LAPLACIAN (LEFT), AFTER LAPLACIAN (RIGHT)....136
FIGURE 72 TWO IMAGES FOR THE SAME IRIS UNDER DIFFERENT IMAGING CONDITIONS....136
FIGURE 73 FRR AND FAR FOR UBIRISV.2 DATABASE 137
FIGURE 74 SEGMENTED IRIS....143
FIGURE 75 COMPLETE UNCONSTRAINED IRIS RECOGNITION SYSTEM....161
FIGURE 76: (A) ORIGINAL IMAGE, (B) HUE, (C) SATURATION, (D) VALUE, (E) MASKED IMAGE AND (F) FILTERED IMAGE.....165
FIGURE 76: A, B, C AND D REPRESENT THE POINTS $x1, y1, x2, y2, x3, y3, x4, y4$ RESPECTIVELY. 165
FIGURE 77: POINTS COORDINATE E ($x5, y5$), F($x6, y6$), G$x7, y7$ AND H$x8, y8$....168
FIGURE 78: (A) SAMPLE IMAGES FROM UPOL, (B) UBIRISV.1, (C AND D) UBIRISV.2. 168

FIGURE 79: OUTPUT OF THE PROPOSED SEGMENTATION ALGORITHM, IMPLEMENTED IN MATLAB. 169
FIGURE 80 THE EXCLUSION OF EYELASHES.....172
FIGURE 82 176
FIGURE 83 177

Table of Tables

TABLE 1 IMAGE QUALITY IN UBIRIS V1 DATABASE [14] 52
TABLE 2 COMPARISION OF FREE IRIS DATABASE.....56
TABLE 3 HETEROGENEITY OF IRIS DATABASES 58
TABLE 4 COMPARISON OF SEGMENTATION TECHNIQUES FOR UPOL DATABASE.....90
TABLE 5 COMPARISON OF SEGMENTATION TECHNIQUES FOR UBIRISV.1 DATABASE 90
TABLE 6 COMPARISON OF SEGMENTATION TECHNIQUES FOR UBIRISV.2 DATABASE 93
TABLE 7 CALCULATED PIXEL RESOLUTION ACCORDING TO IMAGING DISTANCE 108
TABLE 8 2D TRANSFORMS AND THEIR FEATURES 110
TABLE 9 RECOGNITION RATE UBIRIS V1 128
TABLE 10 UBIRISV.1 FRR AND FAR.....129
TABLE 11 RECOGNITION RATE UBIRISV.2 DATABASE 132
TABLE 12 UBIRISV.2 FRR AT FAR= 0.01.....133
TABLE 13 FRR FOR UBIRISV.2 DATABASE AT FAR= 1%.....136
TABLE 14 RECOGNITION ACCURACY ON MANUALLY SELECTED IMAGES.....138
TABLE 15 RUNNING TIME FOR CURVELET TRANSFORM VIA WRAPPING.....173

List of Abbreviations

CASIA	Chinese Academy of Science - Institute of Automation
BATH	University of Bath iris database
EER	Equal Error Rate
FAR	False Acceptance Rate
FRGC	Face Recognition Grand Challenge database
FRR	False Rejection Rate
HSV	Hue Saturation and Value
ICE	Iris Challenge Evaluation
IOM	Iris On the Move
MMU	Multimedia University iris database
NICE	Noisy Iris Challenge Evaluation
NIST	National Institute of Standards and Technology
RGB	Red Green and Blue
ROC	Receiver Operating Characteristics
SVM	Support Vector Machines
UBIRIS	University of Beira Iris database
UPOL	University of Palackeho and Olomouc
WVU	West Virginia University iris database

Chapter 1. Introduction

Whenever people pass through airports, use their credit cards, login to computers or pass through high security areas, their identities must be verified. In some cases this is done with a username and password but in other cases personal identification cards are used. However, usernames and passwords can be forgotten, identity cards can be lost or stolen. This makes it necessary to improve the methods of human identification and to develop new techniques that are more reliable and more accurate than the traditional ones.

Recent advances in science and technology have made it possible to identify individuals through their biometrics. Currently, there are various applications where biometric identification is used. First, it can be used to control access to restricted areas. Second, it can be used in passenger control at airports, as well as in border control. Third, it is applied in database access and financial services.

Recently, the border agencies in the UK and Australia have issued new biometric identity cards and passports based on iris, fingerprint or face recognition technologies. The combination of the iris and fingerprint techniques speeds up the security checking process at some airports [1].

Biometric technology has also been applied in the field of financial services, where it has provided simplicity to customers and, at the same time, increased their security. Banking services and payments made via biometrics, for example, have proved to be much safer than traditional identification methods [2].

Furthermore, biometric identification has been invoked in access control applications, such as computer login and database access. Compared to passwords, pattern recognition techniques, such as iris and fingerprint recognition, provide more reliable and secure accessibility. Also, it solves the problem of users forgetting their passwords or them being hacked.

In the near future, biometric identification will offer more services to the society, and it remains a rich area for research work. A market overview [3] by the International Biometric Group (IBG) in the USA indicates that revenues from biometrics are expected to increase from $3.42 billion in 2009 to $9.37 billion in 2014. These revenues are dependent on fingerprint techniques. However, it is expected that the use of the iris, face, and hand recognition techniques will be expanded in the near future.

This research focuses on iris recognition as it is the most accurate form of biometric identification, as the human iris has 249 unique characteristics, the characteristics of the human iris are unique even in identical twins [4], and the texture of the human iris remains stable all through the human life. Moreover, the environmental effects cannot easily alter its shape (see Appendix B) or refer to [5]. In view of this, we see most high security areas like airports and military laboratories using Iris identification for authorization as well as for identification for Automated Teller Machines (ATMs) and restricted access to police evidence rooms.

In most iris recognition systems, ideal image acquisition conditions are assumed [6, 7]. Some authors have proposed relaxation of these constraints. The first method [8] proposed recognition of the iris while the subject is moving over a long distance from the acquisition

camera. The second method [9] deals with low resolution iris images. Another method [10] deals with noisy irises arising from poorly lit or blurred iris images. While these methods improve the accuracy of the original iris recognition systems, they still have segmentation problems, which can result in unacceptable FRR and FAR or in recognition failure.

Iris recognition uses a verification scenario in order to accept or reject a claim [11]. The verification process compares the acquired samples of claim with the samples of claim that were previously enrolled. When two samples match, the claim is accepted. If not, the claim is rejected.

There are four possible outcomes for the verification process.

1. True Accept: occurs if the recognition system accepts a person biometric, and the biometric image is stored in the database.
2. False Accept: occurs if the recognition system falsely accepts a person biometric, and the biometric image is not stored in the database
3. True Reject: occurs if the recognition system rejects a person biometric, and the biometric image is not stored in the database
4. False Reject: occurs if the recognition system rejects a person biometric, and the biometric image is stored in the database

Thus, there are two error rates that can be used in order to test the system accuracy: FRR and FAR, which can be summarized in a Receiver Operating Characteristics (ROC) curve

that plots FRR as a function of FAR. The point where FRR is equal to FAR is called Equal Error Rate (EER).

- FRR: is the probability that an enrolled person is not identified by the system, and it occurs only when comparing multiple versions of the iris image from the same human subject (intra-class comparison).
- FAR is the probability that an imposter is identified as an enrolled person, and it occurs only when comparing the iris image of different classes from different human subjects (inter-class comparison).
- ROC: The ROC curve plots FRR against FAR to determines the best matching threshold. The best threshold value determine the minimum dissimilarity distance between the input image and the equivalent stored template in order to be considered as a match. If the threshold is reduced, there will be fewer false non-matches but more false accepts. At the same time, a higher threshold will reduce the FAR but increase the FRR.
- EER: The EER is extracted from ROC curve, where the FRR and FAR are equal. The EER is the best way to calculate the device accuracy, and the device with the lowest EER is the most accurate.

1.1 Objectives

Light: Most of the current iris recognition systems use NIR light sources to reveal the rich texture of the captured iris images. This research aims at segmenting and recognizing the iris images captured under natural or artificial light sources.

Distance: Most of the current systems deal with high resolution iris images that have been captured through high resolution cameras and from close distances to capture enough textural features from the human iris. This research aims to extract discriminating features from degraded images captured over 4 to 8 meters.

Rotation invariance: Most of the current systems deal with images that have been captured with human subject cooperation with look and stare and without major head tilt. This research aims at recognizing the iris image without human cooperation.

1.2 Contributions

The main contributions of this thesis are:

- Comparison between the most common iris recognition systems, in terms of segmentation and classification accuracies.
- Comparison between all free available iris databases in terms of the size of database, the acquisition device, the resolution of iris images, capturing settings, light source, capturing distance and noise factors.
- A new quality assessment pre-processing step, based on the image RGB colour intensity to identify the noise factors affecting the input image. Then a modified Retinex image enhancement method is applied according to the image quality.
- Design of a robust segmentation algorithm, for sclera, iris outer ring and pupil, based on HSV, RGB and image binarization. This algorithm is suitable for iris recognition applications with non-cooperative image capturing and using visible wavelength light source.

- Use of the Curvelet transform to extract the geometrical features (curves and edges) from the degraded iris images rather than the classical methods based on textural analysis with the wavelet transform. The proposed algorithm is invariant to the rotations and the size of the iris image. This proposal is suitable for iris recognition applications where the iris images are captured over long distances (4 to 8 meters) and where the fine textural features are not clear.
- A new fast and robust features selection method to select the discriminating features from the Curvelet coefficients based on the highest reflected frequencies.
- Implementation of a complete iris recognition system.

1.3 Thesis outline

The thesis is organized as follows:

The first chapter includes motivations, aims and objectives and the main contributions.

The second chapter describes the main components of an iris recognition system.

The third chapter contains a survey of freely available iris databases with descriptions of their characteristics.

Chapter 4 gives a description of the main previous segmentation proposals and the proposed algorithm, and shows a comparison with the state of the art and the most cited techniques.

Chapter 5 explains the most common feature extraction algorithms, and the advantages of the Curvelet transform over other textural feature extraction techniques. It also contains a description of a method for rotation invariant iris recognition.

Chapter 6 concludes the thesis and proposes topics for future work.

Chapter 2. Background

2.1 Introduction

Iris recognition is the most accurate form of biometric identification. The robustness of iris recognition comes from the rich texture of the human iris, and the permanency of the iris texture as it is stable over human life. The history of iris recognition starts in the middle of the 19th century by Alphonse Bertillon, when he used the eye colour as an identifier. However, the main idea of using the iris pattern was proposed to Prof Daugman, who embarked on developing a high-confidence iris recognition system [11].

This chapter describes the main components of an iris recognition system, with brief description on the most cited iris recognition methods.

2.2 Anatomy of the Iris

The human iris, which is coloured layer (brown, black, green, blue, hazel or grey) in the eye, is responsible for controlling the size of the pupil diameter via two muscles called the dilator and sphincter, and thus the amount of light reaching the retina (Figure 1). The larger the pupil becomes, the more light can enter.

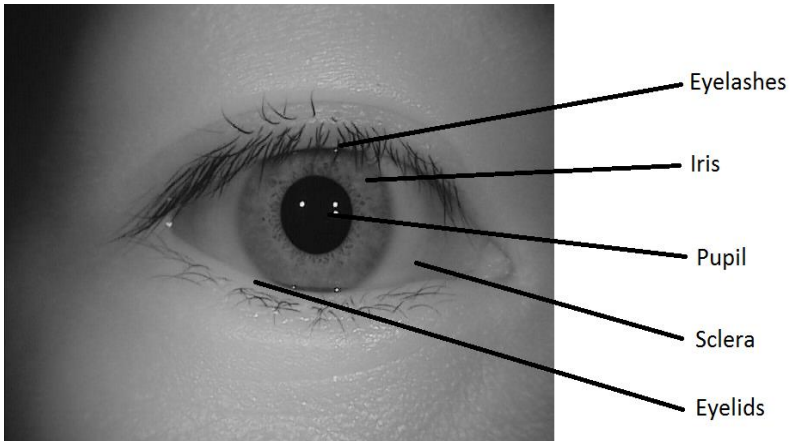

Figure 1 Anatomy of the human eye [40]

The human iris has very rich patterns of colour pigments, ridges and furrows. The details of human iris texture are determined randomly through the foetal development of the human eye, and they differ from one person to another and even between the left and the right eyes of one individual. The most important issue is that environmental effects cannot alter the texture or shape of the human iris [12].

2.3 Iris Recognition

The standard iris recognition process comprises of four phases. The first of these phases is the image capturing, which describes the imaging device, the light source and the capturing distance. The second phase is the image processing. This phase is further subdivided into two steps, the image segmentation and normalization. In the segmentation process the area of interest (iris) is cropped out from the whole eye image, and in the normalization step the doughnut shaped iris image is transformed from Cartesian coordinate to a rectangular image polar coordinate with a predefined size. Recent proposals [8] [9] [13] add another step to the recognition process known as a pre-process step to enhance the noisy input images before processing. The third phase is the feature

extraction phase, where the discriminating features of the iris are extracted from the normalized template and stored in a feature vector to be used in the fourth phase template matching for verification.

Following is a brief explanation of each of the phases of the Iris recognition process:

2.3.1 Image Acquisition

Iris image should be captured with at least 100 to 200 pixel resolution [11] with a maximum distance ranging between 15 and 46 cm to do the recognition process with a high accuracy result. All commercials iris recognition systems use NIR (Near Infrared) illumination at 700-900nm range [7] to light the human face with audio feedback to position the head so that a suitable iris image size is captured.

Other iris recognition systems use high-resolution cameras like SARNOFF, LG, PANASONIC or OKI to expand the capturing distance to 3 metres like [13]. Also, IOM system uses multiple cameras to capture the human iris from multiple angles and then select the best iris image.

To improve the image quality, some authors propose engineering the image acquisition system for good quality iris image [13], regardless of the imaging framework expenses, while others propose developing an intelligent algorithm to classify and enhance the captured images [14]. It is better to develop an intelligent algorithms for enhancements and classification rather than hardware engineering to achieve a high performance unconstrained iris recognition system, because hardware engineering may led to use large imaging equipment which is unsuitable for unconstrained conditions like iris recognition

on mobile phones or using web cams. Further explanation on all free available iris databases is presented in chapter 3.

2.3.2 Image Processing

The iris images, after being captured, will have many unwanted data like eyelids, eyelashes, sclera, pupil and some parts of the human face skin. Moreover, the size of the iris will vary according to the capturing distance, and light source also may cause a pupil dilation, which will also affect the size of the iris portion. Thus, the iris images should be segmented to obtain a useful iris region, and normalized to a predefined fixed size [7]. In image processing phase, there are two main steps, as follows:

2.3.2.1 Segmentation (Localization)

In the segmentation process inner and outer boundaries of the iris are located , and more importantly eyelashes and eyelids that cover a part of the iris region are removed [15].

Segmentation is a very important step in the recognition process because a correct region of the human iris is required for accurate matching.

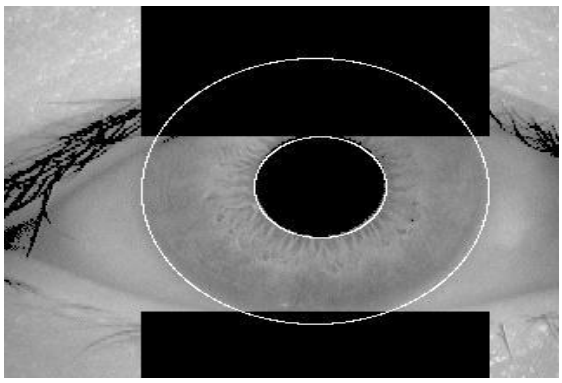

Figure 2 Segmented iris using Daugman [11] method

In this section, the main iris segmentation algorithms cited in the literature is briefly stated, and further explanation is presented in chapter 4.

1. Integro differential Operator: Daugman [11] use Integro differential operator to locate the inner and outer boundaries of the human iris as well as the upper and lower eyelids, Figure 2 show the output of Daugman segmentation method.
2. Circular Hough transform: Wildes [6, 16, 17] use Hough Transform which applies the edge detector to the iris image for generating an edge map for the iris region.
3. Discrete circular active contour: This technology is used in [18] to draw the circular iris region by moving a contour across the human iris until it reaches equilibrium, but this method fails completely if a specular reflection occurs.
4. Bisection method [19]: This method uses a bisection method to determine the centre of the pupil. The centre point then will act as a reference for detecting the inner and the outer boundaries of the iris.
5. Black hole search: In [20] the researchers search for the pupil region. Since the iris pupil is the darkest area in the human iris they use threshold segmentation to find it.

2.3.2.2 Eyelids and Eyelashes Detection

Usually eyelids and eyelashes cover a valuable texture of the iris. So, they should be detected and removed from the iris image. Daugman in [7] proposes the use of integro-differential operator to detect and segment the upper and lower eyelids by changing the contour from circular path to arc path, then in [21] Daugman introduce another technique

which describes the eyelids detection by passing a snake over the active contour based on the expansion of discrete Fourier components, Wildes in [6], as described in [22], uses a horizontal edge map followed by circular Hough transform based on a circular path with increasing radius for eyelids segmentation, another proposal as in [23] introduces eyelids detection by texture segmentation. All the stated methods achieved high segmentation accuracies in noise free iris images, but their results decreases significantly when applied to noisy images, because these methods were developed to process iris images captured under ideal conditions using infrared light source which reduces the effect of reflection noise.

For eyelashes detection, most of the methods described in the literature use a simple threshold algorithm, as the eyelashes are the darkest pixels with the lowest intensity values in the segmented images. An appropriate threshold can be calculated, and the values less than the threshold can be excluded [7] [24].

2.3.2.3 Normalization

The normalization process is used to transform the segmented doughnut shape Cartesian coordinate iris image to a fixed dimension rectangular Polar coordinate to achieve fair comparisons. The image size inconstancies is introduced by using a different light source, which causes a variant dilation level in pupil area. Moreover, a varying capturing distance also affects the dimension of the resultant iris image. Many normalization methods were used in the literature, but the most frequently cited two techniques are Daugman rubber sheet model [11], and Wildes image registration [6].

2.3.2.3.1 Daugman Rubber-Sheet

In this method, the segmented doughnut shaped iris portion is converted into a rectangular image, which can be achieved by converting the segmented portion of the iris to dimensionless pseudo-polar coordinates through a method called Homogenous Rubber Sheet Model [11].

As shown in Figure 3, it is just like drawing concentric circles of pixels from the iris image moving in from the outer circle immediately around the iris until reaching a pupil ring but instead of drawing circles of pixels, the pixel should be extracted from an oval-shaped iris and it must be put in a linear shape as a rectangle. This can be done by extracting the first upper ring of pixels in the iris at the size of iris diameter at 360° and arranging these pixels in a straight line then decreasing the diameter by one and arranging the extracted pixels in the second line and so on until reaching the pupil [7].

If the first circle of the iris has been parsed with 1° step, the width of the resultant rectangle will be 360 and the height of the rectangle will be equal to the difference in the radius size between the iris and the pupil.

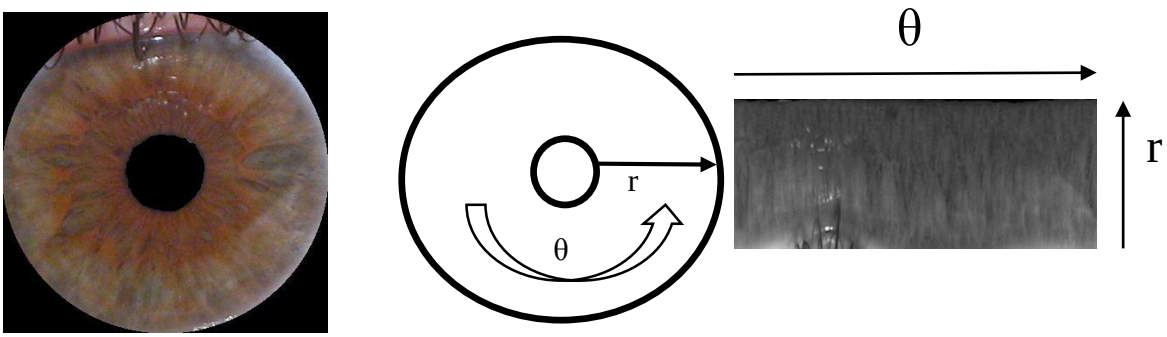

(a) **(b)** **(c)**

Figure 3 Rubber Sheet Model (a) segmented iris, (b) radial and angular resolution (c) rectangular image

The homogenous rubber sheet model is given as.

$$I\left(x\left(r,\theta\right),y\left(r,\theta\right)\right)\rightarrow I\left(r,\theta\right)$$

where

$$x\left(r,\theta\right)=(1-r)x_p(\theta)+rx_i(\theta)$$

$$y\left(r,\theta\right)=(1-r)y_p(\theta)+ry_i(\theta)$$

$I(x,y)$, is the iris image region, (x,y) is the cartesian coordinates, (r,θ) is the polar coordinats corresponds to (x,y), x_p,y_p and x_i,y_i are the coordinates of the outer and inner rings along with θ direction. Homogenous rubber sheet model algorithms can overcome the iris capturing distance problem and the pupil extension.

2.3.2.3.2 Wildes Image Registration

Wildes [6] used image registration method to transform the iris images into a fixed dimension. The author performed a geometrical wrapping process to the captured image $I_a(x, y)$, in alignment with stored image in database $I_d(x, y)$, according to the mapping function$(u(x, y), v(x, y))$. All image intensity value at $(x, y) - (u(x, y), v(x, y))$ in I_a must be close to (x, y) in I_d, in other words, the mapping function (u, v) is calculated to minimize the error function, and that can be found by

$$err = \iint_{x\,y} \left(I_d(x, y) - I_a(x - u, y - v)\right)^2 dxdy$$

The mapping function with error minimization is constrained to find the similarity transformation of coordinate (x, y) to(x', y'), such as

$$\begin{pmatrix} x' \\ y' \end{pmatrix} = \begin{pmatrix} x \\ y \end{pmatrix} - \; sR_{(\emptyset)} \begin{pmatrix} x \\ y \end{pmatrix}$$

where s is the scaling factor and R is the matrix that represents the rotation by $\emptyset$ angle.

2.3.2.4 Image Enhancement

After normalization, the iris images will have a non-uniform illumination with low contrast. These types of noises are caused by the light source intensity and position. Thus, an enhancment process is needed to minimize the effect of these noises. Li, Yunhong, and Tieniu in [17] apply a local histogram to the normalized iris template to minimize the effect of nonuniform illumination. For reflection removal, Junzhou et al [25], detects the

region with high intensity values near 255 and applies a threshold operation to remove these regions.

Other proposals like [26] prefer enhancement of the iris image using Gaussian low-pass filter, while Wildes [6] uses histogram equalization by the means of edge detection. All these methods deal with images that have been captured with human subject cooperation and using NIR light source. In visible wavelength light source, a pre-process should be applied to the input image for increasing the robustness of the recognition system. Proença and Alexandre [27] describe a new method for determining the noisy region in iris image, and they classify the noise affecting the input images into five categories: (eyelids, eyelashes, pupil, light reflection and specular reflection) as in Figure 4.

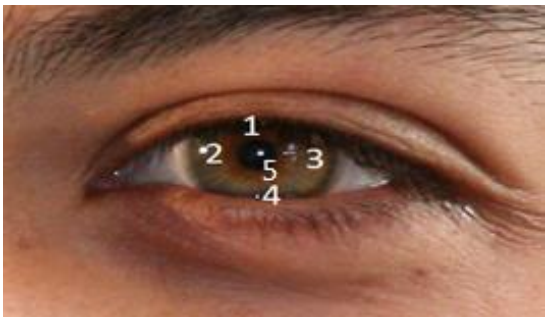

Figure 4 Noise in a normal iris image (1. Eyelashes, 2. Light reflection, 3. Specular reflection, 4. Eyelids, 5. Pupil).

However, in their paper, the authors propose that each pixel in the iris image is a feature. In this method they calculate 8 statistical measures (Angular Second Moment (ASM), Row, Column, Entropy, Energy, Contrast, Inertia, and Phase Congruency) for each pixel. These measures are calculated using Neural Network in a hidden layer. The authors used

20,000 noisy and 20,000 noise-free pixels for the machine learning and achieved good results in detecting noisy regions from the iris images.

2.3.3 Feature Extraction

In the feature extraction process special features (such as rough, smooth, silky or bumpy areas) are extracted from the normalized iris image using texture analysis techniques to generate a biometric template for better matching.

Many techniques are applied to the normalized image in the feature extraction process to extract the suitable features, which will be used in the matching stage.

1. Gabor Filter: A linear function that is derived from a mother wavelet used for edge detection. It is suitable for texture representation and discrimination. 2D Gabor filter is defined as the result of multiplying the harmonic function with Gaussian function: in this filter each pixel in the normalized image is modulated into two pits of binary code in the resulting iris template, to be used in the template matching stage [28].

2.Wavelet Transform: In wavelet transform the normalized iris region is decomposed into components with different resolutions. This transform uses a bank of filters to search for features in the image using varying window sizes and the resulting code will have both frequency and space resolutions. Different types of wavelet transform are used in iris recognition system like Daubechies, Haar, Biorthogonal and Mexican Hat wavelet [29] [30].

3. Laplacian of Gaussian filter: In this feature extraction technique the filter decomposes the iris image into an analysed shape called Laplacian pyramid, then a bank of Gaussian filters are applied to the resulting image to encode the features [6].

4.Key local variations: Key local variation techniques deals with the normalized iris image to extract its characteristics and compose it to 1D intensity signals. Then Dyadic wavelet transform is applied to count the sharp variation of the signal intensity and finally the maximum and minimum points are encoded into a feature vector then these features are converted into a binary template [26].

5. Hilbert transform: Hilbert transform extracts the information from the iris texture [31]. This technique depends on the frequencies extracted from the iris image, and the analysed frequency known as 'Emergent frequency' is formed from instantaneous phase and feature vectors from thresholding emergent frequency.

6. Discrete Cosine Transform (DCT): In this type of transform the encoding is accomplished by expressing a finite sequence of data points from the input image in term of a sum of cosine function at different frequencies [32]. Then the difference in discrete cosine coefficient is calculated to create the binary template using zero crossing technique.

2.3.4 Template Matching

The template generated from the feature extraction process should be compared with the system data base for finding the similarity between two templates (inter-class and intra-class) by using different matching algorithms [33].

In the following some of matching techniques are discussed:

1. Hamming distance: Hamming distance calculates the similarity between two binary codes from the binary image template. A value of zero will represent perfect matching, and a value near 0.5 will represent two independent irises [7].

The main advantage of Hamming distance is the fast matching process because it is operate over a binary template with X-OR comparison.

2. Weighted Euclidean distance: This calculates the similarity between two integer values in the integer image template [15].

3. Normalized correlation: This calculates the similarity between two points (pixel or dot) in a normalized iris region [6].

4.Nearest feature line: The nearest feature line method is an extended version of the nearest neighbour method. The method effectively improves the classification performance where the number of templates per class is small [15].

2.4 Iris recognition systems

Daugman [11] developed the first iris recognition system that was introduced to the market in 1993. IriScan Inc. has adopted Daugman iris recognition system, after Daugman system many other companies provide iris recognition products like Iridian Technologies, IBM, Panasonic and IrisGuard Inc [7].

The history of iris recognition starts in the middle of the 19th century, when the French physician Alphonse Bertillon used the eye colour as an identifier. However, the main idea of using the iris pattern was introduced in 1936 by eye surgeon Frank Burch [11]. This

idea was developed by Flom and Safier in 1987 [108] and was proposed to Prof Daugman, who embarked on developing a high-confidence iris recognition system [11].

Many organizations worldwide, such as Iridian, US Sandia Labs, LG, Sarno, EyeTicket, Siemens,Unisys, UK NationalPhysical Laboratory, IriScan, British Telecom, Sensar, The National Biometric Test Center of SJSU and United Arab Emirates Airport adopted Daugman iris recognition system as the system scored zero false match rates over a comparison of millions [51].

The system proposed by Daugman is able to operate very quickly because it is based on storing the 256 byte iris code in a binary format on an iris code database and the search engine is based on a Boolean X-OR comparison. Moreover, the iris code generated from the iris image has 249 degrees-of-freedom, which makes it a highly reliable system.

Many other researchers have developed new iris recognition systems after Daugman, including those systems presented in [6], [34], [35], [36] . The systems presented in this section have been designed for cooperative uses, in which the user should hold and stare to the acquisition camera at close distance and NIR light should be used. This research is dedicated to relaxing these constraints.

2.5 Main Previous Experiments

In most iris recognition systems, ideal image acquisition conditions are assumed [7]. Many techniques have been introduced for relaxing these constraints. One approach is to recognize the iris while the subject is moving over a long distance from the acquisition camera [8]. Another approach is to recognize the iris in a non-ideal situation such as noisy

images [13], bad lighting, motion blur and reflection [37]. While these approaches improve recognition accuracy, they still have low segmentation accuracy in some situations such as rotation and lighting problems, which can result in recognition failure.

Zhou, Du and Belcher [37] have improved the current iris recognition system by adding an extra step that can overcome some limitations of the systems previously used. Their main idea was to transform the commercialized iris recognition systems deployed in different secure portals for dealing with non-cooperative users rather than replacing the entire existing recognition systems.

All of the traditional iris recognition systems perform five steps in their recognition process. These steps are Image Acquisition, Segmentation, Normalization, Feature Extraction and Template Matching. The authors propose new embedded steps to improve the typical iris recognition system so that it may work in non-ideal situations. These steps are Quality Filter, Segmentation Evaluation, Quality Measure and Score Fusion.

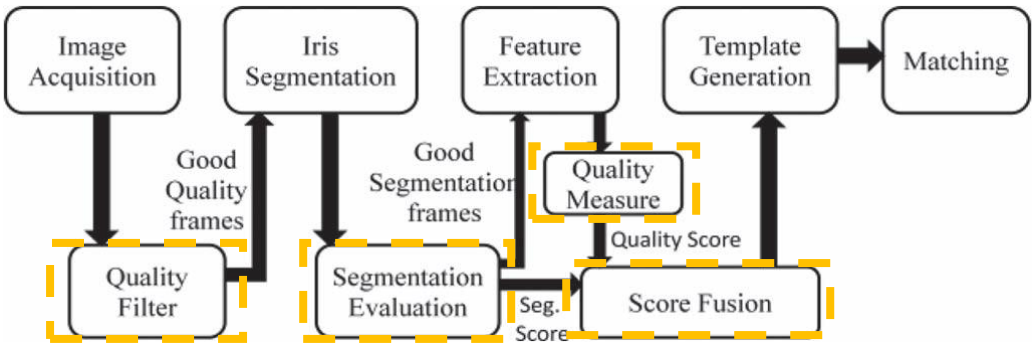

Figure 5 Additional steps to improve the current iris recognition systems [37]

As in Figure 5, the quality filter unit is used to identify and eliminate the poor quality frames from the entire captured video. Eliminating these frames helps to achieve quicker and more accurate recognition, though some of the good quality image that passes the

quality filter will result in incorrect segmentation. Thus to ensure a perfect segmentation the following three parameters should be cleared: centre of the pupil, inner/outer boundaries and the output mask. This can be done via the use of a segmentation evaluation unit, as in the quality measure unit the most suitable portion with the most distinguishable features is selected in order to achieve a perfect recognition process [37].

The segmentation score, achieved through the segmentation unit, is uncorrelated with the quality score. So the combination of both scores should be calculated in the score fusion unit to achieve the expected results. This system scores a very good result in False Rejection Rate (FRR = 2.7%) and False Acceptance Rate (FAR = 2.2%), especially in normal and bright illumination conditions.

Another proposal known as Eagle Eye iris recognition system [8] introduce a new system that deals with images captured at distance for long range identification. Eagle Eye is a multi-biometric system designed to capture the human face, and two iris images present anywhere within a large capture volume.

From the creators of Eagle Eye system point of view, two problems should be considered during the design of an iris recognition system at distance: the first one is the NIR illumination to provide a good contrast between the iris and both sclera and pupil; the second is the resolution of the iris image suitable for perfect identification, which equals 200 pixels for high quality and 100 pixels for minimum iris image quality.

The Eagle Eye system solves the illumination problem by using an array of high powered LEDs and a targeted illumination that has the move capability to target the subject. In

order to yield a suitable pixel and spatial resolution, the Eagle Eye system uses cameras with variable focal lengths and focus controls [8].

The Eagle Eye system works as follows:

The iris image enrolment is done by a mobile hand-held camera for both human eyes using NIR LED illumination to acquire images of iris at a video rate that meets the resolution standards. These images are then segmented, normalized and stored in a database. Next, for human identification, three cameras are used, one for wide Field Of View (FOV) that images and tracks people, the second with a narrow FOV that tracks human faces. The last one is used to target the iris in the face. After capturing the iris image, a segmentation process is applied followed by normalization, and then quality score followed by features encoding are applied to extract the discriminating features of the iris template to be compared with stored features from a database.

The Eagle Eye system scores a good result in the iris distance (3-6) metres and also captures volume of 3*2*3 m^3. It scores well in recognition rate of 99.96 % and false acceptance rate of 0.001 %.

The Iris On Move (IOM) system [13] explains how to reduce constraints on position and motion of the human iris by using high resolution imaging devices.

The core of the IOM system aims at solving these main limitations:

1. Capture volume (the space within which the iris must be placed)

To solve this problem, the IOM system duplicates the system's independent modules, and uses a modified focal length with magnification lens to increase the capture volume up to 70 cm.

2. Standoff distance (distance between iris and acquisition system)

IOM uses COTS camera type PIER 2.3 that can acquire 100 pixel resolutions from 3 metres distance.

3. Verification time (time needed to acquire good quality iris)

To speed up the process, specialized image processing hardware is used.

4. Iris resolution (spatial resolution of iris; between 100 - 200 pixel)

Here a high resolution (COTS) video camera that provides 100 pixels iris region - type PULNIX TM-400 CM - was used.

5. Illumination (light needed to identify the regions of the iris)

The IOM system uses strobe illumination and synchronizes the strobe to the start of the camera frame (the light used in IOM is high power LEDs).

The IOM system, through experiments, achieves the desired scores, but the main problem has not solved completely because the human subject must cooperate with this system and should stare directly into the camera. Furthermore, if the human gaze deviated, the system will not segment the iris correctly.

Vatsa, Singh and Noore [38] introduce a different proposal, where a non-ideal iris image is segmented in two steps, firstly they apply conventional segmentation algorithms on the

input images to detect inner/outer boundaries, and the second step is to detect the exact regions of the non-circular iris and pupil by using Mumford-Shah algorithms [109].

Different enhancement algorithms are then applied to get multiple enhanced iris images. Here, Support Vector Machine (SVM) learning algorithms select locally enhanced regions with the best quality from a global enhanced image and then combines these regions in a single high quality iris image.

"New features are extracted from the high quality image; the first being global texture features that are extracted using 1-D log polar Gabor transform, and the second being the local topological feature extracted by Euler Number. When features are extracted an intelligent fusion algorithm (2*v*SVM) combines the texture and topological scores to reduce FRR, while maintaining low FAR" [38]. Finally an indexing algorithm is applied to enable fast and accurate identification. It is better to use more than one technique to extract the features of any given pattern, but this would also consume more time, and therefore is not suitable for real time recognition.

2.6 Application of Iris Recognition

Iris recognition as a biometric identification has enormous potential for security in many fields. Recently iris recognition has been applied in airline travel, border security check (UAE Dubai, UK Heathrow and USA Dulles airports), bank customer ID (Cairo Amman Bank). Moreover, the iris recognition is used for identifying immigrants, access to highly restricted areas (US Military), police evidence room (USA) and ATM (Bank United in Houston) [110].

2.7 Conclusion

The iris recognition process follows the standard pattern recognition paradigm which consists of four phases as follows

1. Image Acquisition
2. Image Processing
    - Segmentation
        - Outer Ring (Iris)
        - Inner Ring (Pupil)
        - Eyelids and Eyelashes
    - Normalization
3. Feature Extraction
4. Template Matching

These steps form the standard iris recognition system, which operates over high quality images, captured under NIR light source with human subject cooperation. To improve the performance of the recognition system that operates on noisy images taken under visible wavelength light source, additional steps might be included like image enhancement, segmentation quality assessments and discriminating features selection.

Chapter 3. Iris Images Database

3.1 Introduction

In this chapter we will introduce all types and characteristics of human iris databases, which have been created for research purposes and experiments. All the databases that will be described in this chapter are public and freely available on the internet. In the following subsections, the characteristics of seven different iris databases will described, then a comparison between all databases in term of capturing device, image resolution, light source and noise types.

3.2 Iris image Databases

The biometric process encompasses an automated method of recognizing human individuals, based on their biological characteristics. In the past thirty years, the field of biometric recognition gained the interest of many researchers, and several proposals have been introduced. While these proposals need to be proved, a large number of tests over a large number of subjects must be performed. So, it is not realistic for researchers to collect their own dataset, due to its difficulties that this could imply. Also, for a robust comparison, different proposals should be implemented over the same dataset. Therefore, a benchmark database is necessary and cannot be sacrificed for the sake of recognition development.

3.2.1 CASIA Iris database

It is the first freely available iris database for researchers, produced by the Chinese Academy of Science - Institute of Automation [40]. The first versions of CASIA iris databases utilize ideal acquisition environment, with stop and stare, at a close distance and use NIR (Near Infrared) light sources, which simulate the same conditions that have been proposed and used by Daugman's iris recognition system.

From the date of CASIA database creation, the Chinese Academy of Science produced four versions of CASIA databases as follows

1. **CASIA-Iris V1:** This version contains 756 iris images from 108 human subjects, each eye image has seven different classes divided into two sessions, training session-1 (3 images) and testing session-2 (4 images). The images in CASIA-Iris V1 have been captured using homemade iris camera, with eight circularly fitted NIR 850mn illuminators [40]. Before releasing the database to the public, and to compensate the effect of specular reflection, the area of the pupil is replaced with a constant intensity black circle. All the images are stored in format of bmp at 320*280 resolutions. Figure 6 shows the capturing framework for CASIA database.

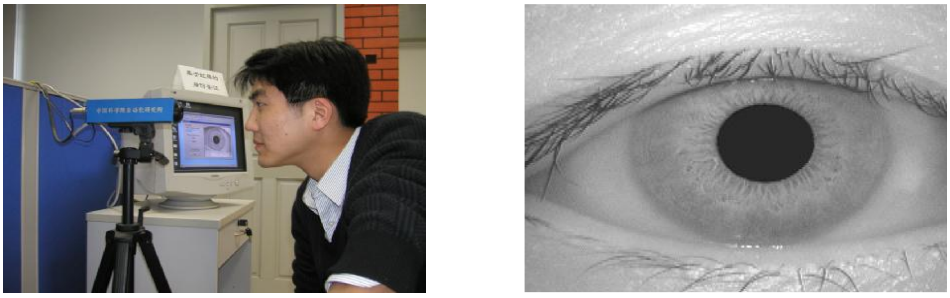

(a) **(b)**

Figure 6 CASIA-Iris V1 (a) capturing device, (b) captured image [40]

2. **CASIA-Iris V2:** This database contains 2400 images [40], divided into two subsets captured by two different devices. The first 1200 images were captured by Irispass-h device developed by OKI, and the other 1200 images were captured by CASIA-Iris cam developed at the Chinese Academy of Science. Each iris image has 60 different classes, all images are stored in bmp format at 640*480 resolution. Figure 7 and Figure 8 shows the imaging devices used to capture the iris images in CASIA V2 database.

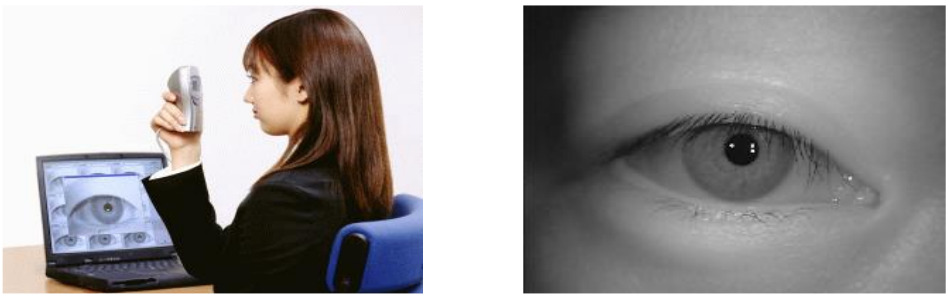

(a) **(b)**

Figure 7 CASIA-Iris V2 Device 1 (a) imaging device (b) result image [40]

(a) **(b)**

Figure 8 CASIA-Iris V2 Device 2 (a) imaging device (b) result image [40]

1. **CASIA-Iris V3:** This is the first CASIA database that introduced noise factors. It contains a total of 22,034 iris images collected from 700 humans. The database is divided into 3 subsets. The Interval data subset contains 2,639 images with very rich texture at a very close distance and lighted with an array of LED NIR light source, all images are stored in jpg format of 320*280 resolutions.

   The Lamp subset contains 16,212 iris images with visible light on-off factor, which will cause the dilation in pupil size and a non-linear deformation in the captured images, images are stored in format of jpg and 640*480 resolution. Finally, the twins data subset which contains 3,183 images captured from 100 pairs of twins during the annual twins festival in Beijing, all images are stored in jpg format at 640*480 resolutions. Figure 9, Figure 10 and Figure 11 shows sample images from CASIA V3 Interval, Lamp and Twins respectively.

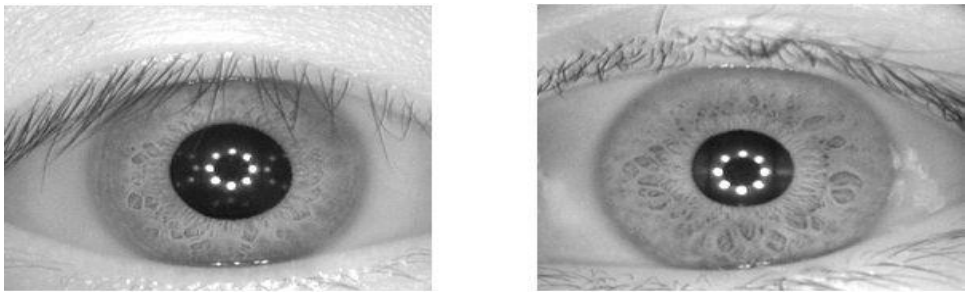

(a) (b)

Figure 9 Samples from CASIA-Iris V3 Interval [40]

(a) (b)

Figure 10 Samples from CASIA-Iris V3 Lamp [40]

(a) (b)

Figure 11 Samples from CASIA-Iris V3 Twins [40]

2. **CASIA-Iris V4:** Early iris recognition systems deal with iris images captured with human subject constrains, while current research contributions are dedicated to relax these constrains [40]. Therefore, CASIA started working to produce a new

iris images database which contains images captured on subject moving, over a distance and with poor quality under the name of CASIA-Iris V4.

CASIA-Iris V4 is an extension to CASIA-Iris V3 with thee more subsets. The first one is called CASIA-Iris-Distance. In this dataset, the iris images have been captured over 3 metres distance and while the subject is moving. The framework is shown in Figure 12 taken from CASIA website [40], the database contains 2576 images with resolution of 2352*1728.

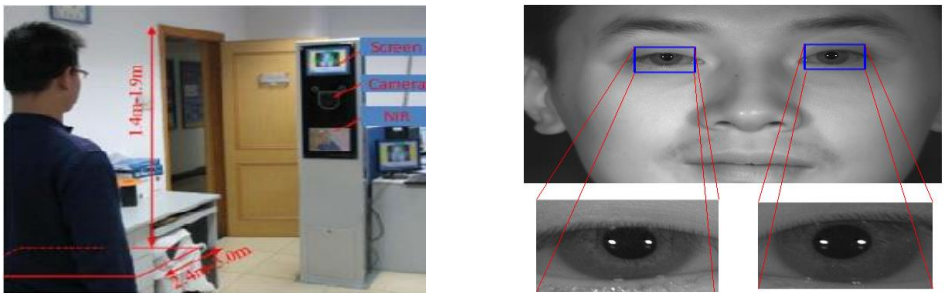

(a) (b)

Figure 12 CASIA-Iris V4 Distance (a) imaging device (b) result image [40]

The second set is called CASIA-Iris-Thousand (Figure 13). This dataset uses IKEMB-100 dual camera with friendly interface, and the output image reveals texture as "what you see is what you get"

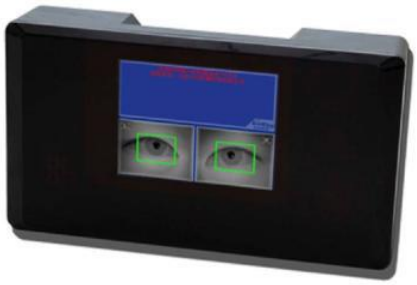

Figure 13 CASIA-Iris V4 Thousand imaging device [40]

The bounding box around the eye shown in the previous fig, tells the human subjects to adjust their positions to get clearer images. This database contains 20,000 images at resolution of 640*480.

The third set, called CASIA-Iris-Syn (Figure 14), contains 10,000, with resolution of 640*480 synthesized images from CASIA-Iris V1 using the process described in [40]. This process makes the iris texture more realistic and enables it to overcome the noise introduced from motion blur, rotation and deformation.

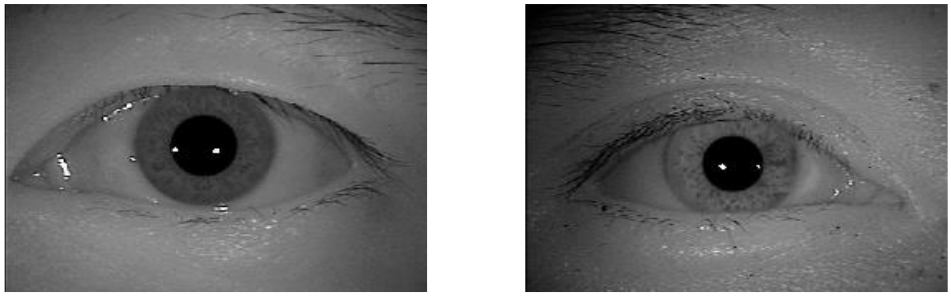

(a) (b)

Figure 14 Samples from CASIA-Iris V4 Syn [40]

3.2.2 BATH Iris Database

This database is another example of NIR images databases [41]. This database has been created at the University of Bath by Smart Sensor Limited. Bath iris database consists of 32,000 high quality iris images, captured from 800 mixed ethnic subjects (1600 classes, for left and right eye) with a pixel resolution of 1280×960. Figure 15 shows samples images from Bath database.

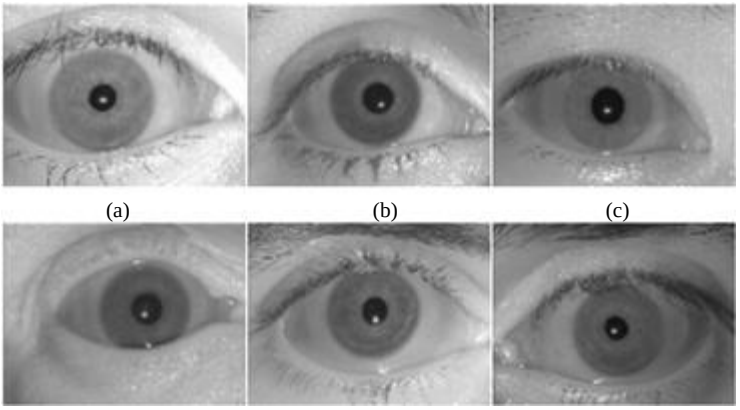

Figure 15 Samples from Bath iris database [41]

Smart Sensor Limited used the ISG LW-1.3-S-1394 1.3 megapixel camera, placed over an adjustable stand as shown in Figure 16 that have been copied from [42], with array of LED's to capture 200 frames from each subject. Based on the frame quality the best 20 frames are selected to be stored in the database. All the subjects must place their chins on a rest stand over short distance from the camera lens, then the camera operator adjust the lens to get the best and the maximum iris texture into focus.

Figure 16 Bath database framework [42]

Although the Bath database contains non-ideal images, like images with deviated gaze, occluded with eyelids/eyelashes and focus blur, still the majority of images have homogenous characteristics, and not suitable for the term of unconstrained recognition.

3.2.3 MMU Iris Database

The Multimedia University has introduced two iris databases [43]. The first one is MMU1 database which comprises of 450 images, captured by a semi-automated camera dedicated for iris capturing (LG IrisAccess 2200) at 7-25 cm distance range, and the second database is MMU2, consisting of 995 images, collected by Panasonic BM-ET100US camera at a distance range of 47-53 cm from the human subject. The images in MMU database have been collected from 100 volunteers of different ages and nationalities, with each volunteer contributing 5 images from each eye.

(a) (b) (c) (d)

Figure 17 Samples iris images from MMU database [43]

The iris images in MMU database are homogenous, and have been taken using an NIR light source at a close distance with human subject cooperation, introducing eyelashes obstruction and eye rotation as shown in Figure 17.

3.2.4 ICE Iris Database

In 2005, the NIST (National Institute of Standards and Technology) managed a project under the title of ICE (Iris Challenge Evaluation) [44] to improve and advance the iris recognition technology that supports the current iris recognition systems in the US government. The improvements were made by distributing the problems introduced by exciting iris recognition systems to a potential participant. In 2006, the NIST facilitated

the opportunity for competition between participants in a large scale and independent evaluation for testing their algorithms on new larger database using their own frameworks.

ICE database contains 2954 images, acquired with look and stair, close distance and NIR light source constrains. This database introduces standard noise factors related to poor focus and occlusion of eyelashes (Figure 18). Like the previously described databases. The images are not appropriate for the evaluation of unconstrained iris recognition systems.

(a) (b) (c)

Figure 18 Samples iris images from ICE database [44]

3.2.5 WVU Iris Database

WVU iris database was developed at West Virginia University [45]. 380 human subjects contribute three to six images each to produce a database of 1852 iris images, and the acquisition process was performed through a hand-held camera called OKI IrisPass-H. As shown in Figure 19, the iris images in WVU database have heterogeneous characteristics and they introduce several types of noise factors, such as off-angle, obstructions, poor focus, environment light reflections and rotated images.

The less constrained imaging conditions, makes the WVU iris database a challenging dataset for testing unconstrained iris recognition algorithms, but still the capturing framework uses the NIR light source.

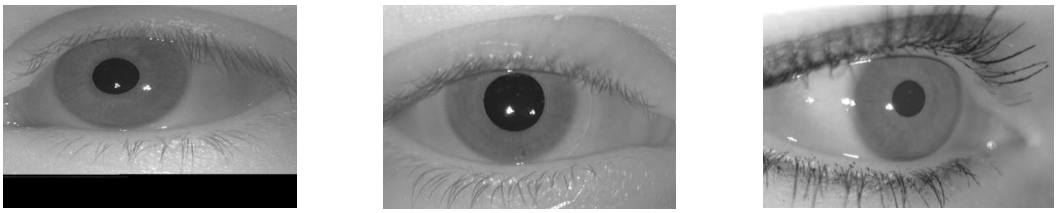

(a) (b) (c)

Figure 19 Samples iris images from WVU database [45]

3.2.6 UPOL Iris Database

The UPOL (University of Palackeho and Olomouc) [46] is the first database that used imaging framework with a visible wavelength light source. The database comprises of 384 images collected from 64 human subjects, with each subject contributing 6 images (3 from left eye and 3 from right eye), and a SONY DXC-950P 3CCD camera connected to TOPCON TRC50IA optical device was used for iris capturing, at resolution of 576×768 RGB 24-bit colour depth (Figure 20).

Figure 20 Sample from UPOL iris database [46]

The images were captured at a close distance with human subject cooperation. Even the visible wavelength light source was placed in a position that does not affect the human iris, and, therefore, the output was extremely noise free images and has homogeneous characteristics, which makes this database unsuitable for testing the unconstrained iris recognition algorithms.

In this research the proposed algorithms was tested on UPOL database before testing them on noisier datasets just for finding the maximum threshold values used in the segmentation process. And minimum numbers of features were used in template match process, and the accuracy was extremely high as it can be seen in the next chapters.

3.2.7 UBIRIS V1 Iris Database

The reason behind the creation of UBIRIS database [47] is the need of a new noisy iris images dataset, which simulates the less constrained environment in the capturing framework that will be used as a tool for the development of robust recognition proposals.

In contrast to the previously described noise free iris databases apart from WVU database, the UBIRIS database is the noisiest one, which introduces new noise factors caused by (1) motion blur and rotated iris images from moving subjects, (2) poor focus images, (3) obstruction of eyelids and eyelashes, (4) specular and light reflection from visible wavelength light source, and finally (5) closed eye iris images. These noise factors make the UBIRIS database an appropriate set for the developments of unconstrained iris recognition algorithms.

The UBIRIS database, which was created at the University of Beira in 2004, contains 1877 iris images contributed from 241 human subjects, collected through two different sessions with a two weeks interval, using Nikon E5700v1.0 camera, 71mm focal length, 1/30s exposure time. The output image is RGB at 2560×1704 resolution, 300 dpi vertical and horizontal resolution, with a colour depth of 24 bit. The image size was reduced to 300×400 grey scale to reduce the database size so it can be easily uploaded and downloaded from the web. As shown in Figure 21, the first session contains images with minimal noise factors, especially those related to reflection, contrast and luminosity factors. The second session involve more noise factors caused by natural light source, a sample of UBIRISv.1 images is given in Figure 22.

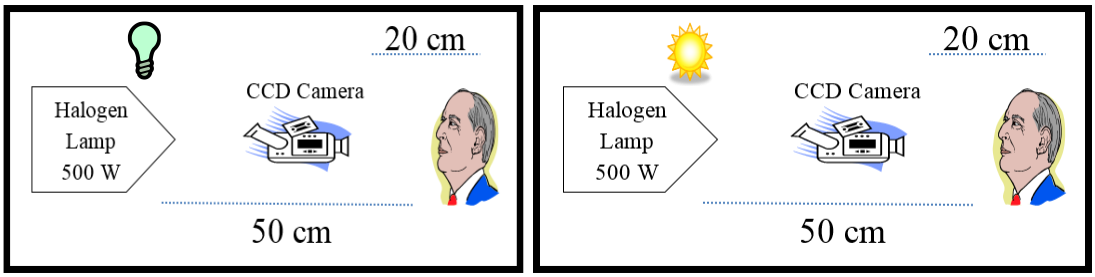

(a) (b)

Figure 21 UBIRIS V1 framework (a) under artificial light source (b) under sun light source [47]

Images in UBIRIS database as stated in Table 1 were manually classified according to three parameters (Focus, Reflection and Visible Iris), and classified as Good, Average and Bad as follows [14]:

Table 1 Image quality in UBIRIS V1 database [14]

Parameter	Good	Average	Bad
First Session			
Reflection	76.10 %	16.51 %	7.39 %
Focus	78.52 %	19.09 %	1.99 %
Visible Iris	43.65 %	52.86 %	3.49 %
Second Session			
Reflection	69.70 %	19.39 %	10.91 %
Focus	22.27 %	69.09 %	8.64 %
Visible Iris	24.09 %	38.64 %	37.27 %

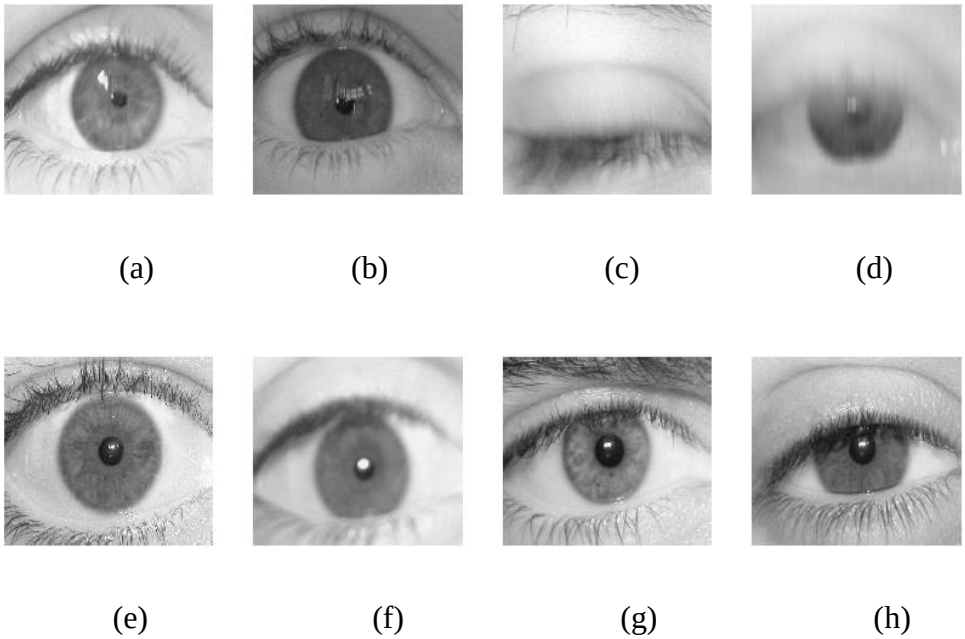

(a) (b) (c) (d)

(e) (f) (g) (h)

Figure 22 Samples from UBIRIS V1 iris database [47]

3.2.8 UBIRIS V2 Database

In 2010, the University of Beira introduced another version of UBIRIS database called UBIRIS.v2 [48] iris database, which is a multisession iris database that contains images captured at a distance of 4 to 8 metres, on the move and lit with a visible wavelength light source. The reason behind the creation of UBIRIS.v2 database is to constitute a new iris dataset collected under a natural or artificial visible wavelength light source, with characteristics far away from ideal imaging framework.

The Canon EOS 5D was used, with 1/197 shutter speed, 400mm focal length, 1/200s exposure time and ISO-1600 speed. The resultant image is 800×600, with 72 dpi vertical/horizontal resolution and 24 bit colour depth, stored in tiff file format.

Unlike UBIRIS.v1, images in UBIRIS.v2 were captured over a distance of 4 to 8 metres. The subjects were asked to walk in average speed slower than normal towards the acquisition camera. Three images per metre were captured while the human subject was looking at preplaced lateral signs. That obliged them to rotate their heads.

There were 261 volunteers participating with 522 (261× 2 left and right) irises, producing 11,102 images. Like UBIRIS.v1, the images have been captured in two different sessions, with a two week interval. 60 percent of the volunteers participated in both sessions and 40 percent participated either in the first or second sessions.

Images in UBIRIS.v2 database have homogeneous characteristics, with 14 different types of noise, "((1) Off-angle iris image, (2) Poorly focused iris image, (3) Rotated iris image, (4) Motion-blurred iris image, (5) Iris obstructions due to eyelids, (6) Iris obstructions due

to eyelashes, (7) Iris obstructions due to glasses, (8) Iris obstructions due to contact lenses, (9) Iris obstructions due to hair, (10) Iris imaging in poor lighting conditions, (11) Iris with specular reflections, (11) Iris with lighting reflections, (12) Partially captured iris, (13) Dark iris, and (14) Out-of-iris image)" [48], see Figure 23. This heterogeneity makes this database an appropriate set for evaluation of unconstrained iris recognition algorithms.

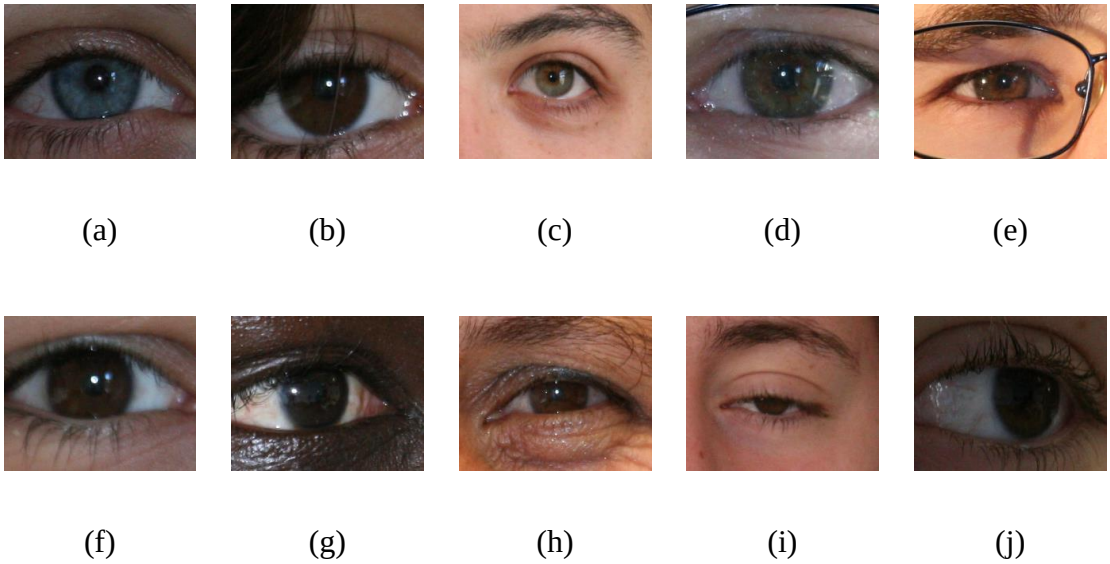

Figure 23 Samples from UBIRIS V2 iris database [48]

3.3 Importance of being random

The key behind any recognition system is the failure of a test of statistical independence [11], which involves so many degrees-of-freedom (249) as a complex textures [7, 49]. Many parameters in the iris recognition system should be considered, and the optimal threshold values to these parameters should be assigned to ensure the maximum recognition accuracy. These parameters include the dimension of input image, the radial and angular resolution of the normalized rectangular image r and θ respectively. That will

be used for the calculation of the number of coefficients extracted, the number of filters N for feature encoding, the wavelength of the selected filter λ, the filter bandwidth ($\frac{\sigma}{f}$), and many other parameters which will be described in next chapters.

The test of statistical independence is implemented as described in Daugman's proposal [11], used a simple XOR operator over 2,048 bit iris template to calculate the hamming distance under different dissimilarity threshold values to calculate the recognition system accuracy [11] as seen in Figure 24.

$$\text{Hamming Distance} = \frac{\|(Code\ A\ \otimes Code\ B) \cap Mask\ A\ \cap Mask\ B\ \|}{\|Mask\ A\ \cap Mask\ B\|}$$

where $Code\ A\ and\ Code\ B$ are the extracted features and the stored features respectively, $Mask\ A\ and\ Mask\ B$ are the noise masks from the input template and the stored template.

HD criterion	Odds of false match
0.26	1 in 10^{13}
0.27	1 in 10^{12}
0.28	1 in 10^{11}
0.29	1 in 13 billion
0.30	1 in 1.5 billion
0.31	1 in 185 million
0.32	1 in 26 million
0.33	1 in 4 million
0.34	1 in 690,000
0.35	1 in 133,000
0.36	1 in 28,000
0.37	1 in 6,750
0.38	1 in 1,780
0.39	1 in 520
0.40	1 in 170

Figure 24 Hamming Distance and Equivalent False Match [11]

(Table 2 and Table 3) summarize the free available iris databases and their characteristics.

3.4 Comparison of Iris Databases

Table 2 Comparision of Free iris database

Database name	Database size	Light wave length	Varying distance	Camera	Sample image
CASIA v1	756	NIR	No	CASIA camera	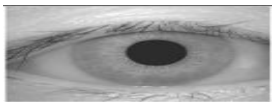
CASIA v2	2,255	NIR	No	CASIA camera	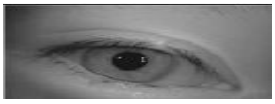
CASIA v3	22,051	NIR	No	OKI iris-pass h	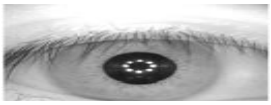
Bath	16,000	NIR	No	ISG LW 1.3 S 1394	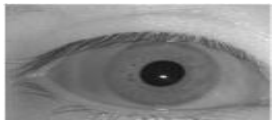
MMU 1	450	NIR	No	LG EOU 2200	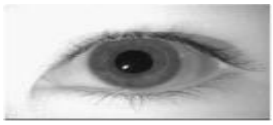
MMU 2	995	NIR	No	Panasonic BM ET 100 US	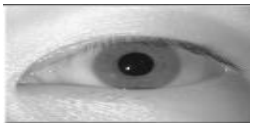
ICE 1	2,900	NIR	No	LG EOU 2200	

ICE 2	75,000	NIR	No	LG EOU 2200	
WVU	3099	NIR	No	OKI iris-pass h	
UPOL	384	Visible	No	Sony DXC 950P 3CCD with TOPCON TRC501A	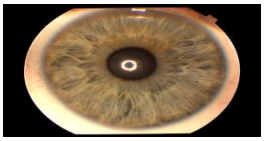
UBIRIS v1	1877	Visible	No	NIKON E5700	
UBIRIS v2	11,357	Visible	Yes	Canon EOS 5D	

Table 3 Heterogeneity of iris databases

Database	Noise													
	Eyelashes	Eyelids	Specular Reflection	Light Reflection	Motion Blurred	Poor Focus	Gaze Deviated	Partially Occluded	Out of Iris	Over Distance	On The Move	Rotated	Glasses	Visible Wavelength
CASIA 1	√	√	-	-	-	-	-	-	-	-	-	-	-	-
CASIA 2	√	√	-	-	-	-	-	-	-	-	-	-	-	-
CASIA 3	√	√	-	-	-	-	-	-	-	-	-	-	-	-
BATH	√	√	-	-	-	-	√	-	-	-	-	√	-	-
MMU 1	√	√	-	-	-	-	-	-	-	-	-	-	-	-
MMU 2	√	√	-	-	-	-	-	-	-	-	-	-	-	-
ICE 1	√	√	-	-	-	-	√	-	-	-	-	√	-	-
ICE 2	√	√	-	-	-	-	√	√	√	-	-	√	-	-
WVU	√	√	-	-	√	√	√	√	-	-	√	√	-	-
UPOL	-	-	-	-	-	-	-	-	-	-	-	-	-	√
UBIRIS.v1	√	√	√	√	√	√	√	√	√	-	-	√	√	√
UBIRIS.v2	√	√	√	√	√	√	√	√	√	√	√	√	√	√

3.5 Conclusion

This chapter summarize all free available iris databases, these databases are categorized in two types, the first category contains the noise free iris databases that have been captured under NIR light source (CASIA, BATH, MMU, ICE and WVU). While the noisy iris databases that have been captured under visible wavelength light source (UPOL, UBIRISv.1 and UBIRISv.2) fall in the second category.

The proposed framework was tested on three visible wavelength databases; the first one was UPOL database that contains high resolution images; The second was the UBIRISv.1 database which contains noisy images captured under different light sources with high reflection and different occlusion ratio but at close distance without subject moving; the third database that best meets the requirements of the proposed algorithms is UBIRS-v2.

Chapter 4. Iris Segmentation

4.1 Introduction

The majority of iris recognition systems follow the standard pattern recognition paradigm which consists of four phases: The segmentation phase, the normalization phase, the feature extraction phase and finally the template matching phase. In the segmentation process, the iris region must be isolated from the whole eye image, and this process approximates two circles to separate the three major parts of human eye (sclera, iris and pupil), and approximates two curves to isolate upper and lower eyelids (Figure 25).

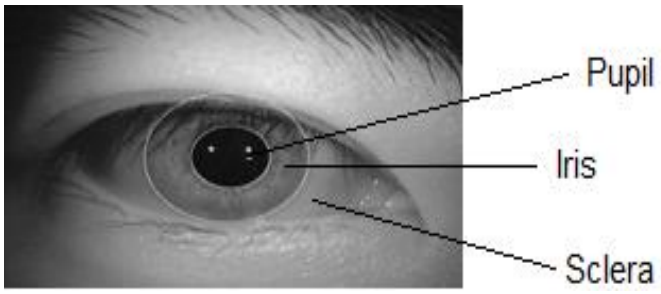

Figure 25 Segmented iris images

The accuracy of the segmentation process depends on the quality of the captured images. Most of the currently available iris recognition systems rely on high quality images captured with NIR light sources (no reflection) at close distances and with look and stare constraints, like those images presented in the CASIA database [40]. This type of images can be correctly segmented using circular shape detection algorithms that will be described in next section.

Most of the current iris recognition systems use an NIR illumination light source to reveal the pigmentation of the iris image, but other researchers [55] have investigated the effects of visible wavelength vs. NIR light source on the iris image. The main differences between NIR illumination and a visible wavelength light source is that a clear pigmentation is revealed from NIR illuminated image (rich iris texture). Furthermore, NIR lights do not cause reflection noise on the image, while a visible wavelength lighting source causes reflection noise on the captured images (Figure 26 and Figure 27).

Grabowski et al in [20] also mentioned the main difference in localizing iris images captured under different light sources.

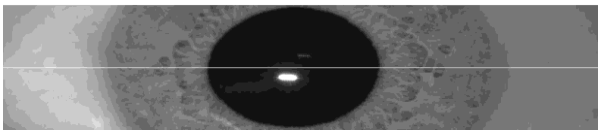

Figure 26 NIR Image

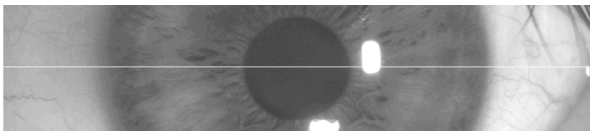

Figure 27 Visible Wavelength Image

In all iris recognition systems, before localizing the iris area, the centre of the pupil should be determined as a reference point from which to start searching the iris area. The localization algorithm for an NIR iris image as in Figure 26 is searching for the iris area from the inside ring to the outside because the transition intensity from pupil to iris is clearly significant. In contrast, in visible wavelength iris images, as Figure 27 shows, the

search algorithm is searching from outer ring to inner because the transition is more significant than the iris pupil.

In [55] Grabowski et al used a strong white visible wavelength light to illuminate the iris image with a mean colour temperature equal to 5780K, to reveal a clear structure of the iris image. He also achieved a clear iris image in visible wavelength that can be compared with NIR images as shown in Figure 28.

(a) (b)

Figure 28 (a) Visible wavelength, (b) NIR [55]

Although he used a very strong visible light source, the results of his experiments show that iris recognition under NIR light source gives better results than under visible wavelength iris images, especially in FRR and FAR. This is because in the visible wavelength light source, the revealed iris texture will be affected with light and specular reflection. Moreover, small elements, like caverns, muscle fibre etc., will appear in the captured images, which will affect the segmentation process.

Furthermore, the reason for low accuracy in [55] is that the author used Daugman's method based on integro-differential operator for segmentations and Gabor wavelet

transform to extract the features from iris images captured at visible wavelength. This algorithm was designed and programmed to extract the features from free of noise NIR iris images. Therefore, to get better results, different feature extraction algorithm must be used.

Recent works in iris recognition are trying to increase the segmentation accuracy while processing images with heterogeneous characteristics, such as the images presented in the UBIRISv.1 [47] and UBIRISv.2 [48] databases. The importance of the segmentations comes from the dependency of all pattern recognition systems, inaccurate segmentation causes failure in the whole recognition process.

4.2 Segmentation Algorithms

In this section, the most frequently used and cited segmentation algorithm will be described. Through a wide research, we found that iris image can be segmented using one of three major strategies: the first one is based on iris outer and inner boundaries [6]. The second strategy is based on the iris template [11], and [56] and [50],The third one is a hybrid [57] approach, which is based on iris colour template and iris boundaries.

In the next section, the main segmentation methods cited in the literature are discussed.

4.2.1 Daugman's Method

This proposal was the first successfully implemented method in the field of iris recognition, it was proposed by Daugman in 1993 [11], and adopted by Iridian Technologies. Daugman applied the integro differential operator to find centre point (x, y) and radius (r) for both iris borders, first the outer border (iris-sclera), and then the

inner border (pupil-iris). In his proposal Daugman assumes both the iris and pupil are in circular shape, and applied the integro differential operator as follows:

$$max_{r,x_0,y_0}\left|G_\sigma(r) * \frac{\delta}{\delta r}\oint_{r,x_0,y_0}\frac{I(x,y)}{2\pi r}\,d_s\right|$$

where $I(x,y)$ is the intensity value for pixel at (x,y) position in the grey level image, r is a varying radius, G is the Gaussian smoothing function and d_s is the circular path. This operator searches for the circumference (circular path) with the maximum variation in pixel intensity value over N^3 space domain. Initially the pixels with the local minima intensity are located to act as a possible centre point for the expected circumference, as seen in Figure 29. The iris area and precisely the pupil area will always have the minimum intensity value as they are the darkest pixels in the human eye image.

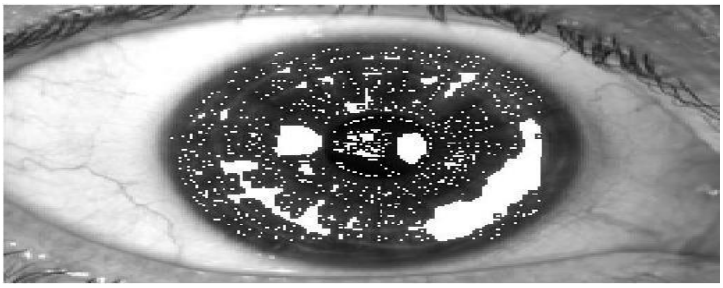

Figure 29 pixels with minimum intensity values [7].

Before implementing the integro differential operator, a pre-process should be made to the grey level image, as this operator fails when there is no significant intensity separability between the coloured region iris ring and the white region sclera. To solve this problem a histogram equalization method should be applied along with contrast enhancement, to enhance the separation between the three eye parts (sclera, iris and pupil) as shown in Figure 30.

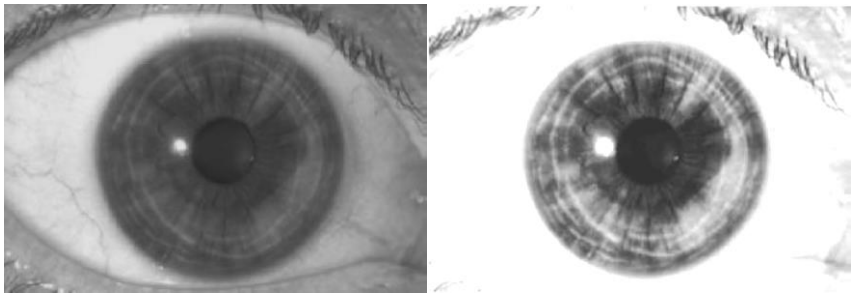

Figure 30 Before and After Contrast Enhancement

However, through tests it was observed that, Daugman's integro differential operator can segment iris images with good quality, like those images introduced in CASIA [40], Bath [41] and UPOL [46] databases, while fails when segmenting noisy images like those presented in UBIRIS.v1 [47] and UBIRIS.v2 [48] databases.

4.2.2 Camus and Wildes Method

Camus and Wildes [56] proposed a method for localizing inner and outer boundaries of the iris on the basis of the maximum summation of directional derivative for image intensity in radial direction. This method works just like Daugman's method, which finds the centre point and the radius of iris pupil circular shape by implementing the following equation:

$$max_{r,x_0,y_0} = \sum_{\theta=1}^{n} \left((n-1) \parallel g_{\theta,r} \parallel - \sum_{\emptyset=\theta+1}^{n} \left(\parallel g_{\theta,r} - g_{\emptyset,r} \parallel \right) - \frac{g_{\theta,r}}{n} \right)$$

where n is the number of discrete values for the polar variable θ and $g_{\theta,r}$ is the directional derivative in radial direction, and $g_{\emptyset,r}$ is the ellipse parameter for the pupil area. This method segments the human iris through three stages, the first one is the specularity filling. This stage minimises the influence of specular reflections by locating the high

intensity pixels with values over 250 out of 0-255 range. The second stage, called seed point selection, finds the centre point and the radius of the pupil area on the basis of locating the local minima intensity pixels then applying the above formula as well as the iris area. The last stage is the boundary representation by means of centre and radius.

Camus and Wildes' method has more accurate and results than Daugman's and can process images with specular reflection. However, the results are still unacceptable under other noise factors.

4.2.3 Roche and Avilla's Method

The method proposed in [50] follows the template based strategies just like Daugman's method. The algorithm receives a grey scale input image. Then the histogram stretch process is applied to emphasize the intensity separation. After histogram stretching, the authors implemented the image gridding method to search for the pixels with lowest intensity to act as a centre point for the future search. Finally, the maximum difference between five circumferences with consecutive radius is calculated. The method is applied twice over the image domain to form the outer and inner iris ring as follows:

$$D = \sum_{m} \left(\sum_{k=1}^{5} \left(I_{n,m} - I_{n-k,m} \right) \right)$$

where

$$I_{i,j} = I(x_0 + i\Delta_r \cos(j\Delta_\theta), y_0 + i\Delta_r \sin(j\Delta_\theta))$$

where $I_{n,m}$ is the image, k is the circumference parameter, (x_0, y_0) is the centre point from the gridding method, Δ_θ and Δ_r are the increments of angle and radius, and $I_{i,j}$ is the grey scale image.

All the previously described methods search in N^3 space, for the three circular parameters, point x, point y and the radius r, which makes the time required for iris segmentation relatively proportionate to image size. The larger the image size, the slower the image segmentation.

4.2.4 Wildes Method

This method is an example of boundary based strategy, proposed in 1997 by Wildes [6]. This proposal performs iris segmentations using circular contours fitting in two steps. The first step is to extract the edge map on the basis of image intensity information using Canny edge detector. In the second step, the circular Hough transform is applied to the binary edge map, where each edge point vote to instantiate radius and centre coordinate values for a particular contour, which satisfies the following equation.

$$x = a + R\ \cos\theta$$
$$y = b + R\ \sin\theta$$

where R is the radius, θ varies 0-360 to form a circle, (a, b) is the centre coordinates.

In the process of edge map detection, the map is built using the gradient-based Canny edge detector to incorporate directional selection. The grey scale image intensity is weighted to produce different ranges of orientation. In other words, the edge points are extracted in both directions (horizontally and vertically) as seen in Figure 31.

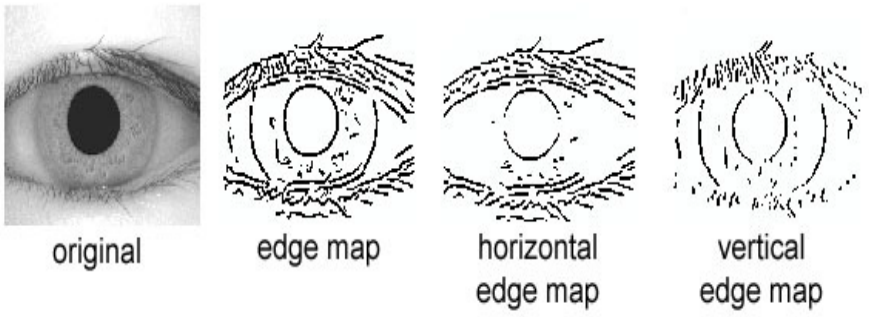

Figure 31 Edge map [6].

The edge points in the vertical edge map are appropriate for the detection sclera iris and pupil circles, while the horizontal points offer more formation for the detection of upper and lower eyelids arcs.

For iris-sclera and iris-pupil detection, each point from the vertical edge map casts a vote in the Hough space for circular parameters (centre, radius), where the edge point acts as centre point for a circle with increasing radius. The point with maximum circumferences intersection will represent the circle centre as shown in Figure 32, and the distance between the detected centre and the extracted edge points that forms the circumferences will represents the radius. For the detection of the upper and lower eyelids, the parabolic Hough transform is applied to the horizontal edge map with arcs parameter instead of circular parameters as follows:

$$(-(x-h_j)\sin\theta_j + (y-k_j)\cos\theta_j)^2 = a_j((x-h_j)\cos\theta_j + (y-k_j)\sin\theta_j)$$

where (h_j, k_j) is the peak of parabola, a_j control the curvature and θ_j is the rotation angle.

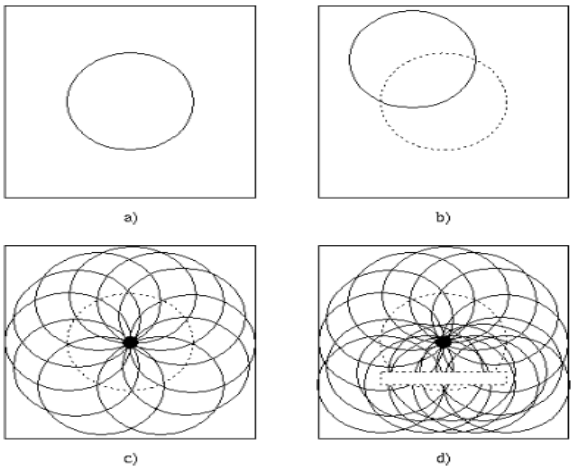

Figure 32 a) input image, b) edge map, with one edge act as a centre to draw a circle with r radius, c) dark point represents the maximum intersection, d) the correct centre with the presence of noise.

4.2.5 Proença Method UBIRIS.v1

In [58] Proença and Alexandre propose a segmentation method based on moments function [59] and clustering followed by canny edge detection and circular Hough transform (Figure 33). Their method was the first successful method that can segment noisy iris images, like those images presented in UBIRIS database.

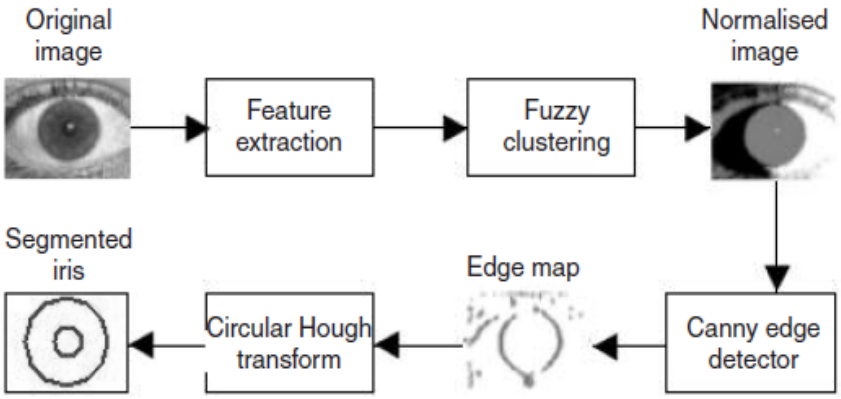

Figure 33 Proença and Alexandre segmentation method for UBIRIS V1 [58]

The first step in Proença and Alexandre's method is the feature extraction step, where the authors used a moment texture segmentation algorithm proposed by Tuceryan [59], which computes the moments over the image intensity domain in small windows as a texture features. The computed moment presents three discrete features for each pixel from the input image, (x, y) to represent the pixel position and $I(x, y)$ for pixel intensity. The moment calculated over image intensity domain is defined as:

$$M_{pq} = \left(\sum_{-\frac{w}{2}}^{\frac{w}{2}} \left(\sum_{-\frac{w}{2}}^{\frac{w}{2}} \left(I(m,n) x_m^p y_n^q \right) \right) \right)$$

where M_{pq}, is the geometric moments of p and q order pixels, $I(m, n)$ is the pixel intensity, w and (x, y) are the moment windows width and coordinate. To emphasize the discriminating capacity between these regular order geometric moments, the author computes the average of the hyperbolic tangent for all moment functions as follows:

$$F_{pq}(i,j) = \frac{1}{L^2} \sum_{(a,b)\epsilon w_{ij}} \left(\tanh\left(\sigma\left(M_{pq}(a,b) - \bar{M} \right) \right) \right)$$

where F_{pq}, is the feature image for all moments with $\bar{M}$ mean, the variable w_{ij} the average window at (i, j) centre location and σ is the controller parameter for the logistic function shape.

After the feature extraction step, and to produce an intermediate image that has a number of intensities smaller than what the original image dose. Proença utilizes the application of Fuzzy K-Means as clustering algorithm for discrimination between the pixels that

belong to iris region and the pixels that belong to the remaining eye regions. The Fuzzy K-Means can be described as follows:

$$J_{fuz} = \sum_{i=1}^{c}\left(\sum_{j=1}^{n}\left(\hat{P}(w_i|x_j,\hat{\theta})^{p}\|x_j - \mu_i\|^{2}\right)\right)$$

where μ_i, is the cluster value, and P is the parameter used to adjust the blending of different clusters. The result from the first two steps will be an intermediate image with minimal range of intensity as shown in Figure 34.

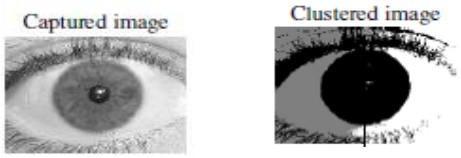

(a) (b)

Figure 34 Minimal intensity range [58].

After the clustering step, the intermediate image will be used by Canny edge detector to produce edge map image that is less sensitive to the noise introduced by light reflection and obstruction of eyelids and eyelashes. Finally the circular Hough transform is applied to the edge map to approximate the inner and outer iris rings.

4.2.6 Proença Method UBIRIS.v2

In 2010, another version of UBIRIS database, which contains more noisy images than the first version of the database, was introduced [57]. So, Proença proposed a new segmentation method that can segment noisier images like those images presented in UBIRIS.v2 databases.

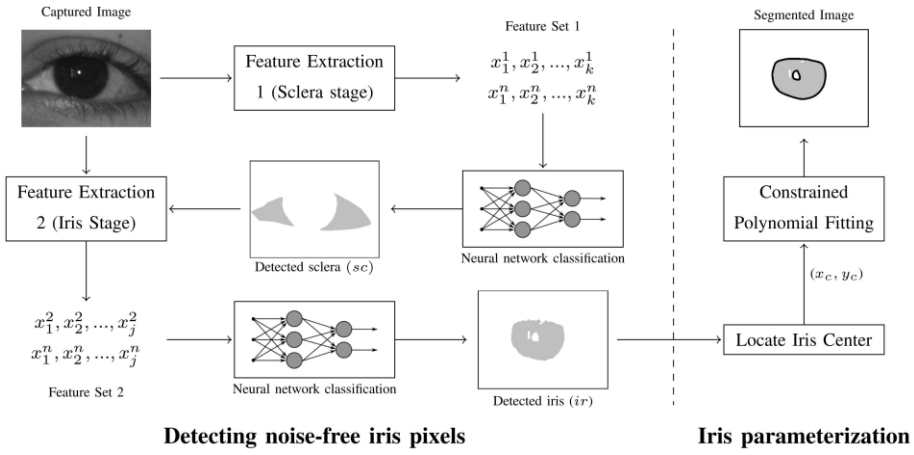

Figure 35 Proença's segmentation method for UBIRIS V2 [57].

Proença's new method is divided into two stages: The first stage is responsible for detecting the noise-free iris pixels, and the second stage parameterizes the iris shape as shown in Figure 35. This method depends on extracting local features through single image scan for the detection of sclera and iris regions by calculating the local central moments (Average intensity and Standard deviation) within increasing the dimension over the image domain of different colour spaces.

The first stage in Proença's method is subdivided into two steps:

- **Sclera detection**

  The sclera part of the image is the most easily distinguishable part in the noisy eyes images, due to the maximum contrast separation between sclera region and the other eye parts. In order to enhance the contrast between the sclera and the remaining eye parts, the author uses the hue (h), chromatic blue (cb) and chromatic red (cr) colour spaces as shown in Figure 36. To detect the sclera region

a 20-dimintional feature set were extracted from each pixel to classify weather the pixel belong to sclera region or to other eye parts.

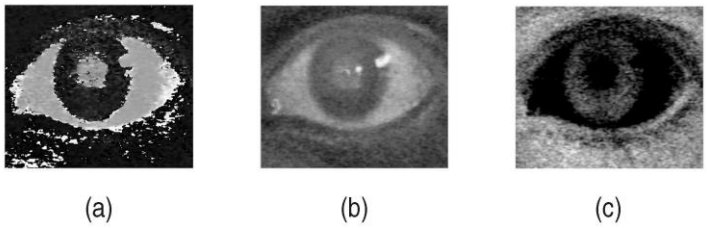

Figure 36 a) hue, b) chromatic blue, c) chromatic red [57]

$$Feature\ set\ for\ each\ pixel\left(\ \{x, y, h_{0,3,7}^{\mu,\sigma}(x,y), cb_{0,3,7}^{\mu,\sigma}(x,y), cr_{0,3,7}^{\mu,\sigma}(x,y)\}\ \right)$$

where x and y denote pixel position, h, cb, cr denote the colour space region centred at the given pixel, and the subscripts 0,3,7 denote the increasing radii.

- **Iris detection**

  For the detection of the iris region, the author utilizes the data from the sclera stage to form a new feature set for detecting the iris region called proportion of the sclera for each pixel in the image. This process measures the proportion of sclera pixels in all directions (north, south, east and west) (Figure 37) with respect to the reference pixel (x, y).

$$p_{\leftarrow}(x,y) = \mu\left(sc\big((1, y-1), (x,y)\big)\right)$$

$$p_{\rightarrow}(x,y) = \mu\left(sc\big((x, y-1), (w,y)\big)\right)$$

$$p_{\uparrow}(x,y) = \mu\left(sc\big((x, 1-1), (x,y)\big)\right)$$

$$p_{\leftarrow}(x,y) = \mu\left(sc\big((x-1, y), (x,h)\big)\right)$$

where $sc(,)(,)$ denotes the sclera region from sclera detection stage (Figure 35), w, h are image width and height, all sclera pixels extracted from the previous step were set to 0.

Finally, to classify weather the pixel belongs to iris region or not, an 18 dimensional feature set is created, and it contains pixel position, saturation, chromatic blue and proportion of sclera for each image pixel apart from sclera region:

$$Feature\ set\ for\ each\ pixel\ \left(\left\{x, y, s_{0,3,7}^{\mu,\sigma}(x,y), cb_{0,3,7}^{\mu,\sigma}(x,y), p_{\leftarrow,\rightarrow,\uparrow,\downarrow}(x,y)\right\}\right)$$

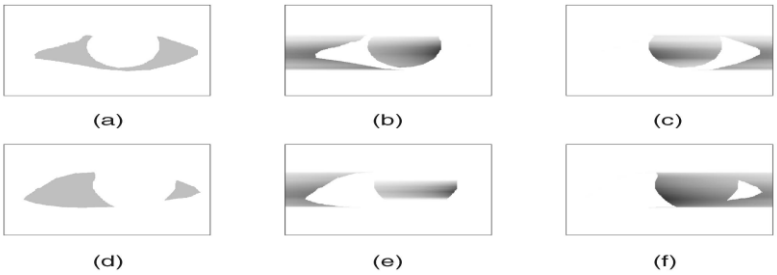

Figure 37 The proportion of sclera in all direction (a),(b)and (c) for a straight eye image, (d),(e) and (f) for gaze divated eye [57].

For the coarse classification of the features, the author uses supervised machine learning that performs binary classification at pixel level. Due to the heterogeneous characteristics and the large amount of data presented in the iris images, the author use a multi-layered feed-forward neural network with a single hidden layer for both classification stages (sclera and iris).

In the last stage, and for fine shape parameterization, the author uses a polynomial fitting technique for the approximation of papillary and scleric iris border. The fitting process starts by localizing the iris centre according to the highest value in all direction from the roughly detected centre, which will act as a reference point while converting the image from Cartesian coordinate to polar coordinate for polynomial fitting and remapping process as shown in Figure 38.

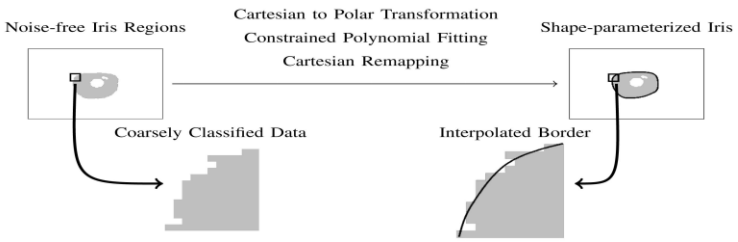

Figure 38 Coarse to fine segmentation [57]

4.2.7 Iris Segmentation Techniques

Recently, many methods were developed to increase the robustness of the segmentation process in non-ideal conditions. In [60], Chen, Lin, and Ding introduces a textural segmentation algorithm based on adaptive mean shift procedure for initial coarse segmentation. Then the method search over a grey scale image for the pupil area to roughly estimate the iris centre. In the second phase they extracts the gradient features by using 2D Gabor filter, and finally he applies an active contour to search for a real inner and outer iris fine boundaries.

Another approach for noisy iris segmentation was introduced in [61]. The proposed method first searches for sclera region in Hue, chromatic blue and chromatic red spaces, to roughly detect the pixels with high intensity values representing the sclera area to locate

the eye region from the input images. After the detection of the eye, a feature extraction process is applied to each pixel in the input image based on Zernike moments. The extracted features are then passed to learning algorithm which uses NN (Neural Network) and SVM (Support Vector Machine) to classify the pixels into iris or non-iris category.

Radman, Zainal and Jumari [62] apply a circular Gabor filter followed by a modified version of Daugman's integro-differential operator [11], to detect the pupil area as it is the most dark area in the human, then then to detect the iris inner and outer boundaries using integro-differential operator, and, finally, to detect the upper and lower eyelids by the live-wire method.

All the methods described in this chapter achieved a good segmentation accuracy when applied to noise free iris images like CASIA iris database. Nevertheless, these methods performance needs improvements when applied to iris images with heterogeneous characteristics like UBIRISv.1 and UBIRISv.2 databases (see Tables 4, 5 and 6).

4.3 Proposed Method

The key behind successful unconstrained iris recognition is the ability of the system to detect the noise factors that affect the iris images. Once the noise factors affecting the input images are known, then it could be easy to apply a suitable filter to process the input image for successful segmentation.

Experiments were held on UBIRISv.1 and UBIRISv.2 databases, and as described in Chapter 3, those images have a heterogeneous characteristic with many noise factors that affect the iris images.

The algorithm is based on RGB colour space. The empirical analysis of different colour spaces led to the selection of the Red value average. In order to determine what noise factor affects the input image, through experiments over 15,000 images, it was observed that the stability of Green and Blue values in comparison to the red value under different imaging conditions. That means that if the lighting condition is changed at the time of capturing same image, the average of Green and Blue values (intensity) will vary in amount of $\approx$ 5 -15 %, while the average Red colour value will vary in amount of 10 - 35 %. This is because one can find a human with blue or green irises, but there are no humans with a red iris. For example, a blue coloured RGB iris image will have high blue (B) value regardless of the noise factor affecting that image, while the major variations will be found in the value of red (R) and green (G). Nevertheless, for green coloured RGB iris image, the value of green (G) will be relatively high and stable under different imaging conditions in comparison with the value of (R) and (B) component. Finally, for those irises with brown, hazel and grey colour, different imaging environments will affect all colours, but still the major variations will be in the red colour component.

For image classification according to red colour average, seven different categories have been chosen. The first three categories include (black skin humans with very dark iris colour, the poor illuminated iris images and the poor focused images). These images suffer from low brightness and contrast. So, a contrast enhancement algorithm is applied. In the fourth category, no pre-processing is needed because only the clear images fall into this category, and the last three categories contain images with (specular reflection, light

reflection and images with glasses). Here a smoothing technique is applied to process the input image.

As a conclusion, the whole segmentation process is subdivided into three steps; the first one is detection of sclera as it is the most easily distinguishable part of the human eye. To get rid of other eye parts, like eyebrows and the skin of the upper and lower eyelids, the output parameters will be the points(x_1, y_1), (x_2, y_2) and (x_3, y_3), (x_4, y_4) that represent the far left and the far right corners of the human eye, as well as upper and lower extremes of the eye region. From these point coordinates, we can reduce the influence of the iris rotation by altering the values of y_1 and y_2 points until $y_1 = y_2$, see Figure 40.

The second part of the method is further subdivided into two steps. The first step is the quality assessment that classifies the input image according to image quality, and it applies a suitable filter, while the second step converts the RGB image to a binary image for outer ring segmentation.

In the last part of the method, the segmented image that results from the second part is converted to HSV to detect and segment the pupil area. The next three sections will explain each part of the method, and the last section will be dedicated to the experimental results.

4.3.1 Proposed Sclera Detection Phase

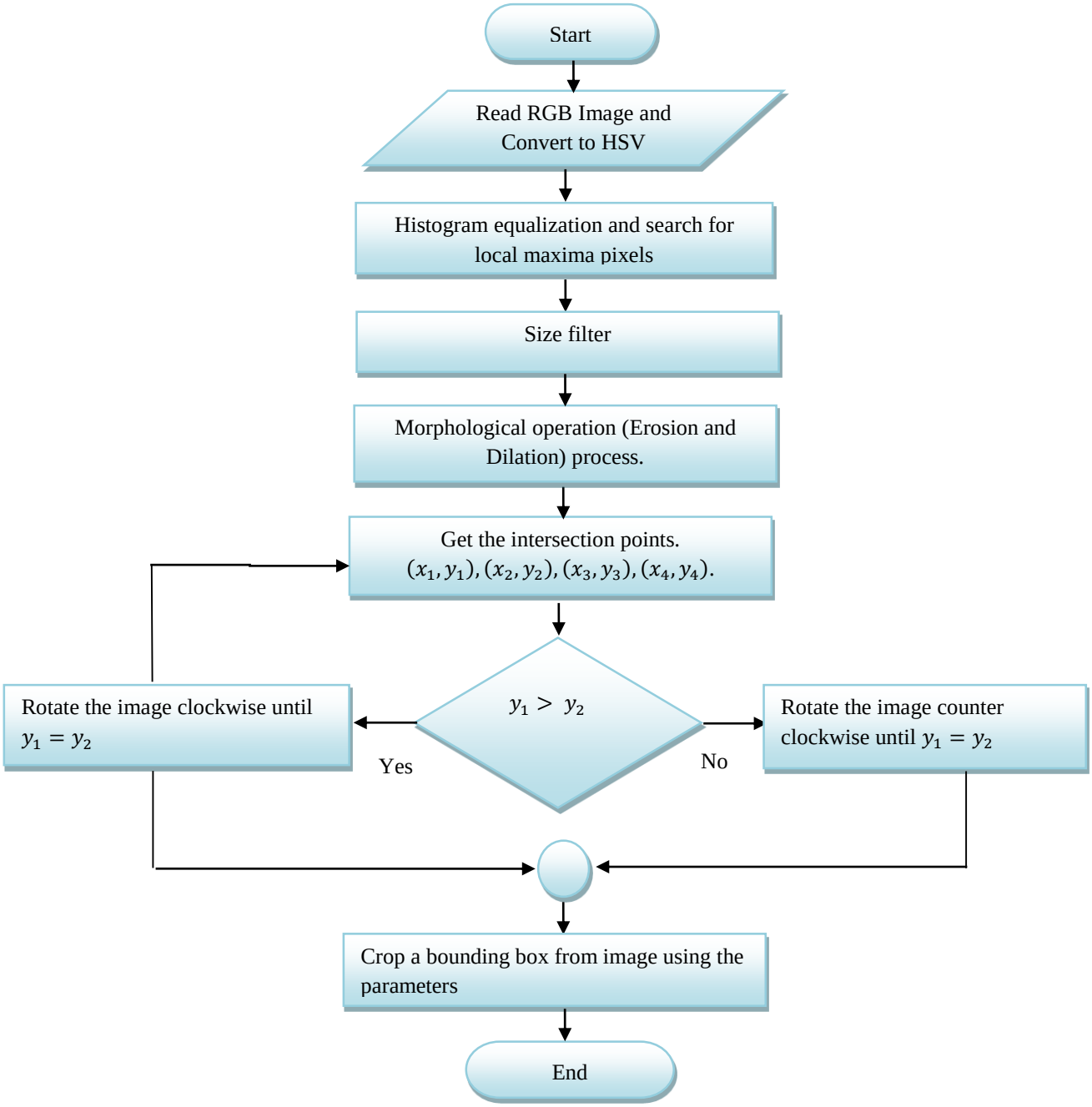

Figure 39 Flow Chart for Sclera Detection

4.3.2 Flow chart in Figure 39.

The flow chart in Figure 39 shows the process for sclera detection and the rotation angle correction as following.

1. Read the selected RGB, for image size refer to (Chapter 3).
2. Search for local maxima pixels

$$HSVmask_{(x,y)} = \begin{cases} 1 \; if\,(\, H > h_{th} \; And \; S < S_{th} \; And \; V > V_{th}) \\ 0 \qquad\qquad\qquad\qquad\qquad\qquad otherwise \end{cases}$$

   where, $HSVmask_{(x,y)}$ is the masked pixels of the image that contains the pixels with Hue H, Saturation S and Value V that defines the area of high intensity colour representing the white pixels from the input RGB images, if the condition of the above equation is true, then assign 1's to pixel value and 0's otherwise. Empirical analysis of high intensity pixels detection led to using (0.73, 0.17 and 0.53) for Hue h_{th}, Saturation s_{th} and Value v_{th} thresholds respectively, were the best threshold values when applied over different image qualities.
3. The output image from step 2 will be a non-smooth binary image and full with gaps in both colours, the white and black regions, due to the noise factors introduced in the original image. To overcome the incorrectly detected pixels and eliminate gaps from the resultant image, a size filter followed by erosion and dilation and operators are applied to smooth the outer edges and fill the undetected small gaps.
4. Now we just have the sclera area of the whole eye image. The main reason for this process is to minimize the searching area for iris segmentation, and to normalize

the iris area to a fixed size and finally to find the angle of rotation. A search process to find the first five black pixels with interval of 10 pixels has been made from both left and right side of the sclera, and for the upper and the lower side separately as seen in Figure 40.

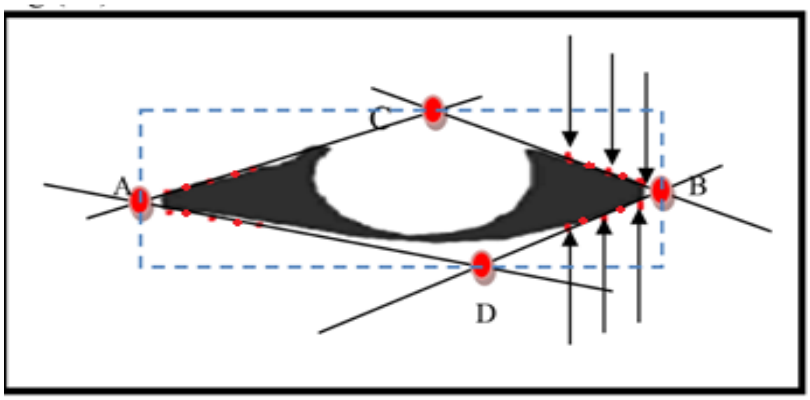

Figure 40 Sclera detection

Using linear polynomial fitting, a tangent line that crosses the upper and lower detected pixels from both sides is drawn, the rectangular area that crosses intersection points for all tangents will represents the area of interest, where A,B,C and D represent the points $(x_1, y_1), (x_2, y_2), (x_3, y_3), (x_4, y_4)$ respectively.

The output of this process is dependent on the image quality, if the input image was clear the output from sclera detection process will be robust like the image shown in Figure 40 and no further process is needed for the outer ring segmentation, but in most cases the input image will have a heterogeneous characteristics like those images presented in UBIRISv.1 and UBIRISv.2. Thus the output from the sclera detection process will have either missing parts

especially in dark areas around the iris and eyelids caused by poor lighting and the occlusion of eyelashes, or some additional parts from iris bright areas caused by light reflection (Figure 41). Therefore, a refining process is applied which will be presented in Section 4.4.3.

Figure 41 Sclera detection from noisy iris image

5. Rotate the image until $y_1 = y_2$.
6. Crop a bounding box with width = $x_1 - x_2$, and height = $y_1 - y_2$.

This phase detects the exact eye area, apart from other face parts and correct the rotation of the iris caused by unconstrained environment.

4.3.3 Outer Ring Segmentation Phase (Iris-Sclera)

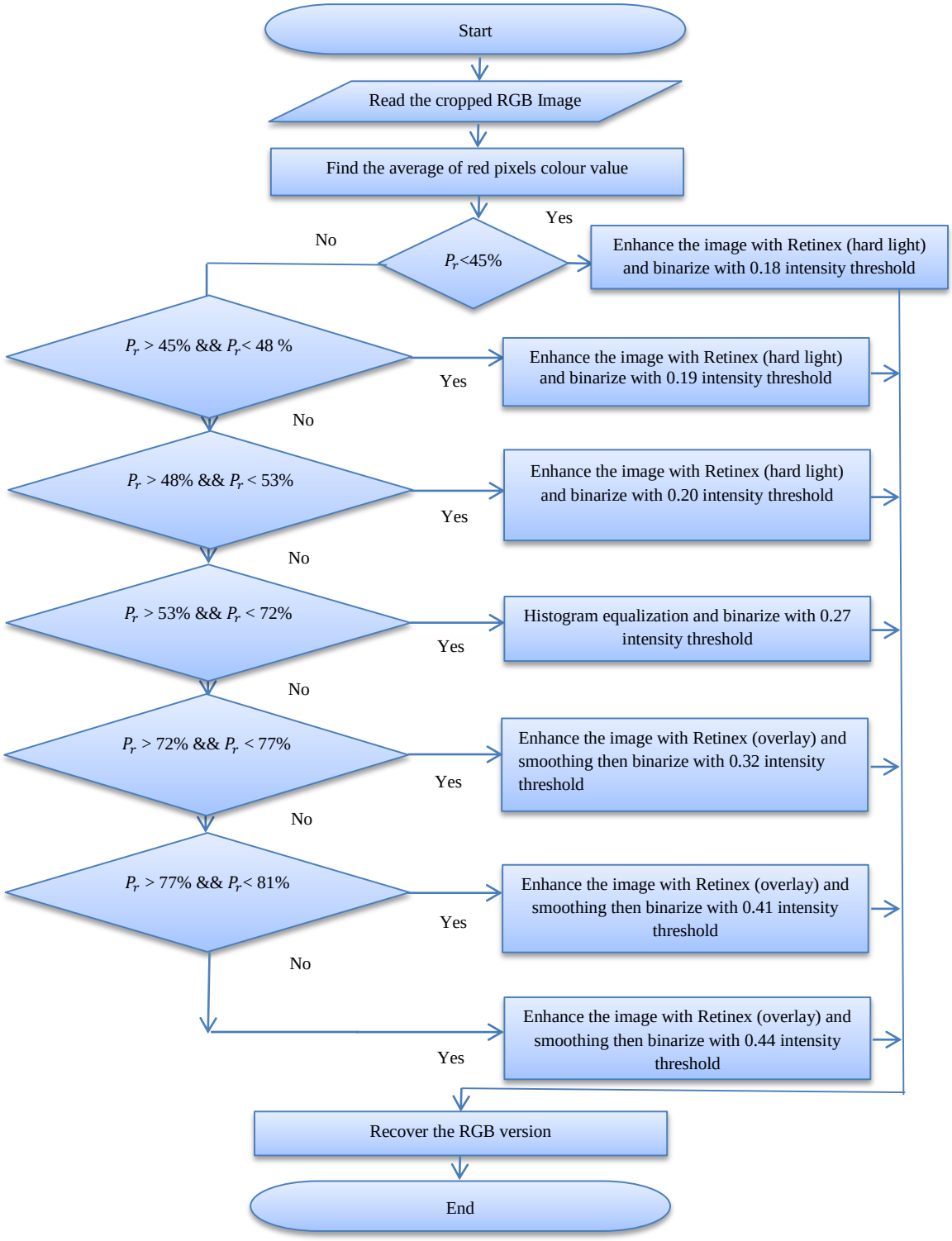

Figure 42 Flow Chart for Outer Ring Segmentation

4.3.4 Flow chart of Figure 42

The flow chart in Figure 42 shows the process of iris inner and outer ring segmentation as follows.

1. Read RGB image resulting from Sclera Detection Phase.
2. Classify the input images whether they are poor, faded, blurred, low reflection or

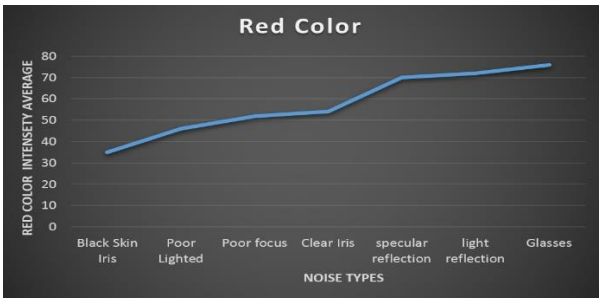

Figure 43 Red colour intensity for different irises categories

To optimize the red colour average for each category, a database of 500 images was manually selected from each database (UBIRISv.1 and UBIRISv.2) for learning. Then each image was manually classified into one of the above stated categories. After the classifications, the red colour map images were extracted then the sum of the red colour values were calculated from each map in a specific category and stored for further analysis, as seen in Figure 43. After plotting the calculated intensities, it became obvious that the images in each category have very close red intensity values, whereas they have high variation in different categories. After the learning process using 500 images from each database, the extracted red intensity features were applied to the whole UBIRISv.1 and UBIRISv.2 databases for image classifications, and the algorithm was successful

to correctly classify the majority of images according to noise factor, but with a major failure where the image is affected with more than one noise factor.

3. Based on Red colour value, apply the suitable filter and threshold value to create a binary image of the input image.

   For low Red intensity, as in the case of people with dark skin, poor lighting and poor focus, enhance the image using Retinex method as implemented in [39] via hard light with saturation adjust and without smoothing operation, and for high red intensity, as in the cases of high reflection images, images with glasses and specular reflection images, smooth the image with sharp Gaussian kernel and then apply the Retinex method via overlay with saturation adjustment.

   The Retinex algorithm works as follows:

- Histogram equalization for a uniform histogram over the given image
- Smoothing the input image using Gaussian kernel to minimize the effect of impulsive noise (see Section 0)
- Retinex process (see Section 0)
- Enhance the dark or light details by combining the image with its inverse via hard light method for dark images or overlay method for bright images (see Section 0).
- Adjust saturation. (See Section 0 for more explanation).

Then create a binary image from the input image using the following equation.

$$BW = \begin{cases} 1, if \;\; r > th \\ 0, if \;\; r \leq th \end{cases}$$

where th is the adaptive threshold as presented in Figure 42**Error! Reference ource not found.**

4. Recover the RGB version from the binary image (Figure 44)

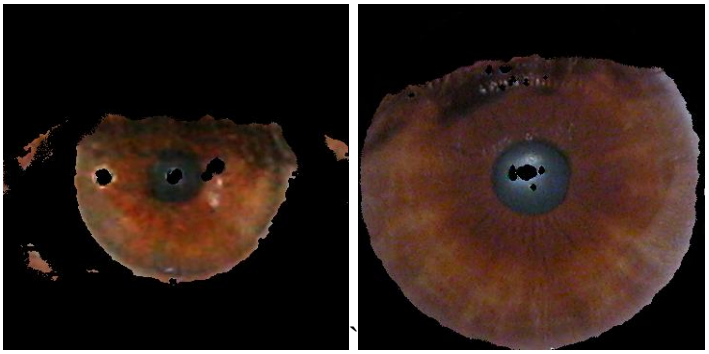

Figure 44 Segmentation Output, Before Filter (left), After Filter (right)

4.3.5 Inner Ring Segmentation Phase (Iris-Pupil)

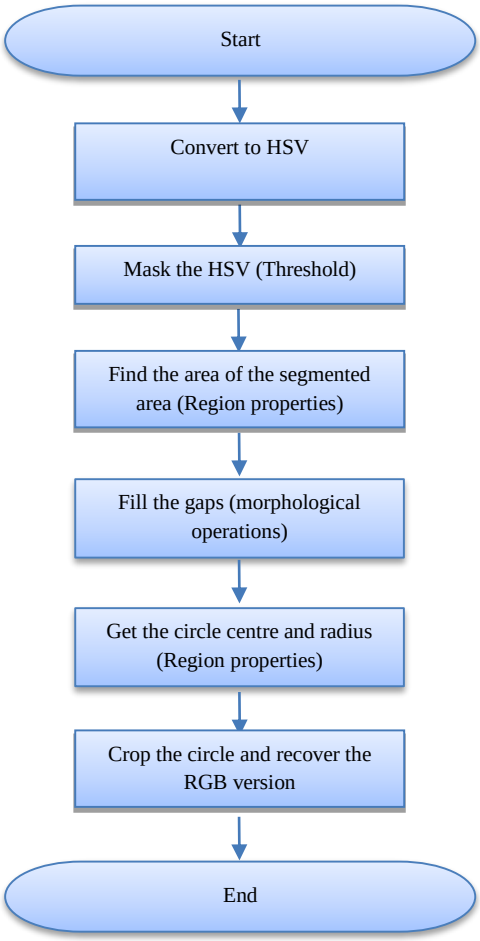

Figure 45 Flow Chart for Inner Iris Segmentation

The flow chart in Figure 45 shows the process of pupil detection and segmentation.

1. Convert the image from RGB to HSV colour space.
2. Mask and segment the local minima pixels with low intensity values representing the darkest area of image, empirical analysis and experiments led to use HSV threshold values: Hue (0.2-0.8), Saturation (0-0.5), and Value (0-0.32).
3. Apply a bank of filters to get the circular shape of pupil (region properties [111])
    - Filter size and area: This filter calculates the size of the segmented area and detects the small blobs of noise in the pupil area [111].
    - Filter creates structure: This filter fills the small gaps that were incorrectly detected as non-pupil pixels due to reflections [111].
    - Filter circle: This filter completes the shape of the pupil to circular [111].
4. Determine the pupil centre and radius [111].
5. From the detected pupil parameters, crop the pupil circle and recover the RGB image.

Figure 46 and Figure 47 show the iris image after each step from sclera detection phase to the pupil segmentation phase.

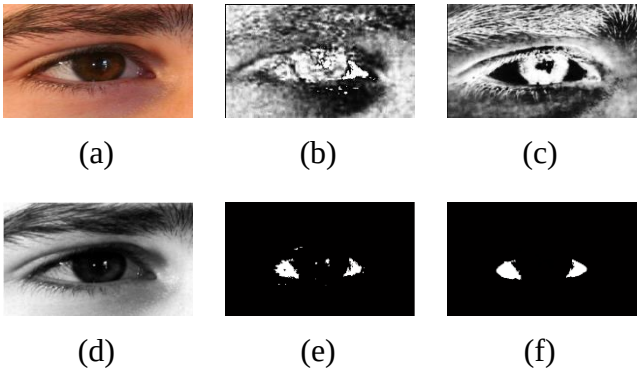

Figure 46 (a) original image, (b) Hue, (c) Saturation, (d) Value, (e) Masked image and (f) Filtered image.

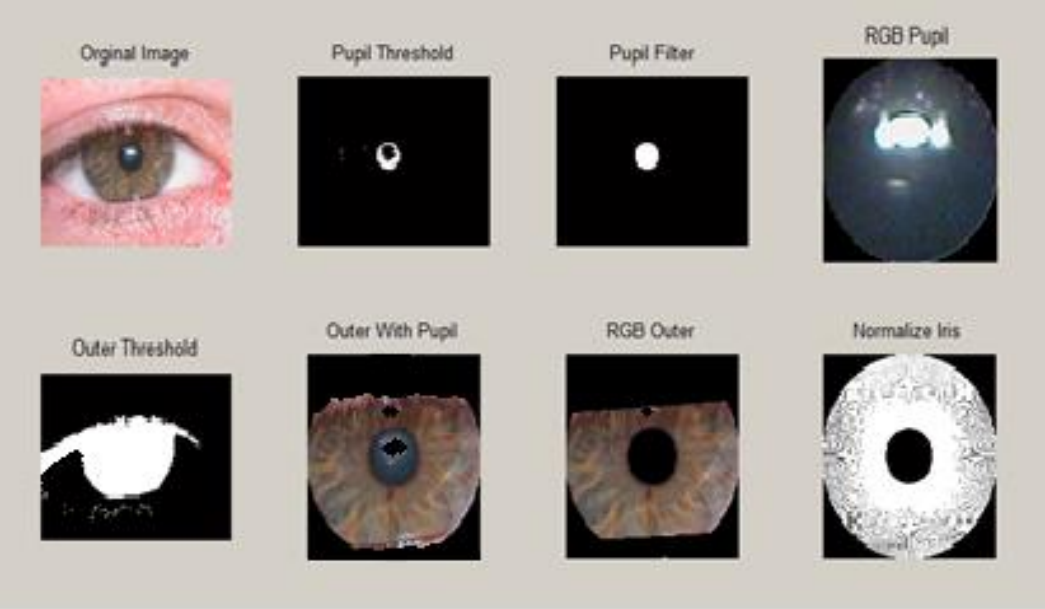

Figure 47 Output of the proposed segmentation algorithm.

4.4 Experimental Results

The proposed method was tested using three datasets (UPOL, UBIRISv.1 and UBIRISv.2). The experiments were applied on the whole UPOL database (384 images), the whole UBIRISv.1 database (1877 images) and 1000 images randomly selected from UBIRISv.2 for testing purpose called NICE.II [63]. To achieve a fair comparison, the databases and the number of sample images from each database were exactly the same as described in the literature and the stated accuracies are in percentage.

Table 4 Comparison of segmentation techniques for UPOL database

Method	*Accuracy*
Daugman's Integro-differential Operator [11]	86.82%
Wildes Circular Hough Transform [6]	95.34%
Proposed Method	99.74%

For the images of UPOL, UBIRISv.1 and UBIRISv.2 databases, the segmentation for Daugman [11], Wildes [6] and the proposed method from Table 4 have been implemented on Matlab while for the other segmentation methods [56], [50] and [58] (Table 5), the results have been taken from the literature. As seen in Table 4, the proposed method showed the highest segmentation accuracy on the UPOL database because the Daugman's integro-differential operator and Wildes circular Hough transform methods were designed to process iris images with highest quality taken under infrared light source where the colour intensity transition between the iris-sclera and the iris-pupil is significant.

Table 5 Comparison of segmentation techniques for UBIRISv.1 database

Method	*Session 1 %*	*Session 2 %*
Daugman [11]	87.64	83.98
Wildes [6]	96.52	94.84
Camus and Wildes [56]	96.78	89.29
Martin-Roche [50]	77.18	71.19
Proença and Alexandre [58]	98.02	97.91
Proposed method	99.52	99.15

Most of the previous methods depend on human visual inception to decide whether the image was correctly segmented or otherwise (Figure 48).

As described in Section 3.2.7, the UBIRISv.1 database is divided into two sessions with two weeks' time interval for image capturing. Images in session 2 have more noise factors than images in session 1. Table 5 shows the accuracy of the segmentation methods. The proposed method showed the highest segmentation accuracy in both sessions when compared to the state-of-the-arts methods. For comparison purpose, the first implemented algorithm was Daugman's integro-differential operator as it is the first segmentation algorithm used to process human eye images. This method has main advantage of its independency from any parameter values, but the obtained results showed the method's sensitivity to noise, where the segmentation accuracy degraded significantly between the first and the second session. Other similar proposals like Martin-Roche [50], Camus and Wildes [56] and Wildes [6] Circular Hough transform proved their methods robustness when applied to high quality images. However, their methods' accuracy decreases significantly when applied to images that incorporate more noise factors.

The top performing algorithm was proposed by Proença and Alexandre [58] who used the moment textural segmentation function followed by circular Hough transform. Their method proved its robustness against many noise factors apart from noise that affects the generation of edge maps like the obstruction from eyelids and eyelashes.

The segmentation accuracy was calculated through visual inception as seen in Figure 48.

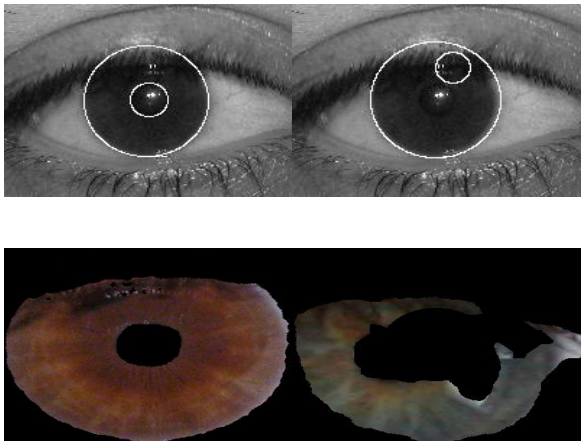

Figure 48 Accurate (left) and inaccurate (right) segmentation. The upper two images represent Daugman's method and the lower images represent our segmentation method

For testing the feasibility of the proposed iris segmentation method on UBIRISv.2 database, we followed the evaluation method as adopted by the UBIRISv.2 creator [57], who used a dataset of 1000 images randomly selected from UBIRISv.2 database known as NICE.II Noisy iris challenge evaluation dataset [63]. NICE.II provides 1000 iris images with their corresponding manually segmented template. The goal is to compare the output of the proposed segmentation method with the given templates (Figure 49). The comparison was implemented as follows:

$$E = \frac{The\ number\ of\ misclassified\ pixels}{total\ number\ of\ compared\ pixels} \times 100$$

(a) (b)

Figure 49 (a) Manually segmented (NICE.II database), (b) automatically segmented (our method) for the same image.

Table 6 Comparison of segmentation techniques for UBIRISv.2 database

Method	***Error Rate***
Daugman's Integro-differential Operator [11]	22.79%
Fourier Active Contour [21]	6.2%
Tan et al [64]	1.72%
Tan [61]	1.9%
Proença [57]	1.87%
Proposed	1.59%

Table 6 summarizes the results obtained by different segmentation methods. The first implemented method was the integro-differential operator proposed by Daugman [11] as it is the most cited method for iris images segmentation. Before applying Daugman's method to the images from UBIRISv.2 database a contrast enhancement algorithm was applied to process the normalized images.

As mentioned in Chapter 4, Daugman's segmentation method was designed to segment high resolution iris images with homogenous characteristics, and it is not suitable for segmenting noisy images with heterogeneous characteristics like those images presented in UBIRISv.2 database. Therefore, a new segmentation method was introduced by Daugman [21] which approximates the inner and outer iris boundaries in terms of "active contour based on discrete Fourier series" to address the problem of iris non-circular shape caused by gaze deviation, camera angle and the occlusion from eyelids. Although the new method showed a significant improvement in the segmentation error rate from 22.79 % to 6.2 %, it is still not suitable for segmenting images with heterogeneous characteristics.

Proença's segmentation method [57] was created specifically to segments noisy images with heterogeneous characteristics. His method creates 18 dimensional feature vectors for each pixel in the image and then feeds these vectors to feed forward neural network to decide whether the pixel belongs to the iris or not. A similar approach [64] using a random walk algorithm followed by circular edge detection method achieved 1.72 % error rate with a top performance due to image enhancement algorithm with reflection removal methods.

Methods in [57] and [64] classify each pixel from the input iris image as iris or non-iris pixels, without categorizing the input images. In UBIRISv.2 database 14 different noise factors are introduced. Therefore, it is very difficult to classify the pixels as iris or non-iris without knowing the noise factor affecting the image.

Table's 4-6 show that the proposed method achieved the highest segmentation accuracy when compared to the state-of-the-art methods (nine methods from the literature) over

three databases (UPOL, UBIRISv.1 and UBIRISv.2). The first reason for this is the coarse detection of sclera from the HSV colour space, which is more conceptual and less affected by reflections than the RGB space. This process detects the eye region apart from other face parts and minimizes the search area for the segmentation of the inner and outer iris rings. The second reason is the quality assessment process, which categorizes the input images according to their quality. Then and according to the image quality an appropriate filter is applied (e.g., Retinex (hard-light) filter for dark images and Retinex (overlay) along with Gaussian smoothing for highly reflected light images with different saturation adjust parameters), see Figure 50. In contrast, methods in [57] and [64] apply the same filters to all images regardless of the noise type.

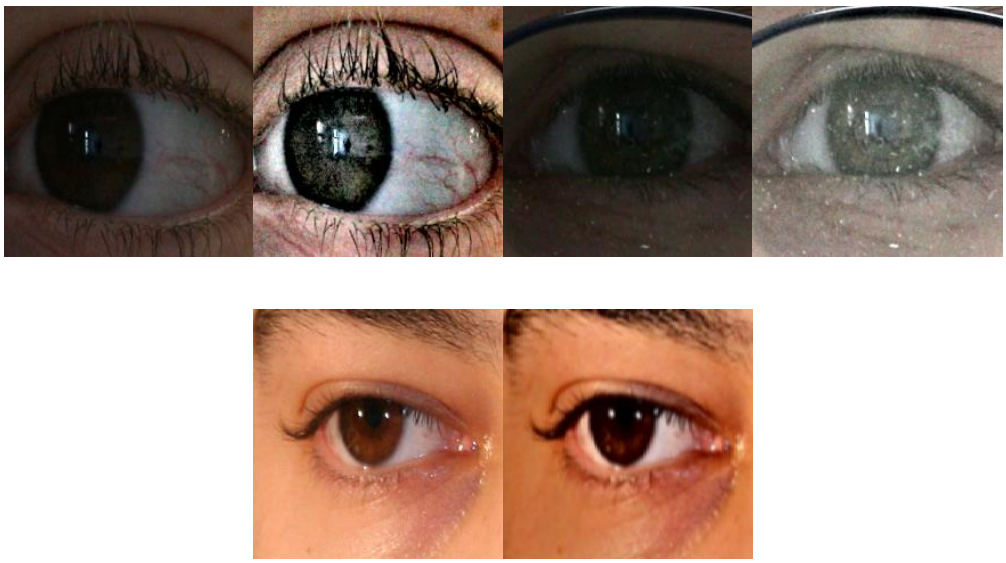

Figure 50 Example of Retinex Filter

The last reason is the binarization process, where the actual shape of the iris image is segmented (Figure 51) using an adaptive threshold according to the image quality. Unlike other segmentation methods which depend on the circular detection methods to segment

the inner and outer iris rings. Daugman [11] and Wildes [6] proposed the first circular segmentation methods for the segmentation of noise free iris images, taken under NIR light sources with look and stare and at a close distance constrains. These methods achieved high segmentation accuracy when applied to a clear iris image but their performance decreased significantly when applied to noisy images taken under visible wavelength and over distance, as there are no perfect circular rings in the iris images taken under unconstrained condition, due to occlusion and gaze deviation (Figure 51). Moreover, in the image binarization process the RGB image is converted to a binary image using an adaptive threshold according to the image quality (Figure 42), where any pixel with intensity value below the determined threshold should be masked. This process automatically segments the highlighted pixels (reflection region) without any additional filters.

Figure 51 Non-Circular iris image

4.5 Conclusion

This chapter presents a novel unconstrained iris segmentation method that adapts to the quality of the captured image. The proposed algorithm searches the HSV colour space for local maxima pixels that belong to the sclera area to reduce the influence of other eye parts. After sclera detection, a quality assessment step is applied before the segmentation process takes place to judge the image quality on the basis of global features extracted from the RGB colour space and then apply suitable Retinex filter via hard light or overlay methods on the basis of the image quality. This step enhances the low quality images, removes undesirable high reflection spots from shiny images but does not harm high quality images. According to RGB features extracted, the algorithm applies an adaptive threshold value to binarize the iris image and to detect the circular outer iris boundary. After detecting the outer ring, the cropped image is converted into HSV space to search for local minima pixels that belong to the pupil area. The proposed quality assessment process cannot be generalized to other pattern recognition systems due to its dependency on the iris RGB colours.

Chapter 5. Feature Extraction

5.1 Introduction

Most existing iris recognition systems assume ideal image acquisition, including NIR (Near Infrared) light to capture the iris image with high resolution and enough texture data. In NIR lit iris recognition systems, the iris texture is clearly revealed, as it has been captured at a close distance without light reflection.

The main aim of this research is to recognize people through their iris images which have been captured in non-ideal situations, using visible wavelength light sources, over distance and without human subject cooperation. Images with a heterogeneous characteristics that simulate the non-ideal imaging conditions were introduced in free available databases called UBIRISv.1 [47] and UBIRISv.2 [48].

Unlike NIR lights, natural and artificial visible wavelength light sources cause a reflection on the captured image which mostly hides important data that should be used to perform the recognition process. In UBIRISv.1 images were captured over 20cm distances, using visible wavelength light which causes high reflection noise, in some cases, major occlusion of eyelids and rotation, while in UBIRISv.2 database, images are classified in three categories: light, medium and heavy pigmented. In this database, both natural and artificial light sources are used. Moreover, there are 14 different types of noise in the UBIRIS database, classified into two categories - local and global noises. In the local category, the noise is caused by obstructions, reflections, off-angle, and partial images,

while in the global category the noise is caused by improper lighting, and poor focused, motion-blurred, rotated, and out-of-iris images.

In this research, the proposed algorithm will be applied for extracting features from both NIR iris images, like those images presented in CASIA database, and visible wavelength iris images from UBIRISv.1 and UBIRISv.2.

5.2 Visible wavelength iris images

Most recent iris recognition systems use an NIR (Near Infrared) light source to capture the human iris. Because NIR light sources reveal the desired iris texture very clearly, NIR enables the utilization of image filtering, which helps to block the wavelengths outside the desired intervals, these corresponds to image reflections and some small elements around the iris (such as caverns, muscle fibre etc) that cover a valuable iris texture. Nevertheless, it is also harmful to the human eye if the used illumination to light the iris area was greater than 10 mw/cm^2 cm^2 [65, 66].

In unconstrained iris recognition, the human subject could be far away from the acquisition camera. Therefore an NIR light source with illumination intensity higher than 10 mw/cm^2 cm^2 can be used, but this may harm the human eye. That is why a visible wavelength light source is used.

Moreover, if the acquisition device is a mobile phone, web cam or even a simple digital camera, a light source with a visible wavelength is usually used, because these devices do not use NIR light sources.

In most previous related works, the authors did not achieve a good result in iris recognition using visible wavelength lights because they implemented and tested their algorithms on Daugman's system without modifying the features extraction and matching techniques in accordance to the low quality iris images.

5.3 Iris Feature Extraction Techniques

Using an NIR light source in an unconstrained iris recognition system, like on-the-move and at-a-distance, is severely conditioned [10, 63]. Most of the current iris recognition systems use infrared wavelength illumination (NIR 700-900 nm). It is true that the NIR lights enable the utilization of image filtering, as those filters allow blocking the wavelengths outside the desire intervals corresponds which correspond to the image reflections that cover a valuable iris texture, and some other small elements around the iris, such as caverns, muscle fibre etc. this could affect the outer ring segmentation. However, if the human subject was far away from the acquisition device, a high power of NIR illumination light may be needed. This light can harm the human eye, according to the American and European standard boards which define the safety limits of illumination to 10 mw/cm^2. Therefore, it is prefered to use visible wavelength lights rather than NIR lights in unconstrained recognition.

5.3.1 Daugman's Method

The method proposed by Daugman [7, 11, 21] is based on wavelet demodulation for extracting features; the wavelets used in Daugman's method are Gabor filters. The Gabor

filter equation shows that the functions applied are Gaussians processed by oriented sinusoidal functions, like sine and cosine waves [7].

$$G(x, y, f) = \frac{1}{2\pi\delta_x\delta_y}\, e^{-\frac{1}{2}\left(\frac{x^2}{\delta^2 x}+\frac{y^2}{\delta^2 y}\right)} \cos\left(2\pi f(x cos\theta + y sin\theta)\right)$$

where f is the frequency of the function, δx, δy are constants that represent the space of the Gaussian along (x, y) axis, respectively, and θ is the filter orientation. In the encoding process, the iris pattern is convolved by 2D Gabor wavelet with a varying size, frequency and orientation, and then the results are quantized into one quadrant. The process of getting the phase information (Figure 52) is described by the following equation [7],

$$h_{Re,Im} = sign_{(Re,Im)} \int_{\rho} \int_{\emptyset} I(\rho, \emptyset) e^{-i\,\omega\,(\theta_0 - \emptyset)} e^{-\frac{(\gamma_0 - \rho)^2}{\alpha}} e^{-\frac{(\theta_0 - \emptyset)^2}{\beta}} \rho d\rho d\emptyset$$

where $h_{Re,Im}$ is the bit value whose real and imaginary parts are either 1 or 0, depending on the 2D integral sign; I(ρ , ϕ) is a dimensionless polar coordinate iris pattern, α and β are the size parameters of multi-scale 2D wavelet, ω is wavelet frequency, and $(\gamma_0, \emptyset_0)$ are the polar coordinates. The result after the quantization process is a binary template of 2048 bits size, with a mask template of the same size for the non-iris data, like eyelids and eyelashes.

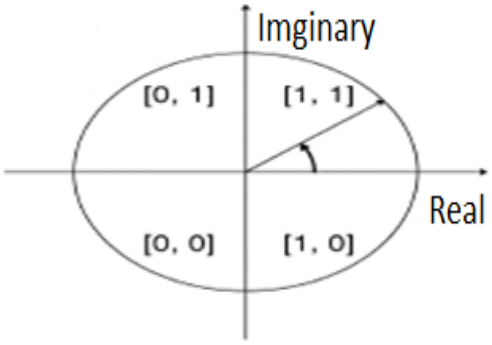

Figure 52 Phase information [21]

5.3.2 Wildes Method

Wilde's method [6] uses image decomposition at a variety of scales just like Daugman, but this method uses a different technique for the extraction of iris features. The advantages of using a multi-scale and multi-resolution structure is to extract distinguished features ranging from the overall shape of human iris (coarse details) to the tiny features (fine details). This method applies Laplacian of Gaussian filter to the input iris template at four different resolutions to perform isotropic band-pass decomposition. The features template is derived by successively applying Laplacian on the input image to form a Laplacian pyramid as shown in Figure 53. The filter he used can be specified as

$$-\frac{1}{\pi\sigma^4}\left(1-\frac{\rho^2}{2\sigma^2}\right)e^{\frac{-\rho^2}{2\sigma^2}}$$

where σ is the standard deviation of the Gaussian and ρ is the radial distance from the filter centre. Given an iris image I, let $w = [1\ 4\ 6\ 4\ 1]/16$ be a 1D mask, and $W = w^T w$ be a 2D mask is generated by calculating the outer product of a 1D mask w with itself.

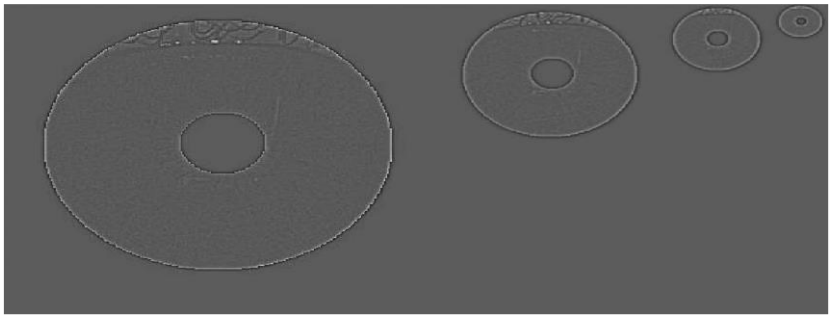

Figure 53 Wilde's pyramid

Now to form a Laplacian pyramid, a convolution process of I with W is used to produce a set of low pass filtered images gk as follows:

$$gk = (W * gk - 1) \downarrow 2$$

where $g_0 = I$, W is the window and $\downarrow$ 2 means down-sampling the image by a factor of 2. The Laplacian pyramids level is formed by calculating the difference between gk and $gk + 1$ expansion, and the expansion of $gk + 1$ is produced by up-sampling and interpolation to match the sampling rate of gk as follows:

$$lk = gk - 4W * (gk + 1) \uparrow 2$$

where $\uparrow$ 2 means up-sampling the image by a factor of 2, through insertion of zero rows and columns between all the rows and columns of the original image.

5.3.3 Wavelet Packets

Krichen et al. [67] propose the use of Gabor wavelet packets over standard Gabor wavelet to recognize the human iris, under the visible wavelength light using a standard resolution camera. The experiments were conducted on INT database [67] with a 700 visible wavelength images.

However, for the feature extraction process, Daugman proposed the use of Gabor wavelets to extract enough features from NIR iris images. Daugman's method works as follows: each wavelet consists of one mother wavelet and N number of daughter wavelets with different level of resolution. To extract enough features from iris image, 32 wavelets should be applied to different spatial locations of the image, with 4 scales and 8 different orientations. Each complex coefficient is converted into a 2-bit binary code according to the sign of its real or imaginary parts. So, 1024 complex coefficients are produced from each iris image. Thus, each iris pattern (real and imaginary) consists of 2048 bits binary code.

For the visible wavelength iris images, the Gabor wavelet is not a feasible solution to extract enough features from degraded images, since the Gabor wavelet does a precise zoom for each window partition located on the iris image. Since the original image is degraded, the zoomed windows will substantially be degraded. To solve this problem, the author introduces the use of wavelet packets, because if the size of the window to overcome the degraded zoom problem is increased, the number of iris codes will be decreased substantially, and the amount of codes will not be enough to perform a feasible iris recognition. In the wavelet packet technique, the number of wavelets involved is more than the classical wavelet, which leads to a sufficient iris code for high accuracy iris recognition.

Also, the author includes the colour information from the iris images into the wavelet packets method to improve the discrimination features of the visible wavelength images,

and he encodes the 16 million colour code to 256 colours by using the Adaptive Colour Reduction Method [67].

5.3.4 Other Iris Encoding Methods

Authors in [10, 48] state that to achieve high recognition accuracy in unconstrained iris recognition systems, three different perspectives should be considered.

1.**Amount of information:** Does the data captured from non-cooperative human subjects have enough discriminating features?

In Proença system [10, 48], both natural and artificial light sources were used from a distance of 4,5,6,7 and 8 meters to capture a free to move and at a distance human iris images with Canon EOS 5D camera.

After calculating the entropy of the captured image (which represents the amount of information contained in the image), the author concludes that the amount of information available in the images captured at (4, 5, 6, 7 and 8 meters) using visible wavelength light sources is equal to 81%, 77%, 67%, 59% and 58% of the information available in a good quality NIR image at close distance where image is captured in a cooperative scenario.

2.**Specificity:** Does the iris recognition system produce low false acceptance rate using the captured degraded image?

For specificity test, Proença extracted the signature of 1000 good quality iris images as those images used in Daugman's system and stored them in a sample database. After that, Proença used 21000 poor quality iris images like out of focus iris, partially occluded and visible wavelength iris images, and made 1 to all comparison. After conducting these tests,

Proença confirmed that even in highly degraded irises the encoding and comparison algorithms used in Daugman's system will produce almost null probability in false match.

3.**Sensitivity:** Does the iris recognition system produce low false rejection rate with the captured degraded data?

For iris images sensitivity calculations, Proença made an inter-class (comparison for FAR) and intra-class (comparison for FRR) comparison for images presented in UBIRISv.1 [47] and UBIRISv.2 [48] and concluded that the iris recognition accuracy significantly decreases as the image quality decreases, which highlights the importance of developing a new feature extraction technique to process noisy iris images with heterogeneous characteristics.

Authors in [10, 14, 48, 63] and others in [64, 68] used Daugman's approach [7] for textural features extraction to do their experiments. Another approach [69] used the Discrete Cosine Transform to extract iris textural features. Rahulkar and Holambe [70] developed a new feature extraction method based on bi-orthogonal wavelet triplet half band. They divided the normalized iris region into six partitions and selected four out-of-noise partitions for feature extraction. All the previously stated methods depend on the iris textures, and they are not suitable for on-the-move and over-distance recognition where textures are not clearly revealed.

While Hosseini, Araabi and Soltanian-Zadeh [71] introduced the pigments melanin shapes of the iris images acquired under visible wavelength light source, their method extracts three features from each window over the normalized images. These features are radius-vector function, support function and tangent-angle function.

After extracting the pigments melanin shape features from the normalized iris pattern at different resolutions, the authors fused these features with NIR textural features based on [11] to get higher classification accuracy.

Proença and Santos [72] proposed a new method for extracting features from degraded images. The method first extracts a shape descriptor of the iris boundary, based on Fourier series cumulative angular function, and then the method extracts the dominant colour descriptor based on MPEG7 descriptors. They concluded that shape and colour descriptor features achieve a recognition accuracy close to the state-of-the-art results, but without any remarkable improvements. While Raffei et al [73] proposed a new method that uses Radon transform as a multi-scale representation to down-sample the image at different scales and orientations to create the feature set, the problem of data loss, and low resolution in Radon transform translation, makes the transform unsuitable for unconstrained iris recognition.

Finally, authors in [74, 75], used the Curvelet transform to extract features from iris images captured in NIR and visible wavelength light sources. But in their work they used the first version of the Curvelet transform which is a very complex and coefficient redundant technique as well as they converted the Curvelet coefficients to a binary code, which weakens the Curvelet coefficients strength.

5.4 Proposed Method

As stated in Chapter 4, the unconstrained iris recognition system should be able to process noisy images that have heterogeneous characteristics. One of the main noises that affect

the iris images in UBIRISv2 database [48] is the capturing distance (up to 8 meters), where the tiny details of the iris texture is not clear, see Table 7. Although the images presented in UBIRISv2 database have been cropped manually from the captured face, so that the iris recognition researchers will not be concerned with eye detection processes, but still the texture quality of the images is very low due to distance capturing and different lighting conditions.

Table 7 Calculated pixel resolution according to imaging distance

Light used	Visible wavelength, natural and artificial	
4 meters	≈ 180 pixel	Entropy≈ 3.4×10^{-4}
5 meters	≈ 140 pixel	Entropy≈3.39×10^{-4}
6 meters	≈ 120 pixel	Entropy≈3.35×10^{-4}
7 meters	≈ 90 pixel	Entropy≈ 3.3×10^{-4}
8 meters	≈ 70 pixel	Entropy≈3.28×10^{-4}

Many researchers [10, 48, 76-79] have focused on increasing the segmentation accuracy and proposed various techniques to segment the noisy iris images, but in the feature extraction process they either used the algorithm proposed by Daugman [7] or they used another texture feature extraction algorithm such as [69, 80].

As the textural features are the tiny patterns presented in the image, the capturing distance and lighting conditions will affect the amount and the quality of these tiny features. In some cases the capturing device will not be able even to capture these features. Thus, the textural features extraction is not a robust method when applied to images that have been

captured over long distance under poor lighting conditions. Therefore, the second main contribution of this research is to extract 2D geometrical features from the human iris in addition to the textural features by utilizing the Curvelet transformation.

5.4.1 Curvelet

The Fourier transform requires a huge number of terms to represent a discontinuity with high accuracy (Gibbs phenomenon). Then the wavelet transform came to solve the weakness of Fourier, by localizing the signal at multi scales, while Wavelet performs well in one dimension, it is still weak when "representing higher dimensionality due to limited orientation selectivity and isotropic scaling" [81]. The Curvelet transform has a higher dimensionality representation (Figure 54) than wavelets and other transforms [82] (Table 8).

Table 8 2D Transforms and their features

Transform	Description
Steerable wavelet [83]	Rotation and Translation invariant paid by high redundancy
Gabor wavelet [84]	Fast but the number of orientation in each scale is limited.
Contourlet [85]	Fast but the directional geometrical features is less clear than other 2D transforms.
Shearlet [86]	Very redundant, and the parameters returns the scale, direction and translation, but the discriminating features selectivity is very complex.
Bandlet [87]	Strong performance for 2D singularities, but the computational complexity is high

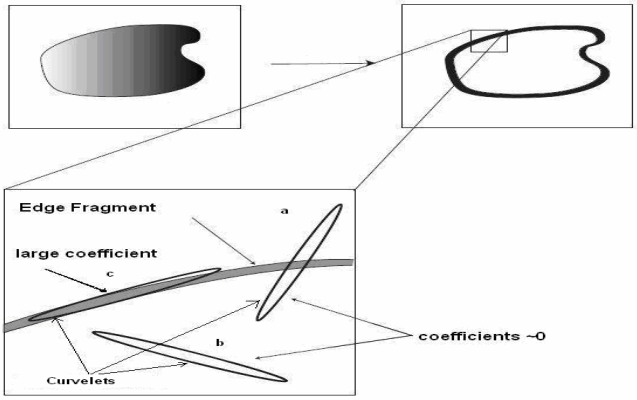

Figure 54 Curvelet coefficients (a and b) represent zero coefficients while (c) represents a discriminating coefficient [81]

The main idea here is that the edge discontinuity is better approximated by Curvelet than wavelets (Figure 55). The Curvelet transform provides a solution to the limitations that the wavelet transform suffers from [81] such as curved singularity representation, limited orientation and absence of anisotropic element. Curvelet has strong mathematical properties that can accurately represent the singularity of curves in non-adaptive manner. In other words it can be considered as a higher dimensional generalization of the wavelets.

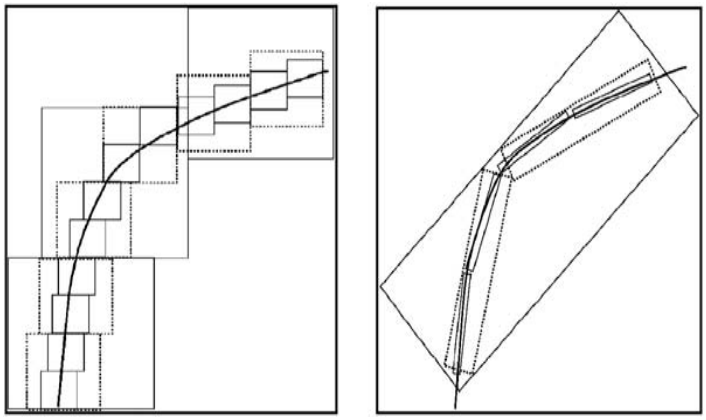

Figure 55 Wavelet (left) against Curvelet (right) [81]

Curvelet transform is a new generation of multiple scale representation. This contains information about the scale and location parameters. Unlike wavelets, it also contains the directional parameters.

The directional or orientation selectivity behaviour in Curvelet transform helps to represent objects with curves as well as handle other one-dimensional or two-dimensional singularities much better than the wavelet transform [88]. This makes the Curvelet transform a more accurate transformation for many image applications such as feature extraction, compression, image de-noising and enhancement. Figure 56 shows the scale (4 scales), position (the largest coefficient where the feature curve fit into a shear, see Figure 54 (c)) and orientation (multiple orientation in each scale) of Curvelet coefficients.

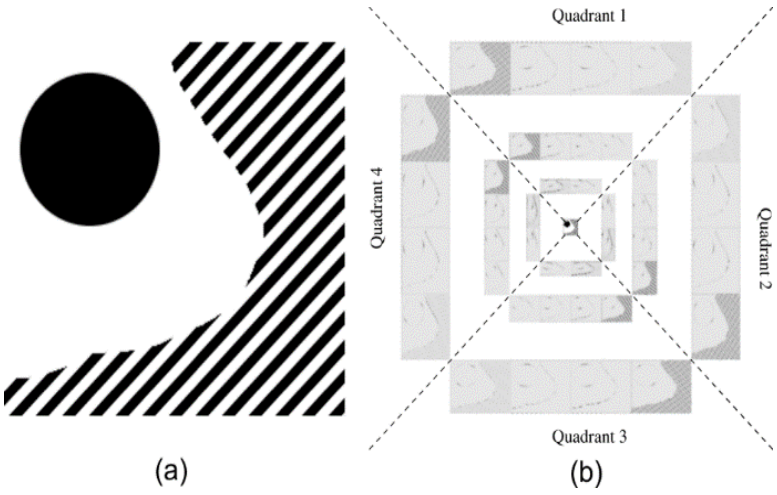

Figure 56 (a) Original image, (b) Curvelet coefficients

5.4.2 Description of Curvelet Transform

1. **2D FFT of the image is taken (Cartesian Frequency Plane) and obtain $\hat{f}(n_1, n_2)$**

Extract the frequencies from the image.

2. 2D Fourier frequency plane is divided into shears (Wedges)

According to anisotropic scaling law [82]: curves features can be extracted through shear shaped windows which obey the parabolic scaling $Length \approx Width^2$ (Figure 57).

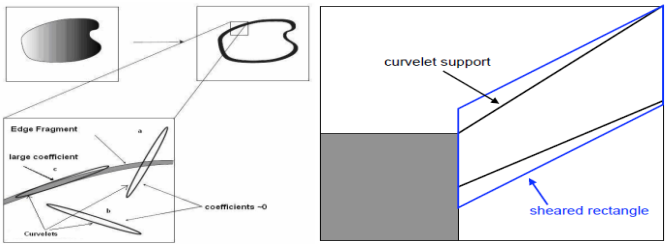

Figure 57 Curvelet shear [81]

Decomposition scaling law: $[\mathbf{2^{2j}, 2^{2j+2}}]$. The number of scales is proportional to the image size; large images have more scale divisions than small ones. For example, a 512×512 image will have seven scales.

The size of the 2D Fourier array at the coarse scale is one-third of the original array size, and the size of the array at the fine scale is one/third of the previous scale. The frequency plane is divided into two directions. The concentric squares are responsible for the decomposition of the input image into multiple scales, and the angular division divides the band passed image into different angles and orientations as shown in Figure 58. Each shear is indexed with scale j, angle $\emptyset$ and position(x, y). Each shear corresponds to a particular Curvelet with scale j and angle l. Each shear can smoothly extract frequencies near the dyadic corona ($2^j \leq r \leq 2^{j+1}$) and near the angle ($-\pi . 2^{-\frac{j}{2}} \leq \emptyset \leq \pi . 2^{-\frac{j}{2}}$)

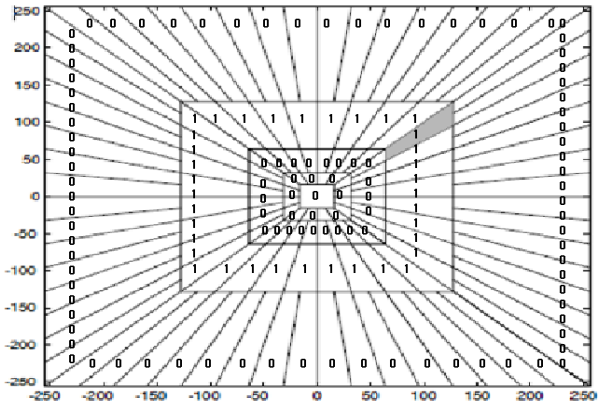

Figure 58 Curvelet scales and frequency distribution

The shaded scale in Figure 58 will be used to demonstrate the process of Curvelet in extracting coefficients with orientation, scale and position parameters. For example, a 2D-Fourier array of an image is divided into five scales. The first scale represents the low pass filter and the remaining scales represent the high pass filters. These scales must be masked (set to zeros) except for the one that the Curvelet coefficients will be extracted from (set to 1). A number of windows (wedges) are placed over the chosen scale. These windows will start reading frequencies with all possible orientations by drawing a window with no rotation. This window will extract the coefficients of vertical edges, red colour window (Figure 59), and then it will start to draw the other windows with different orientations to find curve singularities. This process continues until all the coefficients are obtained from the scale.

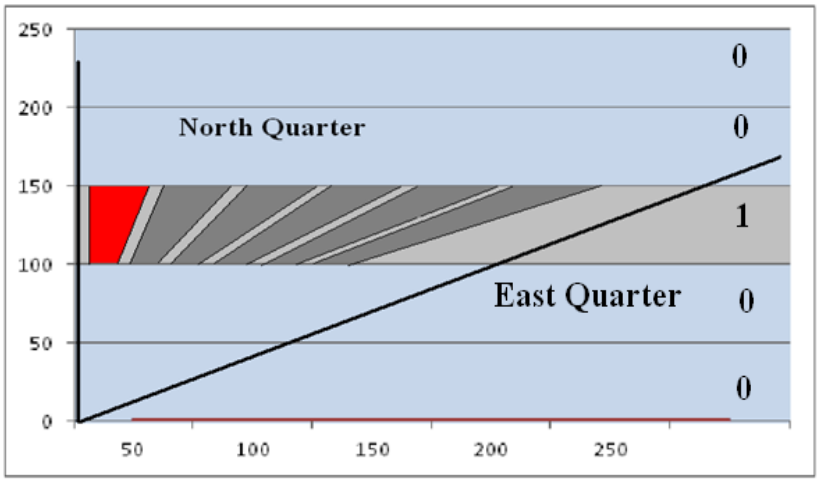

Figure 59 Wedges (shears) orientations

Each quarter corner is mirrored by Mirror Extension (ME) (Figure 60).

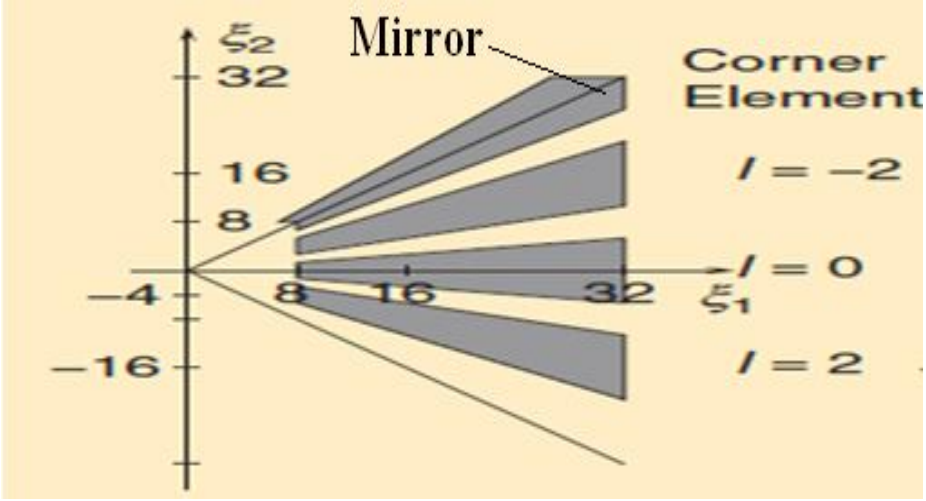

Figure 60 Mirror extension [82]

Within all shears $p_{j,l} \coloneqq \{(n_1, n_2 + n_1 \tan \emptyset_{j,l})\}, n_1, n_2 \in p_{j,l}$ (where $p_{j,l}$ is a parallelogram containing the support of the discrete localizing window $\widetilde{U_{j,l}}[n_1, n_2]$) and find out where the maximum frequency is.

3. **For each scale j and angle l multiply the sheared object $\hat{f}$ with the parabolic window: and form the product $\widetilde{U_{j,l}}[n_1, n_2]\hat{f}[n_1, n_2]$.**

To effectively localize $\hat{f}$ near the parallelogram with orientation$\emptyset_{j,l}$, the Fourier coefficients that have the maximum values inside the wedge should be multiplied with the wedge parameters (orientation, scale, position).

4. **Inverse 2D FFT for each shear $\hat{f}_{j,l}$ via Wrapping to obtain Discrete Curvelet $C^{d}_{j,l,k}$**

In the frequency plane the window $\widehat{U}_{j,l}[n_1, n_2]$ does not fit in a rectangle of size $2^j \times 2^{j/2}$ in which 2D IFFT could be applied. So the wedge coefficient should be wrapped around the origin to fit inside the Fourier windows (Figure 61).

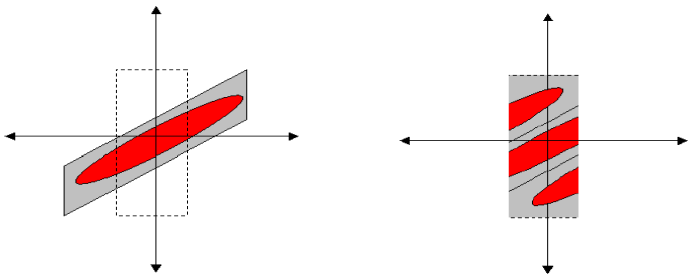

Figure 61 Wrapping

5.5 Rotation Invariance

As this research title implies, a person should not need to co-operate with the acquisition camera to capture his/her iris image. While the person moves his head, the camera also tilts right and left, i.e., the eyes also move. So, it is important to correctly recognize the human iris even if the iris is rotated.

Iris rotation is one of the most important issues addressed in the state-of-the-art systems. According to experiments, Daugman's system does not correctly recognize sharply rotated iris images. Although Daugman's system uses the bit shift technique, it is not suitable for unconstrained iris recognition systems because the bit shift technique has been developed to correct the misalignments in a normalized iris image caused by noise or minimal head rotation, not for sharply rotated images.

5.5.1 Related Work

For iris rotation, Daugman proposes a method of shifting the iris template bits to the left and right [7]. The number of bits in each shift should be twice the number of filters used because each filter represents a single pixel in the normalized iris template with two bits of binary code. Hamming Distance values are then calculated from successive shifts until the best match occurs.

Daugman's system uses the Hamming Distance (HD) to find the similarities between the two iris templates. In HD each bit in the binary template generated from the normalization process is compared with millions of iris templates stored in the database. So when the rotation occurs the matching result will not be accurate because the binary template will be shifted.

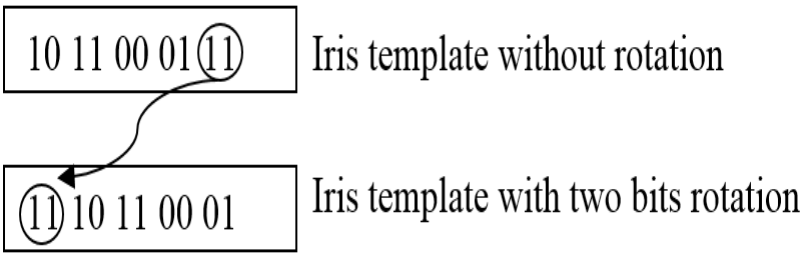

Figure 62 Bit shift process in Daugman's system

Figure 62 illustrates the shifting process in Daugman's system. In each shift the system rotate the template code two bits left and two bits right. This is an example of one filter encoding. Hence, only two bits are moved during a shift. Here, an HD of zero will be the best match.

The system solves slight rotation problems. In addition, Daugman's system, and many other systems used, store multiple images for the same iris at different orientations (which means that they store 6-10 images for each iris) to overcome the rotation problem, which increases the processing time and consumes more memory space. This system is applicable for lightly rotated iris images but not suitable for sharply rotated images. Another approach [69] achieved a rotation invariant recognition by storing six iris codes for rotation angles of 4, 8, and 12 pixels in each horizontal direction, and compare the extracted iris code against seven stored codes (six rotated and the original one) and choose the minimum distance. [89], Monro and Rakshit uses 1D Fourier domain cross correlation to estimate the rotation between two iris images. This eliminates the need to store multiple iris codes for different orientations and only stores one code for the iris and the discrete Fourier transform of annular ((Ring)) segments derived from the enrolled iris.

The use of 1D circular cross correlation in the discrete Fourier transform instead of 2D will reduce the amount of saved data (iris code) and increase the speed of matching.

Monro and Rakshit [89] system is used to calculate the amplitude of a feature vector and its inverse of the captured and enrolled images. When a sharp peak of features occurs, the system will search the nearest feature vector, calculate the position of the peak and compare it with the position of the nearest enrolled image. If a difference in position exists, a non-match result will occur. So the system will start to shift the resulting feature's sharp amplitude until there is a match.

Recognition accuracy of 75.6% [89] was achieved using modified images from the CASIA database [40] with a processing time of 12 times shorter than Daugman's system.

In [90], Monro and Rakshit also propose another method of solving the problem of rotation by estimating the motion in a sequence of video frames to determine the rotation angle in human iris.

In this method, the author compared a macro block from any selected video frame with the same macro block in the previous and next frames to calculate the amount of displacement, which is important for computing the motion vector that can be used in the matching process.

A match result for two images of same iris image is shown in Figure 63 (a) which shows the vector magnitude is very low and the orientation of the vectors are correlated - unlike (b) which represents the vector results of two different images with high magnitude and random orientation. The comparisons of multiple video frames macro blocks is

computationally expensive, also the idea behind the system is built on estimations, in which accurate results cannot be ensured.

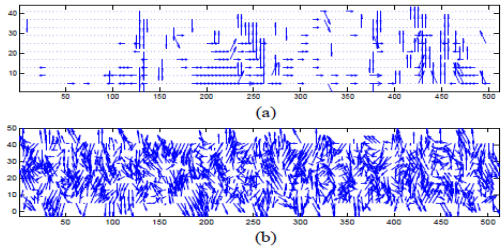

Figure 63 Plots obtained by motion estimation between two normalized images (a) Match (b) Non-Match [91]

Takano and Nakamura in [91] proposed a method to detect the orientation of the iris image using the iris itself, not using the outer facial environments, by applying neural network algorithms called R-SAN net to the recognition system.

In this system, the iris image is transformed into a polar pattern. After sampling the pattern into a spreading layer, a periodic Gaussian is applied to get a spread pattern. To do the learning, each iris should be stored in a matrix with its orientation, for example if there are 10 irises and 6 different orientations for each iris, then the number of learning patterns will be given as 10 (iris) × 6 (orientation) = 60; all of these patterns are then stored into a memory called memory orientation matrix.

Finally, the orientation recognition neurons will recognize the orientation in the given image using the population vector method [91]. This method can detect the orientation of the any given pattern by synthesizing the continuous spectra of the outputs of the

orientation recognition neurons. However, this system is still computationally expensive and its complexity should be reduced.

Matschitsch, Stögner, and Tschinder [92] improved the rotation invariant systems that work on a 1D spatial domain, like the Monro system, by extending the iris data template from mean vectors to 2D histogram information. The system improved the FAR in rotated images, but the FRR values were high.

Another proposal by M. Islam, Z. Dengsheng, and L. Guojun [81] solved the problem of rotations in the feature extraction process. The proposed method solves the rotation problem by arranging the mean energy in the feature vector array. The feature vector changes significantly, when the image is rotated, the maximum and the second maximum mean energy will appear at different locations in the feature vector. This will cause a large feature distance in the recognition process. The idea is to rearrange the features energy values based on their dominant orientation. Because the maximum and the second maximum mean energy appears together.

The rearrangement of utilizing the first and second dominant direction energy at the beginning of the feature vectors array and shifts the rest circularly also the mean energy at other scales is arranged in a similar way. Since the mean energy defines the dominant orientation, the standard deviation of different sub bands is rearranged in the same order of the mean. This enables the Curvelet feature vectors to be rotation invariant.

In this example, the Curvelet uses four sub bands to extract the mean energy features from any given image as seen in Figure 64, i.e. total of $26 = 1 + 8 + 16 + 1$ Curvelets coefficients are used. Thus, a feature vector of $52 = 26 * 2$ is created for each image.

This proposal works well when the input image is clear and whole portion of the image is included in the feature extraction process. However, in our case, the upper and lower extremes might be occluded by eyelids, and some portion of the iris image also might be excluded due to severe noise. Thus, this technique is not suitable for unconstrained recognition.

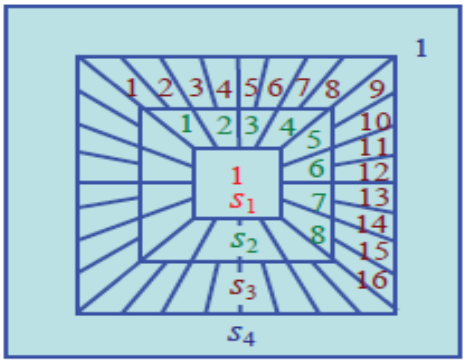

Figure 64 Frequency spectrum coverage of Curvelet using four sub-bands [62].

5.5.2 Proposed Rotation Invariance Method

As stated above, many proposals have been introduced to address the limitation of iris rotations, these techniques were applied to the iris recognition system either in the features extraction or in the template matching phase. While the proposed solution for rotational invariance iris recognition is based on human eye geometry, and applied during the sclera detection process. The method searches for both left and right eye corners $(x_1, y_1)\ and\ (x_2, y_2)$ respectively pointed as A and B in Figure 65. (Refer to section 4.3.1 for further explanation).

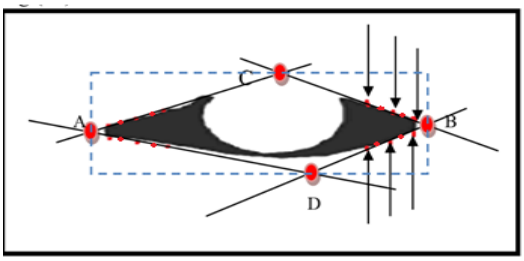

Figure 65 Detected Iris Corners

5.6 Curvelet implementation

To extract the features from iris images using the Curvelet transform, first the segmented image should be normalized to a predefined size using Daugman's rubber sheet model [21]. Then, a Laplacian sharpening filter is applied over the normalized images to enhance the lines and edges (geometrical features) as shown in Figure 66. Here we used the implementation of Masek [22] to perform the normalization process, with radial resolution of 256, and angular resolution of 256 as shown in Figure 66.

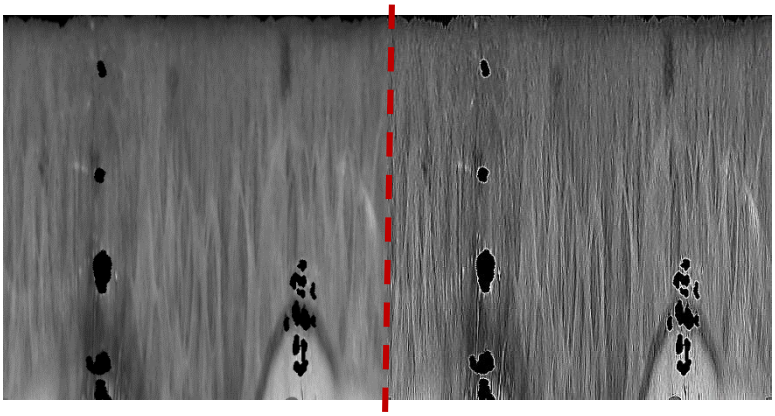

Figure 66 Normalized iris

After the normalization process, the rectangular iris template is passed to the Curvelet transform for features extraction.

The number of scales for ($N \times N$) image is automatically defined by Curvelet according to the following equation $Scale = log_2(N) - 3$ where N is the horizontal resolution of the image. So the default number of scales for (256×256) image will be 5. Each scale is divided into several partitions with different orientations. The first scale which uses the low band pass filter is not divided and it is just one matrix that holds the coarse details of the input image. Each scale apart from the first low pass coarse scale, passes the image under higher pass filter to get the finer details from the input image. The number of shears in each scale is $(1, 16, 32, 32, and\ 64)$ for the first, second, third, fourth and fifth scale respectively.

The main disadvantage of Curvelet is the redundancy of the extracted coefficients, because at each scale the Fourier frequency plane is passed to each scale at different orientations, but we are interested in the oriented shear that returns the maximum only, where the feature fits inside the shear like 'c' in Figure 54.

Many researchers like [93, 94], use the PCA (Principle Component Analysis) as a dimensional reduction technique to minimize the size of the output Curvelet coefficients, but as described in [95], the PCA accuracy is dependent on the size of the input template, where the PCA fails to select the feature of interest in a larger dataset.

As described earlier in this section, the features of interest from Curvelet transform, will be the coefficients with highest values. Therefore, 1024 coefficients with the highest values were extracted from each scale, selected equally from all orientations (shears), as in our case the frequency plan is divided into 5 scales, then the number of discriminating features will be $1024 \times 5 = 5120$ features, divided as follows: from the first low pass

scale, the highest 1024 features are extracted from scale as there are no oriented shears in this scale; from the second scale, the 1024 features are extracted from the 16 shears equally ($1024 \div 16 = 64$); features from each shear, the next scale with 32 oriented shears ($1024 \div 32 = 32$); features from each shear, and the last scale of 64 oriented shears a total of 16 features extracted from each shear.

The reason for selecting this amount of features from the whole Curvelet coefficients, is the Curvelet ability to reconstruct the curves continuities of the input image using 1% from the Curvelet coefficients as described by the patent from [96]. Figure 67 shows that the original image can be reconstructed using 10% from the Curvelet coefficients.

Figure 67 Reconstructing image from Curvelet coefficients

Finally, the 5120 discriminating features are stored in 1D feature vector for classifications.

5.7 Matching

As described in the background chapter, many techniques are used for matching the output template with the stored templates, depending on the nature of the features. The most widely used techniques in the literature are Hamming distance (HD) [7] [97], and Euclidean Distance (ED) [98] [99], since the Curvelet coefficients are real numbers, the implementation of HD is not possible, because the HD calculates the dissimilarities

between binary templates. In addition, it is very difficult to work with Euclidean distance when comparing a large data set. As our template consists of 5120 values, the resultant ED will be very high and unpredictable, due to the sum operation in calculating the distance, as shown:

$$ED(a,b) = \sqrt{\sum_{1}^{n}(a_i - b_i)^2}$$

where a is the stored feature vector and b is the extracted feature vector. In unconstrained recognition, the probability of getting the exact feature value from a subject using two different imaging sessions under variant imaging conditions is very low. Therefore, the occurrence of any miss-segmented pixel, any interference from eyelashes, or even the presence of reflections, will produce a very high distance, which will affect the whole recognition process.

Another approach for distance calculation that addresses the limitations of ED is the L_0 distance, which can be described as follows:

$$L_0(a,b) = \sum_{1}^{n}\frac{\mathbb{1}(|a_i - b_i|)}{n}$$

$$a = (a_1, \dots \dots a_n)$$

$$b = (b_1, \dots \dots b_n)$$

where $\mathbb{1}(a_i = b_i) = \begin{cases} 1 & if\ (a_i = b_i) \\ 0 & if\ (a_i \neq b_i) \end{cases}$

As described earlier in this section, the probability for the value of ($\boldsymbol{a}$) created from input iris image that has been captured under unconstrained conditions, to be exactly equal to its correspondent ($\boldsymbol{b}$) from a stored iris template, is very low. Therefore, a little modification should be made to calculate the distance as follows.

$$L_0(a,b) = \sum_{i=1}^{n} \frac{\mathbb{1}(|a_i - b_i| \leq 5)}{n}$$

$$a = (a_1, \dots \dots a_n)$$

$$b = (b_1, \dots \dots b_n)$$

where $\mathbb{1}(|a_i = b_i|) = \begin{cases} 1 & if\ (|a_i - b_i|) \leq 5 \\ 0 & if\ (|a_i - b_i|) > 5 \end{cases}$

where n =5120 is the size of feature set. The resulting distance will be in the range between [0, 1], where 1 means no match and 0 means complete match.

5.8 Evaluation and Experimental Setting

The databases that best meet the requirements of the proposed algorithms are UBIRISv.1 [47] and UBIRSv.2 [48]. This is because when SOCIA Labs planned to create the UBIRIS databases they had three basic goals 1) To acquire the iris images of moving subjects 2) To acquire the iris images at varying distance and 3) To acquire the iris images under different lighting conditions. These roles incorporate the noise effects that result from unconstrained humans and varying lights conditions.

For evaluation, the proposed feature extraction method was tested using two datasets (UBIRISv.1 and UBIRISv.2). The experiments were applied to the whole UBIRISv.1 database (1877 images) and 1000 randomly selected images from UBIRISv.2 (NICE.II).

5.8.1 UBIRISv.1

Table 9 - 10 show the results for UBIRISv.1 database. These results have been evaluated using two different methods. Table 9 shows the recognition rates of the two sessions of the database.

Table 9 Recognition rate UBIRIS V1

Method	*Session 1 %*	*Session 2 %*
Daugman [11]	90.80	86.71
Wildes [6]	72.40	71.24
Farouk, Kumar, and Riad [100]	97.17	--
Proposed method	99.63	99.35

The second evaluation method is the verification rate for intra and inter class comparisons known as FRR and FAR. Table 10 shows the FRR and FAR for UBIRISv.1.

Table 10 UBIRISv.1 FRR and FAR

Method	*FRR %*	*FAR%*
Daugman [11]	21.47	0.001
Wildes [6]	22.95	0.001
Mayank, Vatsa, Singh, and Noore [101]	7.35	0.0001
Radman, Zainal, and Jumari [62]	18.30	0
Proença [14]	16.49	0
Rahulkar and Holambe [70]	0.49	0.52
Proposed method	5.82	0

Figure 68 shows the ROC curve for UBIRISv.1 database. It is obvious that the FRR is inversely proportional to FAR under different dissimilarity threshold values, the higher the dissimilarity threshold value the higher the FAR and the lower FRR (Figure 69).

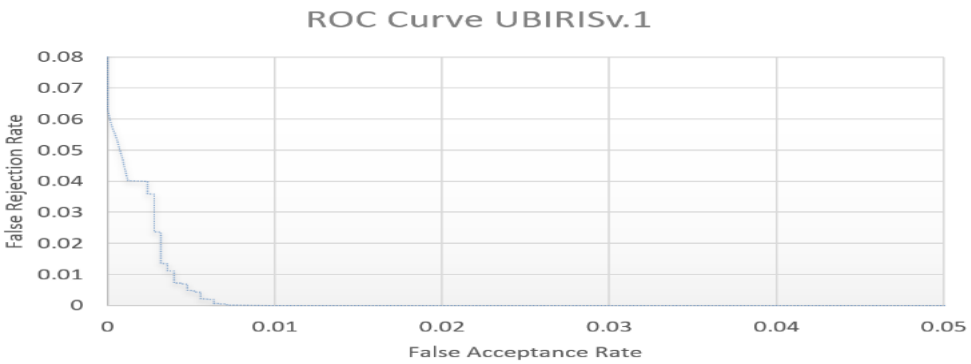

Figure 68 FRR and FAR for UBIRISv.1 Database

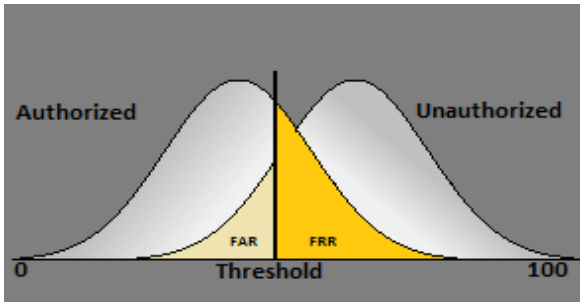

Figure 69 Threshold for FRR and FAR

The FRR can be calculated as

$$FRR = \prod_{i=1}^{n} \frac{Prob\left(Dist_i^I > Th_i\right)}{N_i}$$

where $Dist$ is the L_0 distance between two iris templates (Section 5.7) for intra-class comparisons, Th is the threshold used, 0.31 and 0.33 for UBIRISv.1 and UBIRISv.2 respectively, I stands for intra-class, and N is the number of intra-class comparisons.

The FAR can be calculated as

$$FAR = \sum_{i=1}^{n} \frac{Prob\left(Dist_i^E \leq Th_i\right)}{Q_i}$$

where E is the inter-class comparisons, and Q is the number of inter-class comparisons. We used Matlab built-in function called Prefcurve to calculate the FRR and FAR, with 95% confidence interval. More details are given in Appendix B.

The accuracy of the recognition system using the proposed feature extraction algorithm based on the Curvelet transform was compared to seven different recognition systems. Each system uses its own segmentation algorithm (Table 9 and Table 10). The first implemented method was Daugman's method based on 2D Gabor Wavelet [11]. This method scores 90.80% and 86.71% for the first and second sessions of UBIRISv.1 database. The significant decrease in the results between two sessions proves that this method is not suitable for extracting features from noisy iris images. Wildes [6] used a different feature extraction method based on Laplacian pyramids to extract textural features from iris images. The accuracy of Wildes' system is lower than Daugman's, because of the anisotropic scaling (orientation selectivity) of 2D Gabor transform used by Daugman can approximate the 2D features from degraded images in a better way than the isotropic scaling of Laplacian transform.

Proença and Alexandre [14] used the same approach as Daugman. Authors in [100] used the same approach of Daugman but they used a multidimensional neural network for matching to improve the system efficiency. Radman, Zainal, and Jumari [62] used an image enhancement pre-processing and a modified version of Integro-differential operator for image segmentation to improve the whole system accuracy.

Mayank et al [101] extract two distinct features (local and global). Euler numbers method is used to extract the local topological features and 1D log-Gabor transform to extract the global iris textural features. While Rahulkar and Holambe [70] with top performing method used a feature extraction algorithm based on triplet half band filter bank to extract a discriminating features from degraded iris images, their method is rotation invariant and have a high performance on frequency selection and localization. Moreover they apply a K out of N post classifier over the extracted coefficients to reduce the FRR of the system.

5.8.2 UBIRISv.2

Table 11 – 12 show the results for UBIRISv.2 database. These results have been evaluated using two different methods. Table 11 shows the recognition rates of the database.

Table 11 Recognition Rate UBIRISv.2 database

Method	*Recognition Rate*
Daugman [11]	38.39 %
Wildes [6]	34.30 %
Proença [10]	63 %
Proposed method	75.34 %

To test the robustness of our feature extraction method on UBIRISv.2 database, we compared our system to the three top performing systems given by NICE.II evaluation committee and verified by the UBIRIS creator in [72], along with Daugman and Wildes feature extraction methods.

Table 12 UBIRISv.2 FRR at FAR= 0.01

Method	***FRR %***
Daugman [11]	67.82
Wildes [6]	69.04
Wang et al. [102]	47.58
Proença and Santos [72]	45.03
Tan et al. [68]	41.62
Proposed method	29.36

Each recognition system mentioned in Table 12 uses a different feature extraction algorithm with its own image enhancement and segmentation method. The first implemented system was Daugman's system based on the phasor features extracted using 2D Gabor Wavelet [11]. The second implemented system was Wildes' system based on Laplacian pyramids to extract textural features from the iris template. While both systems achieved high performance when applied to high quality iris images, their accuracy decreased significantly when applied to noisy images. The low performance of these

systems is not only caused by their feature extraction methods, but also to their segmentation techniques.

Wang et al. [102] used a modified version of Daugman's system, where they used the Integro-differential operator for segmentation followed by the rubber sheet model, then the normalized iris pattern is passed to a learning algorithm called Adaboost [102] to classify whether the iris images were correctly segmented or not, and finally a 2D Gabor wavelet is applied for features extraction. Proença and Santos [72] proposed a new method for extracting features from iris images with heterogeneous characteristics. The method first extracts a shape descriptor of the iris boundary based on Fourier series cumulative angular function, and then the method extracts the dominant colour descriptor based on MPEG7 descriptors. They conclude that shape and colour descriptor features achieve a recognition accuracy close to the state-of-the-art results, but without any remarkable improvements.

Tan et al. [68] used a modified version of Daugman's Integro-differential operator for segmentation followed by rubber sheet for normalization, then they used four different methods for feature extraction. The first two features sets are ordinal measures and colour analysis for the iris region, the second two feature sets are texton (micro structures) representation and semantic information for the eye region. Finally a score level fusion is applied to the feature sets to find the dissimilarities between two images.

The Curvelet transform used in the proposed method were applied over 256 × 256 normalized image (five rows from the top and bottom of the image where excluded to get rid of noises around the iris and pupil) at 5 scales with multiple orientation at each scale

(Figure 70), a total number of around ≈ 300,000 coefficients where extracted. As the Curvelet transform returns the maximum coefficient values when the geometrical curves and lines fit exactly inside the shear, the maximum 1024 coefficients from each scale forming 5120 features set (approximately 2% from the whole coefficients) were selected. The strength of Curvelet transform in this case is that, it depends on 2D geometrical features rather than the tiny textural features like other transforms and as we used iris images captured over distance up to 8 meters and using several lighting sources, then the textural features presented by these degraded images are not reliable (Figure 72).

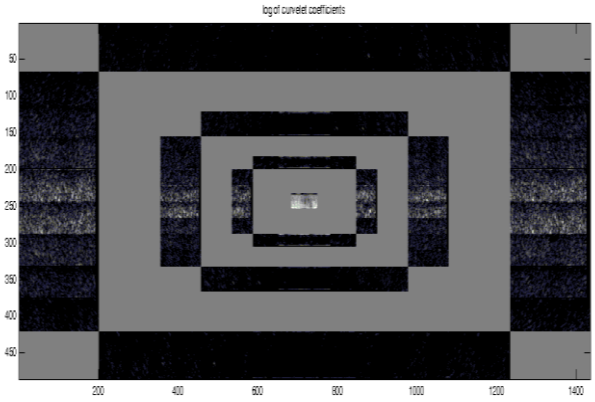

Figure 70 Curvelet Coefficients

To improve the performance of Curvelet transform, a Laplacian sharpening filter is applied over the normalized image to enhance the 2D edges (Figure 71). In unconstrained conditions the tiny textural features are not stable under different lighting conditions and over different imaging distance (Figure 72). While the bold geometrical features is less affected with noise than the tiny textural features.

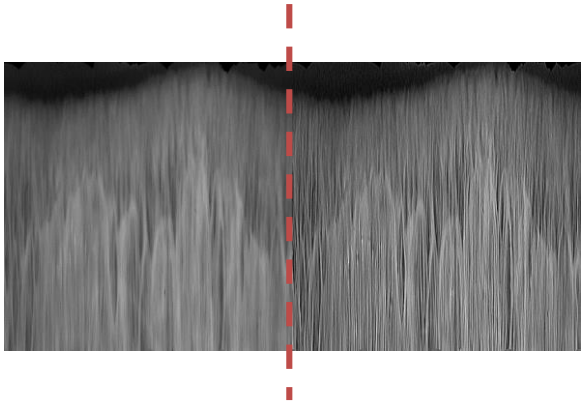

Figure 71 Before Laplacian (left), After Laplacian (Right)

Figure 72 Two images for the same iris under different imaging conditions

Each system stated in Table 12 used its own pre-processing and segmentation technique, which in turn affect the strength of the extracted features as well as the matching accuracy. To measure the robustness of the Curvelet transform in extracting features from degraded iris images away from the effect of segmentation process, we used the 1000 images from NICE.II dataset that have been manually segmented, then these images were processed by rubber sheet model for normalization and passed to the Curvelet transform as well as to Daugman's 2D Gabor transform. Table 13 shows that the proposed feature extraction method outperforms Daugman's benchmark method.

Table 13 FRR for UBIRISv.2 Database at FAR= 1%

Method	***FRR %***
Daugman	37.38
Proposed method	15.14

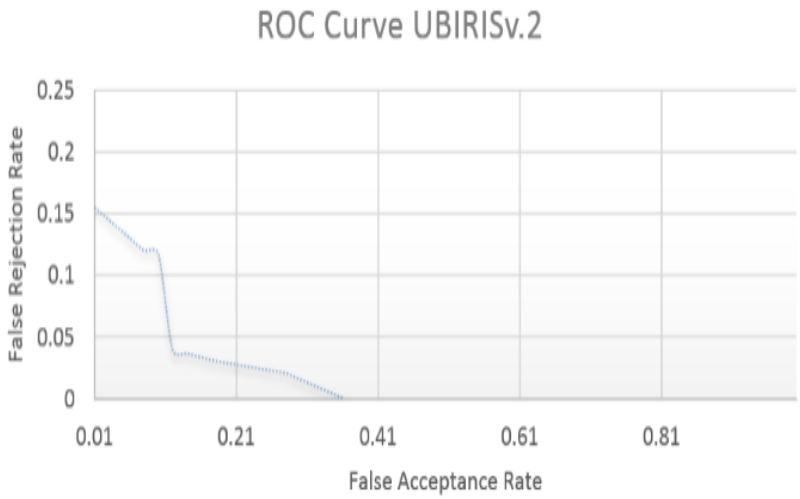

Figure 73 FRR and FAR for UBIRISv.2 Database

As the experiments were conducted on both versions of the UBIRIS database, and both databases contain noisy images with heterogeneous characteristics, the robustness of the proposed algorithms was unclear against each particular noise. Therefore, we have manually selected 520 images from UBIRISv.1 and UBIRISv.2 databases and classified them as seen in Table 14.

The proposed recognition system showed promising results against high reflection, glasses, minor occlusion and rotation noise, while the recognition accuracy significantly decreases when major occlusion, gaze deviation and dark environment noise affect the input image.

Table 14 Recognition Accuracy on Manually Selected Images

Number of Images	*Sample*	*Noise*	*Recognition Rate*
100		High reflection	97%
100		Glasses	92%
100		Minor occlusion	99%
50		Major occlusion	72%
50	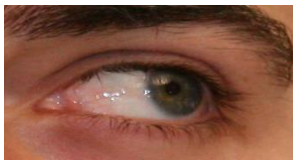	Gaze deviation	74%
20		Rotation	100%
100		Dark images	54%

5.9 Conclusion

This chapter describes the use of the Curvelet transform to extract 2D anisotropic oriented features from degraded iris templates rather than using classical methods based on textural analysis wavelet transform. Moreover, a discriminating feature selection method for increasing the robustness of the recognition system based on local highest coefficients is introduced.

The proposed use of the Curvelet transform and the discriminating features selection process can be generalized to other pattern recognition systems like face recognition and road signs recognition. Moreover it can performs better when applied to a pattern rich with edges and curves features like finger print recognition, palm recognition, hand writing recognition, plant recognition, gestures recognition and seismic signals recognition.

Chapter 6. Conclusion and Future Work

6.1 Conclusion

In this work, we addressed the challenge of improving the performance of iris recognition systems in terms of the verification and identification rates known as FAR and FRR respectively. This effort presents a novel unconstrained iris segmentation method that adapts to the quality of the captured image. The proposed algorithm searches the HSV colour space for local maxima pixels that belong to the sclera area to reduce the influence of other eye parts. After sclera detection, a quality assessment step is applied before the segmentation process takes place to judge the image quality on the basis of global features extracted from the RGB colour space and then apply suitable Retinex filter via hard light or overlay methods on the basis of the image quality. This step enhances the low quality images, removes undesirable high reflection spots from shiny images but does not harm high quality images. According to RGB features extracted, the algorithm applies an adaptive threshold value to binarize the iris image and to detect the circular outer iris boundary. After detecting the outer ring, the cropped image is converted into HSV space to search for local minima pixels that belong to the pupil area. The proposed quality assessment process cannot be generalized to other pattern recognition systems due to its dependency on the iris RGB colours.

After the segmentation process, the doughnut shape iris image is normalised into a rectangular polar coordinate image. For the normalisation of the iris image, we used the rubber sheet model algorithm introduced by Daugman followed by Laplacian sharpening

filter. Daugman's normalization process is unsuitable for non-circular iris rings caused by gaze deviation, in which some of the iris parts near the outer ring will be lost, which will affect the extracted features that will be used for further processing. Further work on iris normalization is left as future work.

This thesis also describes the use of the Curvelet transform to extract 2D anisotropic oriented features from degraded iris templates rather than using classical methods based on textural analysis wavelet transform. Moreover, a discriminating feature selection method for increasing the robustness of the recognition system based on local highest coefficients is introduced.

The proposed use of the Curvelet transform and the discriminating features selection process can be generalized to other pattern recognition systems like face recognition and road signs recognition. Moreover it can performs better when applied to a pattern rich with edges and curves features like finger print recognition, palm recognition, hand writing recognition, plant recognition, gestures recognition and seismic signals recognition.

The performance of the segmentation algorithm is evaluated on a homogeneous database (UPOL) and two heterogeneous databases (UBIRISv.1 and UBIRISv.2) with varying characteristics. The segmentation accuracy was 99.74% for the UPOL database, 99.52% for UBIRISv.1 session 1 and 99.15% for session 2, and the segmentation error rate was 1.59% for UBIRISv.2. Compared with existing algorithms, the proposed algorithm increases the segmentation accuracy over the selected databases.

Moreover, the use of the Curvelet transform for feature extraction and the selection of discriminating features reduces the FRR and FAR over UBIRISv1 and UBIRISv.2 when compared to the state-of-the art.

The recognition system was tested on the whole UBIRISv.1 database (1877 images), and the result was FRR = 5.82% at FAR = 0%, and 1000 images randomly selected images from UBIRISv.2 and the result was FRR = 29.36 % at FAR = 1%.

6.2 Limitations

The proposed iris recognition system performs well when compared to the state-of-art systems and addresses some of previous systems drawbacks, but still the system produces high FRR in certain conditions such as major occlusions, gaze deviations and dark imaging environment (Table 14 Chapter 5). Therefore, further work on the extraction and selection of discriminating features could improve the recognition accuracy.

The proposed system was tested on two heterogeneous databases UBIRISv.1 and UBIRISv.2. Other iris databases with different heterogeneous characteristics like FRGC database [107] could be tested.

6.3 Future Work

In this work, the proposed iris recognition algorithms from the segmentation to feature matching step perform well and this can be seen from the obtained results. However, there are some issues that could be addressed in the future.

The following is a list of directions for future work.

1. The normalization process used in this work is the rubber sheet model proposed by Daugman. In this process the doughnut-shaped iris image is transformed from the Cartesian coordinate system to rectangular image polar coordinate system via wrapping. The wrapping process takes a predefined number of circles with increasing radius along the iris region to form the rectangular image. In some cases, where the iris is occluded, or where the iris gaze is sharply deviated to west or east directions, the segmented shape of the iris image will be far away from a circle (Figure 74). This will produce many indefinite values for the matching process, which affects the recognition accuracy.

Figure 74 Segmented Iris

2. In unconstrained environments and especially for dark coloured irises, it is very difficult to detect the eyelashes. To the best of author's knowledge there are no methods that are able to detect and exclude the eyelashes from the segmented iris portion in degraded images. Thus, a new method for detecting and segmenting eyelashes needs to be developed.
3. The FRR increases dramatically when recognizing human irises with a sharp gaze deviation. If the left or right iris portion is occluded, a method for selecting features from the east half or west half of the iris should be studied and developed. On the

other hand, the major occlusion from upper and lower eyelids strongly affects the recognition rate. Therefore, a new method for feature selection and matching should be developed.

References

[1] UK. brp-information-leaflet. Available: [Online] https://www.gov.uk/government/uploads/system/uploads/attachment_data/file/261497/brp-information-leaflet.pdf. Last Accessed (July 2014).

[2] S. Hosseini and S. Mohammad, "Review Banking on Biometric in the World's Banks and Introducing a Biometric Model for Iran's Banking System," *Basic and Applied Scientific Research*, vol. 2, pp. 9152-9160, 2012.

[3] Biometric. Available: [Online] http://findbiometrics.com/international-biometric-group-ibg-announces-november-13-webcast-and-release-of-the-biometric-market-and-industry-report-2009-2014. Last Accessed (July 2014).

[4] K. Bowyer, "What Surprises Do Identical Twins Have for Identity Science?," *Computer Vision and Image Understanding*, vol. 44, pp. 100-102, 2011.

[5] NationalGeographicMagazine. Available: [Online] http://ngm.nationalgeographic.com/2002/04/afghan-girl/index-text. Last Accessed (July 2014).

[6] R. P. Wildes, "Iris recognition: an emerging biometric technology," *Proceedings of the IEEE*, vol. 85, pp. 1348-1363, 1997.

[7] J. Daugman, "How Iris Recognition Works," *IEEE Transactions on Circuits and Systems for Video Technology*, vol. 14, pp. 21-30, 2004.

[8] F. Bashir, P. Casaverde, D. Usher, and M. Friedman, "Eagle-Eyes: A System for Iris Recognition at a Distance," *IEEE Conference on Technologies for Homeland Security*, 2008, pp. 426-431.

[9] D. Zhang, A. Jain, D. Jeong, H.-A. Park, K. Park, and J. Kim, "Iris Recognition in Mobile Phone Based on Adaptive Gabor Filter," *Advances in Biometrics*. vol. 3832, ed: Springer Berlin / Heidelberg, 2005, pp. 457-463.

[10] H. Proença, "On the feasibility of the visible wavelength, at-a-distance and on-the-move iris recognition," in *IEEE Workshop on Computational Intelligence in Biometrics: Theory, Algorithms, and Applications, CIB.*, 2009, pp. 9-15.

[11] J. G. Daugman, "High confidence visual recognition of persons by a test of statistical independence," *Transactions on Pattern Analysis and Machine Intelligence, IEEE,* vol. 15, pp. 1148-1161, 1993.

[12] K. W. Bowyer, K. Hollingsworth, and P. J. Flynn, "Image understanding for iris biometrics: A survey," *Comput. Vis. Image Underst.*, vol. 110, pp. 281-307, 2008.

[13] J. R. Matey, O. Naroditsky, K. Hanna, R. Kolczynski, D. J. LoIacono, S. Mangru, *et al.*, "Iris on the Move: Acquisition of Images for Iris Recognition in Less Constrained Environments," *Proceedings of the IEEE,* vol. 94, pp. 1936-1947, 2006.

[14] H. Proença and L. A. Alexandre, "Toward noncooperative iris recognition: a classification approach using multiple signatures," *Transactions on Pattern Analysis and Machine Intelligence,* vol. 29, pp. 607-12, Apr 2007.

[15] R. Ng, Y. Tay, and K. Mok, "A review of iris recognition algorithms," in *International Symposium on Information Technology. ITSim*, 2008, pp. 1-7.

[16] S. Weicheng and R. Khanna, "Prolog To Iris Recognition: An Emerging Biometric Technology," *Proceedings of the IEEE,* vol. 85, pp. 1347-1347, 1997.

[17] M. Li, W. Yunhong, and T. Tieniu, "Iris recognition using circular symmetric filters," in *Proceedings of 16th International Conference on Pattern Recognition.* , 2002, pp. 414-417 vol.2.

[18] N. Ritter, R. Owens, J. Cooper, and P. P. van Saarloos, "Location of the pupil-iris border in slit-lamp images of the cornea," in *Proceedings of International Conference on Image Analysis and Processing,*, 1999, pp. 740-745.

[19] S. Hanho, L. Jaekyung, P. Ji-hyun, and L. Yillbyung, "Iris recognition using collarette boundary localization," in *Proceedings of the 17th International Conference on Pattern Recognition. ICPR.* , 2004, pp. 857-860 Vol.4.

[20] K. Grabowski, W. Sankowski, M. Zubert, and M. Napieralska, "Reliable Iris Localization Method With Application To Iris Recognition In Near Infrared Light," in *Proceedings of the International Conference on Mixed Design of Integrated Circuits and System, MIXDES.* , 2006, pp. 684-687.

[21] J. Daugman, "New methods in iris recognition," *IEEE Transactions on System Man and Cybernetics Part B,* vol. 37, pp. 1167-75, Oct 2007.

[22] L. Masek, "Iris Recognition," BE, Computer Science and Software Engineer Western Australia, 2003.

[23] J. Cui, Y. Wang, T. Tan, L. Ma, and Z. Sun, "A Fast and Robust Iris Localization Method Based on Texture Segmentation," *SPIE Defense and Security Symposium,* vol. 5404, pp, pp. 401-408, 2004.

[24] W. K. Kong and D. Zhang, "Accurate iris segmentation based on novel reflection and eyelash detection model," in *Proceedings of International Symposium on Intelligent Multimedia, Video and Speech Processing.*, 2001, pp. 263-266.

[25] H. Junzhou, W. Yunhong, T. Tieniu, and C. Jiali, "A new iris segmentation method for recognition," in *Proceedings of the 17th International Conference on Pattern Recognition, ICPR.* , 2004, pp. 554-557 Vol.3.

[26] M. Li, T. Tieniu, W. Yunhong, and Z. Dexin, "Efficient iris recognition by characterizing key local variations," *IEEE Transactions on Image Processing.,* vol. 13, pp. 739-750, 2004.

[27] H. Proença and L. A. Alexandre, "A Method for the Identification of Noisy Regions in Normalized Iris Images," in *18th International Conference on Pattern Recognition, ICPR.,* 2006, pp. 405-408.

[28] A. V. Oppenheim and J. S. Lim, "The importance of phase in signals," *Proceedings of the IEEE,* vol. 69, pp. 529-541, 1981.

[29] H. E. Kocer and N. Allahverdi, "An efficient iris recognition system based on modular neural networks," *ETRI Journal,* vol. 23, 2008.

[30] A. Poursaberi and B. N. Araabi, "Iris Recognition for Partially Occluded Images: Methodology and Sensitivity Analysis," *EURASIP Journal on Advances in Signal Processing,* vol. 4, 2007.

[31] Christel, L. Tisse, L. Martin, L. Torres, and M. Robert, "Person Identification Technique Using Human Iris Recognition," in *Proceeding of Vision Interface,* 2002, pp. 294-299.

[32] D. M. Monro, S. Rakshit, and Z. Dexin, "DCT-Based Iris Recognition," *Pattern Analysis and Machine Intelligence, IEEE Transactions on,* vol. 29, pp. 586-595, 2007.

[33] R. Ng, Y. Tay, and K. Mok, "A review of iris recognition algorithms," in *International Symposium on Information Technology*, 2008, pp. 1-7.

[34] S. Lim, K. Lee, O. Byeon, and T. Kim, "Efficient iris recognition through improvement of feature vector and classifier," *ETRI,* vol. 23, 2001.

[35] W. Boles and B. Boashash, "A human identification technique using images of the iris and wavelet transform," *IEEE Transactions on Signal Processing,* vol. 46, pp. 1185-1188, 1998.

[36] S. Noh, K. Pae, C. Lee, and J. Kim, "Multiresolution independent component analysis for iris identification," in *Proceedings of The International Technical Conference on Circuits/Systems, Computers and Communications*, Phuket, Thailand, 2002.

[37] Z. Zhi, D. Yingzi, and C. Belcher, "Transforming Traditional Iris Recognition Systems to Work in Nonideal Situations," *IEEE Transactions on Industrial Electronics,* vol. 56, pp. 3203-3213, 2009.

[38] M. Vatsa, R. Singh, and A. Noore, "Improving Iris Recognition Performance Using Segmentation, Quality Enhancement, Match Score Fusion, and Indexing," *IEEE Transactions on Systems, Man, and Cybernetics, Part B,* vol. 38, pp. 1021-1035, 2008.

[39] L. Xining, "Image Enhancemnt Filter Using Retinex," in *Proceedings of the International Conference on Computer Image Processing*, Italy, 2008.

[40] BIT. CASIA Iris Image Database [Online]. Available: http://biometrics.idealtest.org/. Last Accessed (July 2014).

[41] Smart-Sensor-Ltd. BATH Iris Database [Online]. Available: http://www.smartsensors.co.uk/products/iris-database/. Last Accessed (July 2014).

[42] SmartSensores. Available: [Online] http://www.smartsensors.co.uk/products/iris-database/. Last Accessed (July 2014).

[43] Multimedia-University. MMU Database [Online]. Available: http://pesona.mmu.edu.my/~ccteo/. Last Accessed (July 2014).

[44] National-Institute-of-Standard-and-Technology. Iris Challenge Evaluation Database [Online]. Available: http://www.nist.gov/itl/iad/ig/ice.cfm. Last Accessed (July 2014).

[45] West-Virginia-University. WVU Iris Database [Online]. Available: http://www.csee.wvu.edu/~xinl/demo/nonideal_iris.html. Last Accessed (July 2014).

[46] University-of-Palackeho-and-Olomouc. UPOL Iris Database [Online]. Available: http://phoenix.inf.upol.cz/iris/. Last Accessed (July 2014).

[47] H. Proença and L. Alex, "UBIRIS: A noisy iris image database," in *Proceedings of the 13th International Conference on Image Analysis and Processing* - ICIAP, 2005.

[48] H. Proença, S. Filipe, R. Santos, J. Oliveira, and L. A. Alexandre, "The UBIRIS.v2: a database of visible wavelength iris images captured on-the-move and at-a-distance," *IEEE Transaction Pattern Analysis and Machine Intelligence,* vol. 32, pp. 1529-35, Aug 2010.

[49] J. Daugman, "The importance of being random: statistical principles of iris recognition," *Pattern Recognition Society,* pp. 279-291, 2002

[50] D. De Martin-Roche, C. Sanchez-Avila, and R. Sanchez-Reillo, "Iris recognition for biometric identification using dyadic wavelet transform zero-crossing," *in Proceedings of the International Carnahan Conference on Security Technology,* IEEE 35th 2001.

[51] J. Daugman. Available: [Online] https://www.cl.cam.ac.uk/~jgd1000. Last Accessed (July 2014).

[52] D.-S. Huang, D. C. Wunsch, D. S. Levine, and K.-H. Jo, "*Advanced Intelligent Computing Theories and Applications. With Aspects of Artificial Intelligence" Fourth International Conference on Intelligent Computing*: Springer Publishing Company, Incorporated, 2008.

[53] I. Guyon, J. Makhoul, R. Schwartz, and V. Vapnik, "What size test set gives good error rate estimates?," *IEEE Transactions on Pattern Analysis and Machine Intelligence,* vol. 20, pp. 52-64, 1998.

[54] H. Yuqing, C. Jiali, T. Tieniu, and W. Yangsheng, "Key Techniques and Methods for Imaging Iris in Focus," in *Proceeding of 18th International Conference on Pattern Recognition ICPR* 2006, pp. 557-561.

[55] K. Grabowski, W. Sankowski, M. Zubert, and M. Napieralska, "Illumination influence on iris identification algorithms," in *15th International Conference on Mixed Design of Integrated Circuits and Systems. MIXDES.* , 2008, pp. 571-574.

[56] T. A. Camus and R. Wildes, "Reliable and fast eye finding in close-up images," in *16th International Conference on Pattern Recognition.* , 2002, pp. 389-394 vol.1.

[57] H. Proença, "Iris recognition: on the segmentation of degraded images acquired in the visible wavelength," *IEEE Transactions on Pattern Analysis and Machine Intelligence,* vol. 32, pp. 1502-16, Aug 2010.

[58] H. Proença and L. A. Alexandre, "Iris segmentation methodology for non-cooperative recognition," *IEEE Proceedings - Vision, Image, and Signal Processing,* vol. 153, p. 199, 2006.

[59] M. Tuceryan, "Moment based texture segmentation," in *Proceedings of 11th IAPR International Conference on Pattern Recognition, Conference C: Image, Speech and Signal Analysis,*, 1992, pp. 45-48.

[60] R. Chen, X. R. Lin, and T. H. Ding, "Iris segmentation for non-cooperative recognition systems," *IET Image Processing,* vol. 5, p. 448, 2011.

[61] C. W. Tan and A. Kumar, "Unified framework for automated iris segmentation using distantly acquired face images," *IEEE Transaction on Image Processing,* vol. 21, pp. 4068-79, Sep 2012.

[62] A. Radman, N. Zainal, and K. Jumari, "Fast and reliable iris segmentation algorithm," *IET Image Processing,* vol. 7, pp. 42-49, 2013.

[63] H. Proença and L. A. Alexandre, "Toward Covert Iris Biometric Recognition: Experimental Results From the NICE Contests," *IEEE Transactions on Information Forensics and Security*, vol. 7, pp. 798-808, 2012.

[64] C. W. Tan and A. Kumar, "Towards online iris and periocular recognition under relaxed imaging constraints," *IEEE Transaction on Image Processing*, vol. 22, pp. 3751-65, Oct 2013.

[65] "American National Standard for the safe use of lasers and LEDs used in optical fiber transmission systems," 1988.

[66] "Photobiological safety standards for safety standards for lamps," 1999.

[67] E. Krichen, M. A. Mellakh, S. Garcia-Salicetti, and B. Dorizzi, "Iris identification using wavelet packets," in *Proceedings of the 17th International Conference on Pattern Recognition ICPR*, 2004, pp. 335-338.

[68] T. Tan, X. Zhang, Z. Sun, and H. Zhang, "Noisy iris image matching by using multiple cues," *Pattern Recognition Letters*, vol. 33, pp. 970-977, 2012.

[69] D. M. Monro, S. Rakshit, and D. Zhang, "DCT-based iris recognition," *IEEE Transactions on Pattern Analysis and Machine Intelligence.*, vol. 29, pp. 586-95, Apr 2007.

[70] A. D. Rahulkar and R. S. Holambe, "Half-Iris Feature Extraction and Recognition Using a New Class of Biorthogonal Triplet Half-Band Filter Bank and Flexible k-out-of-n:A Postclassifier," *IEEE Transactions on Information Forensics and Security*, vol. 7, pp. 230-240, 2012.

[71] M. S. Hosseini, B. N. Araabi, and H. Soltanian-Zadeh, "Pigment Melanin: Pattern for Iris Recognition," *IEEE Transactions on Instrumentation and Measurement,* vol. 59, pp. 792-804, 2010.

[72] H. Proença and G. Santos, "Fusing color and shape descriptors in the recognition of degraded iris images acquired at visible wavelengths," *Computer Vision and Image Understanding,* vol. 116, pp. 167-178, 2012.

[73] A. F. Mat Raffei, H. Asmuni, R. Hassan, and R. M. Othman, "Feature extraction for different distances of visible reflection iris using multiscale sparse representation of local Radon transform," *Pattern Recognition,* vol. 46, pp. 2622-2633, 2013.

[74] A. Ahamed and M. Bhuiyan, "Low complexity iris recognition using curvelet transform," in *Proceedings of the International Conference on Informatics, Electronics & Vision* (ICIEV), 2012.

[75] N. Mojtaba and G. Sedigheh, "Iris Recognition Based on Using Ridgelet and Curvelet Transform," *International Journal of Signal Processing, Vol. 4 Issue 2, p7,* 2011.

[76] G. Yazhuo, D. Zhang, S. Pengfei, and Y. Jingqi, "An Optimized Wavelength Band Selection for Heavily Pigmented Iris Recognition," *IEEE Transactions on Information Forensics and Security,* vol. 8, pp. 64-75, 2013.

[77] G. Santos and H. Proença, "Iris recognition: Analyzing the distribution of the iriscodes concordant bits," in *Proceeding of 3rd International Conference on Image and Signal Processing (CISP),* 2010, pp. 1873-1877.

[78] Z. He, T. Tan, Z. Sun, and X. Qiu, "Toward accurate and fast iris segmentation for iris biometrics," *IEEE Transactions on Pattern Analysis and Machine Intelligence,* vol. 31, pp. 1670-84, Sep 2009.

[79] Y. Du, E. Arslanturk, Z. Zhou, and C. Belcher, "Video-based noncooperative iris image segmentation," *IEEE Transaction on System Man and Cybernetics Part B,* vol. 41, pp. 64-74, Feb 2011.

[80] Z. Sun and T. Tan, "Ordinal measures for iris recognition," *IEEE Transaction on Pattern Analysis and Machine Intelligence,* vol. 31, pp. 2211-26, Dec 2009.

[81] M. Islam, Z. Dengsheng, and L. Guojun, "Rotation invariant curvelet features for texture image retrieval," in *Proceeding of IEEE International Conference on Multimedia and Expo, ICME.* , 2009, pp. 562-565.

[82] J. Ma and G. Plonka, "The Curvelet Transform," *IEEE Signal Processing Magazine,* vol. 27, pp. 118-133, 2010.

[83] W. T. Freeman and E. H. Adelson, "The design and use of steerable filters," *IEEE Transactions on Pattern Analysis and Machine Intelligence,* vol. 13, pp. 891-906, 1991.

[84] L. Tai Sing, "Image representation using 2D Gabor wavelets," *IEEE Transactions on Pattern Analysis and Machine Intelligence,* vol. 18, pp. 959-971, 1996.

[85] N. Do and M. Vetterli, "The contourlet transform: an efficient directional multiresolution image representation," *IEEE Transaction on Image Processing,* vol. 14, pp. 2091-106, Dec 2005.

[86] G. R. Easley, D. Labate, and Q. L. Wang, "Optimally Sparse Image Representations using Shearlets," in *Proceeding of 40th Asilomar Conference on Signals, Systems and Computers ACSSC*, 2006, pp. 974-978.

[87] E. P. Simoncelli, W. T. Freeman, E. H. Adelson, and D. J. Heeger, "Shiftable multiscale transforms," *IEEE Transactions on Information Theory*, vol. 38, pp. 587-607, 1992.

[88] M. Meselhy Eltoukhy, I. Faye, and B. Belhaouari Samir, "A comparison of wavelet and curvelet for breast cancer diagnosis in digital mammogram," *Computers in Biology and Medicine*, vol. 40, pp. 384-391, 2010.

[89] D. M. Monro and S. Rakshit, "Rotation Compensated Human Iris Matching," in *Proceeding of IEEE Workshop on Signal Processing Applications for Public Security and Forensics. SAFE '07* , 2007, pp. 1-4.

[90] D. M. Monro and S. Rakshit, "Rotation-Independent IRIS Matching by Motion Estimation," in *Proceeding of IEEE International Conference on Image Processing,*, 2007, pp. 401 - 404.

[91] H. Takano and K. Nakamura, "Rotation independent iris recognition by the rotation spreading neural network," in *Proceeding of IEEE 13th International Symposium on Consumer Electronics. ISCE '09*, 2009, pp. 651-654.

[92] S. Matschitsch, H. Stögner, and M. Tschinder, "Rotation-Invariant Iris Recognition Boosting 1D Spatial-Domain Signatures to 2D," in *Proceedings of the 5th International Conference on Informatics in Control, Automation and*

Robotics, Department of Computer Sciences, University of Salzburg, Austria, 2008.

[93] D. R. S. Kumar, K. B. Raja, N. Nuthan, B. Sindhuja, P. Supriya, R. K. Chhotaray, *et al.*, "Iris Recognition Based on DWT and PCA," *in Proceedings of the International Conference on Computational Intelligence and Communication Networks* (CICN), 2011.

[94] C. Wen-Shiung, C. Chi-An, S. Sheng-Wen, and C. Shun-Hsun, "Iris recognition using 2D-LDA + 2D-PCA," *in Proceedings of the IEEE International Conference on Acoustics, Speech and Signal Processing*, ICASSP. 2009.

[95] A. M. Martinez and A. C. Kak, "PCA versus LDA," *IEEE Transactions on Pattern Analysis and Machine Intelligence*, vol. 23, pp. 228-233, 2001.

[96] CandesCurvelets. Available: [Online] www.cs.tut.fi/~karen/CandesCurvelets.pdf. Last Accessed (July 2014).

[97] S. Venugopalan and M. Savvides, "How to Generate Spoofed Irises From an Iris Code Template," *IEEE Transactions on Information Forensics and Security*, vol. 6, pp. 385-395, 2011.

[98] Z. Yong, T. Tieniu, and W. Yunhong, "Biometric personal identification based on iris patterns," in *Proceedings of 15th International Conference on Pattern Recognition*, 2000, pp. 801-804 vol.2.

[99] M. Li, W. Yunhong, and T. Tieniu, "Iris recognition using circular symmetric filters," in *Proceedings of 16th International Conference on Pattern Recognition*,, 2002, pp. 414-417 vol.2.

[100] R. M. Farouk, R. Kumar, and K. A. Riad, "Iris matching using multi-dimensional artificial neural network," *IET Computer Vision,* vol. 5, p. 178, 2011.

[101] M. Vatsa, R. Singh, and A. Noore, "Improving iris recognition performance using segmentation, quality enhancement, match score fusion, and indexing," *IEEE Transaction on System Man and Cybernetics Part B,* vol. 38, pp. 1021-35, Aug 2008.

[102] Q. Wang, X. Zhang, M. Li, X. Dong, Q. Zhou, and Y. Yin, "Adaboost and multi-orientation 2D Gabor-based noisy iris recognition," *Pattern Recogn Letter,* vol. 33, pp. 978-983, 2012.

[103] H. Proença and L. A. Alexandre, "The NICE.I: Noisy Iris Challenge Evaluation - Part I," in *First IEEE International Conference on Biometrics: Theory, Applications, and Systems, BTAS.*, 2007, pp. 1-4.

[104] E. Candes and D. Donoho, "Curvelets: A Surprisingly Effective Nonadaptive Representation of Objects with Edges," in *IN CURVE AND SURFACE FITTING: SAINT-MALO*, ed: University Press, 2000.

[105] E. Candès, L. Demanet, D. Donoho, and L. Ying, "Fast Discrete Curvelet Transforms," *SIAM Multiscale Model Simulation,* vol. 5, pp. 861-899, 2006.

[106] S. P. Fenker, E. Ortiz, and K. W. Bowyer, "Template Aging Phenomenon in Iris Recognition," *IEEE Access,* vol. 1, pp. 266-274, 2013.

[107] Face Recognition Grand Challenge Database [Online]. Available: http://www.nist.gov/itl/iad/ig/frgc.cfm. Last Accessed (July 2014).

[108] L. Flom, and A. Safir, "Iris recognition system". U.S. Patent 4641394, 1987

[109] D. Mumford, J. Shah, ". Optimal approximations by piecewise smooth functions and associated variational problems". Communication and Pure Applied Mathematics. vol.42, pp. 577–685, 1989.

[110] SANS Institute InfoSec Reading Room. Available [Online]: http://www.sans.org/reading-room/whitepapers/authentication/iris-recognition-technology-improved-authentication-132 . Last Accessed (July 2014).

[111] Math Work. Available [Online]: http://www.mathworks.com/help/images/ref/regionprops.html. Last Accessed (December 2014)

Appendix A

Complete Iris Recognition Framework

In this effort, a new segmentation algorithm for detecting the limbus and pupillary boundaries (known as inner and outer boundaries) of human iris images is first presented. Most of the currently deployed systems benefit from costly imaging instruments when capturing rich in texture near infrared iris images with look and stare at a close distance constrains. We designed a novel segmentation algorithm based on RGB and HSV colour spaces to successfully detect the inner and outer rings as well as upper and lower eyelids of the human iris that have been acquired at a four to eight metre distance, on the move and using a visible wavelength light source. Secondly, utilization of Curvelet transform and new discriminating feature selection method were introduced for extracting enough features from degraded iris templates to increase the robustness of the recognition system rather than the classical methods based on textural analysis wavelet transform (Figure 75), which states every phase in the recognition system. A heterogeneous iris image database which contains non-ideal images affected with fourteen different noise factors (off-angle, poor focus, rotated, motion blurred, at a distance, on the move, occluded with eyelids, eyelashes, glasses, contact lens, hair, high reflection and out of iris). This dataset is available free of charge on the internet at [47] [48] called UBIRIS.v1 and UBIRIS.v2 databases.

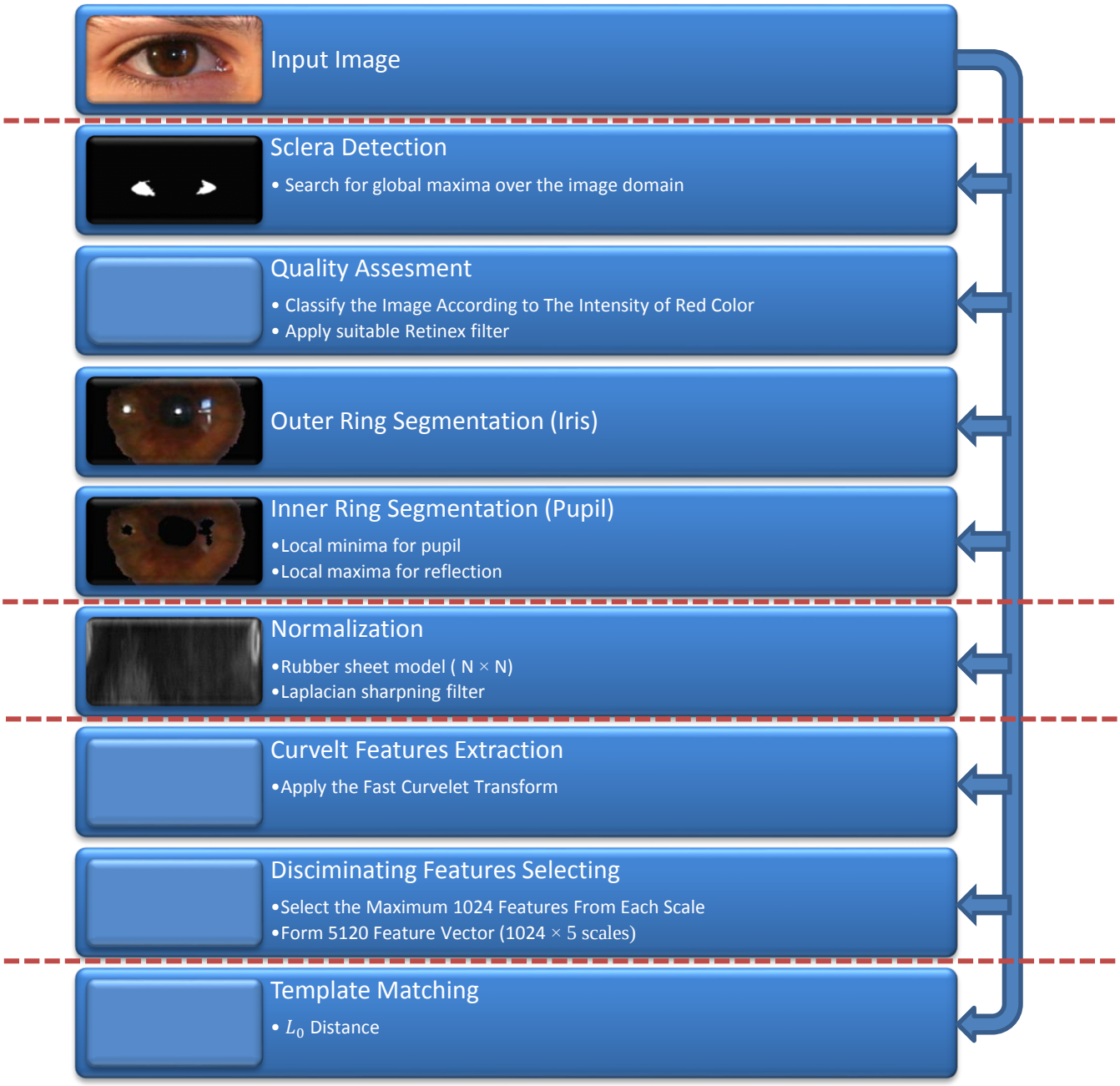

Figure 75 Complete Unconstrained Iris Recognition System

Objectives

- Light problem: most of the current iris recognition systems use NIR (Near Infrared) light sources in the iris image acquisition. This research aims to use iris images captured under natural or traditional light sources.
- Distance and Occlusion: Most of the current systems deal with high resolution iris images that have been captured through high resolution cameras and from close distances to capture enough textural features from the human iris. This research aims to capture discriminating features from degraded images.
- Rotation: an original rotation invariant technique that suits the proposed feature extraction algorithm (Curvelet transform).

Iris Images

The proposed framework was tested on three visible wavelength databases; the first one was UPOL database that contains high resolution images; The second was the UBIRISv.1 database which contains noisy images captured under different light sources with high reflection and different occlusion ratio but at close distance without subject moving; the third database that best meets the requirements of the proposed algorithms is UBIRS-v2.

Segmentation

The whole segmentation process is subdivided into three processes, namely:

1. The first one is detection of sclera as it is the most easily distinguishable part of the human eye. To get rid of other eye parts like eyebrows and the skin of upper and lower eyelids, the output parameters will be the points (x_1, y_1), (x_2, y_2) and (x_3, y_3), (x_4, y_4) that represent the far left and the far right corners of the

human eye, as well as the upper and lower extremes of the eye region. From these point coordinates, the human iris should be normalized to a fixed size. Moreover, the influence of iris rotation can be reduced by altering the values of y_1 and y_2 points until $y_1 = y_2$.

2. The second part of the method is further subdivided into two steps; the first step is the quality assessment that classifies the input image according to image quality and applies a suitable filter, while the second step converts the RGB image to a binary image for outer ring segmentation.

3. In the last part of the method, the enhanced segmented image that results from the second part is converted into HSV to detect and segment the pupil area. The next three sections will explain each part of the method, and the last section will be dedicated to the experimental results.

The first step is to detect the sclera parts, as it is the most easily distinguishable part of the human eye.

Sclera Detection

The first step in the segmentation process is to detect the sclera as it is the most easily distinguishable part of the human eye. To get rid of other eye parts like eyebrows and the skin of the upper and lower eyelids, the output parameters will be the points(x_1, y_1), (x_2, y_2) and (x_3, y_3), (x_4, y_4) that represent the far left and the far right corners of the human eye, as well as upper and lower extremes of the eye region. From these point coordinates, the human iris could be normalized to a fixed size. Moreover, the influence of iris rotation can be reduced by altering the values of y_1 and y_2 points until $y_1 = y_2$.

Here, the image is converted to HSV colour space, as it is more robust against reflection than the RGB. Then the method searches for local maxima to define the area of high intensity colour representing the white coloured pixels of the input RGB images as follows:

$$HSVmask_{(x,y)} = 1\ if(\ H > h_{th}\ and\ S < S_{th}\ and\ V > V_{th}), 0\ otherwise$$

where, HSV_{mask} is the mask image that contains the pixels with, H Hue, S Saturation and V Values that define the area of high intensity colour values.

The results of the previous step is a binary non smooth image as seen in Figure 76 (e). Therefore, we applied an erosion and dilation process to the resultant image as seen in Figure 76 (f).

Now we just have the sclera area of the whole eye image. The main reason for this process is to minimize the search area for iris segmentation, and to normalize the iris area to a fixed size and finally to find the angle of rotation. A search process to find the first five black pixels with intervals of 10 pixels have been made for the left and right sides of the sclera, and for the upper and the lower sides separately, as seen in Figure 77.

Using simple linear polynomial fitting, a tangent line that crosses the upper and lower detected pixels from both sides is drawn. The rectangular area that crosses the intersection points for all tangents well represents the area of interest (Figure 77) where

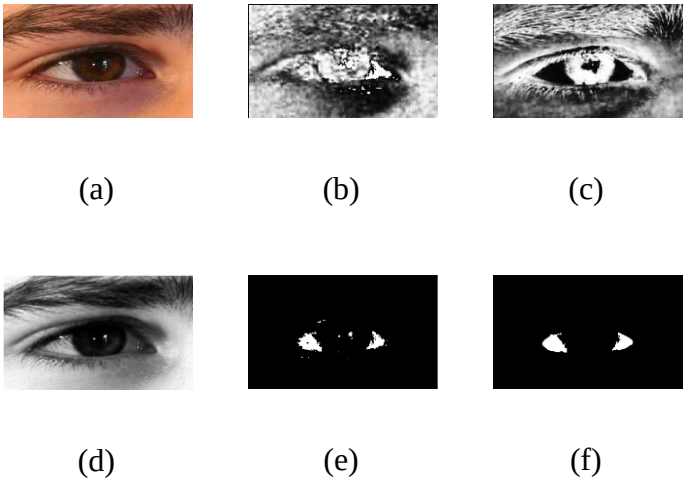

Figure 76: (a) original image, (b) Hue, (c) Saturation, (d) Value, (e) Masked image and (f) Filtered image.

A, B, C and D represent the points $(x_1, y_1), (x_2, y_2), (x_3, y_3), (x_4, y_4)$ respectively. Now, to minimize the influence of rotation, simply the system rotate the resulting image until $y_1 = y_2$, and , finally, reconstruct the RGB version by multiplying the resultant binary image with the original input image and crop a bounding box with width = $x_1 - x_2$, and height = $y_1 - y_2$.

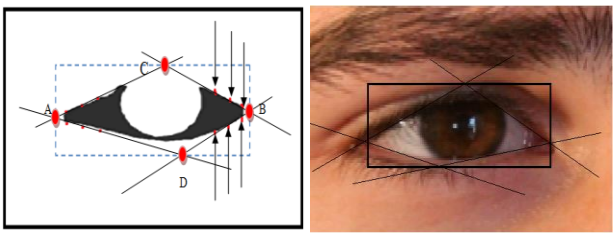

Figure 77: A, B, C and D represent the points $(x_1, y_1), (x_2, y_2), (x_3, y_3), (x_4, y_4)$ respectively.

Iris Segmentation (Outer)

Through many experiments on a huge numbers of iris images, it was obvious: in the RGB image, the Green and Blue colours are relatively stable in comparison with the Red colour.

That means if the lighting condition was changed at the time of capturing the same image, the sum of Green and Blue values (intensity) will vary in amount of ≈ 5 to 15%, while the sum of the Red colour value will vary in amount of ≈ 10 to 35%. Therefore, we used the average of the red colour intensity to classify the input images whether they are poor, faded, blurred, low reflection or high reflection.

where n is the number of pixles in the image, val_i is the value of red color intensity taken from red value of $RGB(1:0:0)$, According to the average of the Red colour values, apply the Retinex filter with or without smoothing then binarize the image using a predefined threshold. For image classification according to the red colour average, seven different categories have been selected; the first three categories include (dark brown, dark blue and dark green iris colour, the dusky iris images and the poorly focused images), these images suffer from low brightness and contrast. Therefore, a Retinex filter (hard light) was applied.

In the fourth category, just a histogram equalization is needed because only the hazel and light brown images and clear images fall into this category, and the last three categories contain images with (light blue, light green, specular reflection, light reflection and images with glasses). Here a Retinex filter (overlay) along with Gaussian smoothing filter were applied to process the input image.

Finally, binarize (convert to black and white BW) the image

$$BW = \begin{cases} 1 \; if \; r > threshold \\ 0 \; if \; r \leq threshold \end{cases}$$

Multiply the black and white image with the input RGB image to get the segmented outer ring (Figure 80).

Iris Segmentation (Inner)

In this step, the inner part of the iris image (pupil) is segmented. As the pupil area is the darkest portion in the iris, the method searches for local minima values over the HSV colour domain. The empirical testing led to choosing the following range of values,

$$H\ (0.2 - 0.8), S\ (0 - 0.5), V\ (0 - 0.32).$$

Due to noise and especially high reflection, the detected area resulting from the HSV colour masking, will be of a non-smooth and non-circular shape. Therefore, a bank of filters are applied to the detected area to get the circular shape of the pupil using the applications of morphological operations as follows:

1. Filter size and area: This filter calculates the size of the segmented area and detects the small plops of noise in the pupil area.
2. Filter creates structure: This filter fills the detected plops with black colour.
3. Filter circle: This filter completes the shape of the pupil to a circular shape.

Finally, from the detected shape coordinates get the centre and radius and crop the pupil circle from the input images as shown in Figure 78.

After applying the outer and inner segmentation methods, the result will be a doughnut shape iris image with eyelids and eyelashes occlusion (Figure 80). The presence of eyelids and eyelashes will affect the features that will be extracted later from the segmented images. Therefore, the upper and lower eyelids should be avoided.

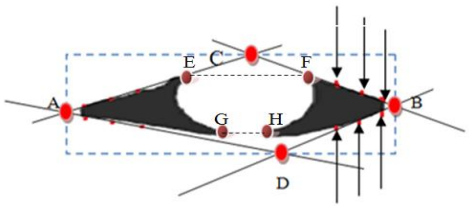

Figure 78: points coordinate E (x_5, y_5), F(x_6, y_6), G(x_7, y_7) and H(x_8, y_8).

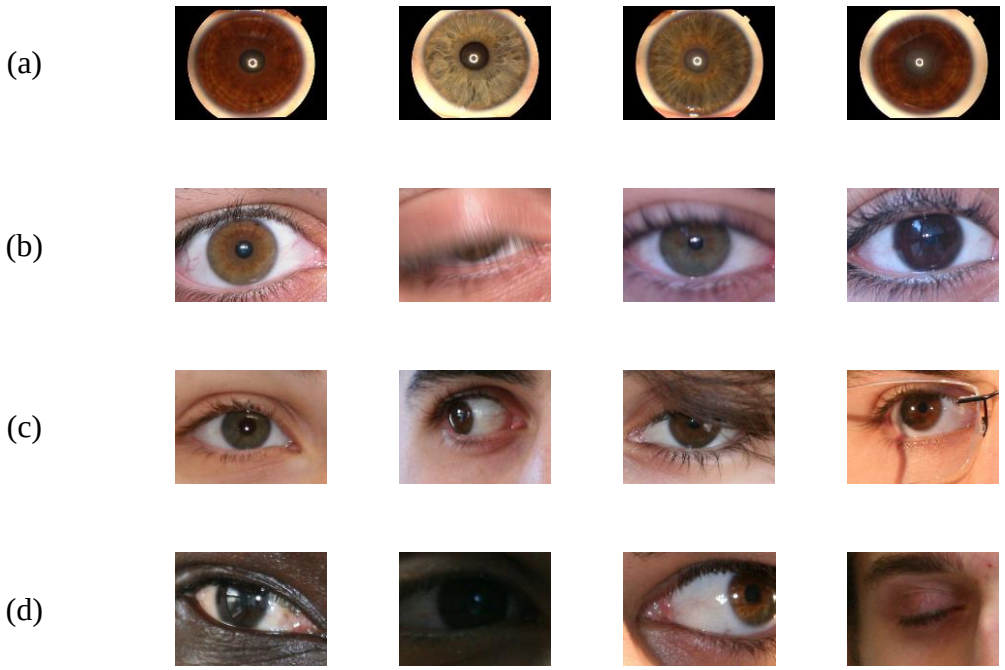

Figure 79: (a) Sample images from UPOL, (b) UBIRISv.1, (c and d) UBIRISv.2.

From the sclera detection, the close points around the upper and lower iris extremes as shown in Figure 78 the brown circles were calculated. From these points coordinate E (x_5, y_5), F(x_6, y_6), G(x_7, y_7) *and* H(x_8, y_8) we can crop the area above the upper $(y_5 + 5, y_6 + 5)$ and below the lower (y_7, y_8) coordinates to remove the upper and lower eyelids. The reason behind adding 5 pixels to the upper coordinates, is to minimize the

influence of eyelashes that might cover the sclera corners around the upper extreme. The only exception in this step is applied where the distance between x_5 and x_6 is less than 5 pixels, then no cropping process will be needed.

The proposed algorithm was tested on three datasets (UPOL, UBIRISv.1 and UBIRISv.2). The experiments were applied to the whole UPOL database (384 images), the whole UBIRISv.1 database (1877 images) and 1000 images randomly selected from UBIRISv.2 (NICE.II). Samples from all used databases are given in Figure 79.

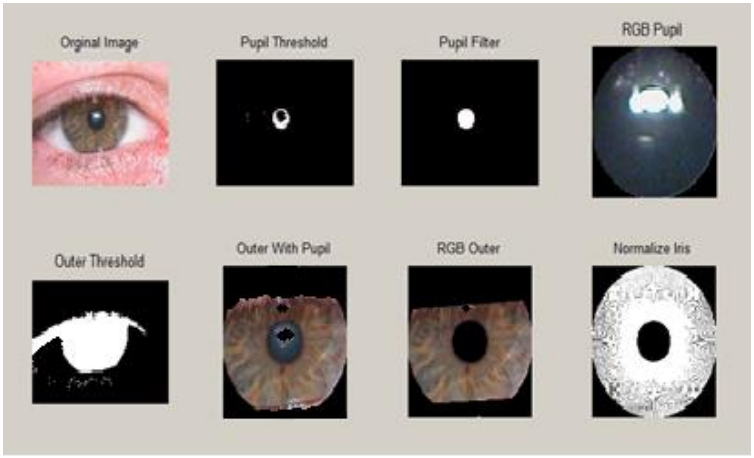

Figure 80: Output of the proposed segmentation algorithm, implemented in Matlab.

Figure 80 shows the output of the implemented algorithm in Matlab, and the accuracy of the system was 99.74% for UPOL database, 99.52%, 99.15% for UBIRIS.v1 session 1 and session 2, respectively. The previous results were calculated on the basis of visual inception, and finally the error rate for UBIRIS V2 was 1.59% calculated according to the evaluation protocol given by NICE.I [103].

Normalization

The normalization process is used to represent the segmented portion of the iris image in a form that is invariant to the size and position. In normalization, the segmented iris portion is converted into a rectangular image. This can be achieved by converting the segmented portion of the iris to dimensionless pseudo-polar coordinates through a method called Homogenous Rubber Sheet Model [11].

The homogenous rubber sheet model is given as.

$$I\left(x\left(r,\theta\right),y\left(r,\theta\right)\right)\rightarrow I\left(r,\theta\right)$$

where

$$x\left(r,\theta\right)=(1-r)x_p(\theta)+\ rx_i(\theta)$$

$$y\left(r,\theta\right)=(1-r)y_p(\theta)+\ ry_i(\theta)$$

$I(x,y)$, is the iris image region, (x,y), is the cartesian coordinates, (r,θ) is the polar coordinats corresponding to (x,y), x_p,y_p and x_i,y_i are the coordinates of the outer and inner rings along with θ direction. Homogenous rubber sheet model algorithms can overcome the iris capturing distance problem and the pupil extension but are not suitable for iris rotation.

It is just like drawing concentric circles of pixels in the iris moving out of the circle immediately around the pupil, but instead of drawing circles of pixels, the pixel should be extracted from an oval shaped iris and put in a linear shape as a rectangle. This can be done by extracting the first upper ring of pixels in the iris at the size of iris diameter at

360° and arranging these pixels in a straight line then decreasing the diameter by one and arranging the extracted pixels in the second line and so on until reaching the pupil.

If the first circle of the iris is parsed with 1° step, the width of the resultant rectangle will be 360, and the height of the rectangle will be equal to the difference in the radius size between the iris and the pupil.

Feature Extraction

As the system was built to process iris images captured over distance, without look and stares constrains and using different lighting conditions, the resulting images will have a poor quality and low textural features. In such circumstances, the textural features offered by the images are not reliable and will cause higher FRR in the recognition system. Therefore, it is preferable to rely on the geometrical features such as lines and curves singularities offered by the human iris pattern from enhanced images with Laplacian edge sharpening filter.

Through a wide research and experiments the founding was that the Curvelet transform outperforms the limited orientation selectivity in the 2D Gabor transform and other isotropic textural feature transforms [81] [88].

Curvelet Algorithm

The Curvelet transform is divided into four steps as follows:

1. 2D FFT of the image is taken (Cartesian Frequency Plane) and obtain $\hat{f}(n_1, n_2)$
2. 2D Fourier frequency plane is divided into shears (Wedges)

3. For each scale j and angle l multiply the sheared object $\hat{f}$ with the parabolic window: and form the product $\widetilde{U_{J,L}}\,[n_1, n_2]\hat{f}[n_1, n_2]$.
4. Inverse 2D FFT for each shear $\hat{f}_{j,l}$ via Wrapping to obtain Discrete Curvelet $C^{d}_{j,l,k}$

Implementation

After the segmentation process and before the normalization phase, a process to the segmented images should be applied to maximize the robustness of the Curvelet transform. The Curvelet transform is very sensitive to 2D curve discontinuities, so any interference from eyelashes will affect the extracted features vector. Therefore, the upper side of the iris should be excluded from the feature extraction process to minimize the influence of eyelashes and eyelids (Figure 81). This can be done by cropping the area above the points (E, F) and below (G, H) from the sclera detection phase.

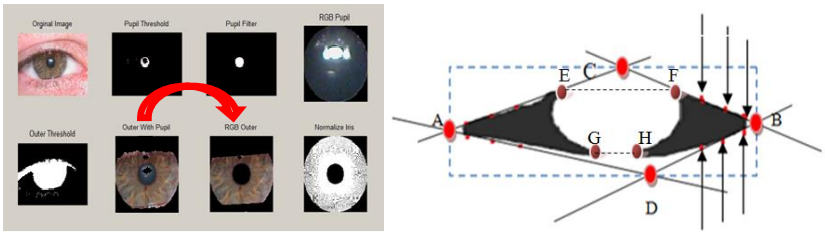

Figure 81 the Exclusion of Eyelashes

The normalized iris template is then processed by Laplacian sharpening filter and entered into the Curvelet transform, the features of interest from Curvelet transform will be the coefficients with highest values. Therefore, 1024 coefficients with the highest values were extracted from each scale, selected equally from all orientations (shears), as in our case the frequency plan is divided into 5 scales, then the number of discriminating features will be 1024×5= 5120 features, divided as follows: from the first low pass scale, the highest

1024 features are extracted from scale as there are no oriented shears in this scale; from the second scale, the 1024 features are extracted from the 16 shears equally (1024 ÷ 16 = 64) features from each shear; the next scale with 32 oriented shears (1024 ÷ 32 = 32) features from each shear, and the last scale of 64 oriented shears a total of 16 features extracted from each shear.

Finally, the 5120 discriminating features are stored in a 1D feature vector for classification.

Curvelet Transform Complexity

The first generation Curvelet transform [104] suffers from high computational complexity and redundancy as it is based on Ridgelet transform. Candès et al. [105] introduced a new generation for Curvelet known as FDCT (Fast Discrete Curvelet Transform) with two implementations. The first one is based on unequally spaced fast Fourier transform (USFFT) and the second one is based on wrapping Fourier samples (I used the wrapping technique in my implementation). The two implementations are simpler and faster than the first generation and have $O(n^2 \log n)$ time complexity for an N x N array (Table 15).

Table 15 Running Time for Curvelet Transform via Wrapping

Size	Time (s)
256 × 256	2.34
512 × 512	4.17

Template Matching

We used L_0 distance to find the dissimilarities between two features sets of size 5120. The resultant distance will be in the range between 0-1, where 1 means no match and 0 means complete match. Thousands of experiments led us to use a threshold distance of 0.31 and 0.33 for UBIRIS.v1 and UBIRIS.v2 respectively, the distance threshold of 0.31 has the minimum FRR at zero FAR for UBIRIS.v1 and a distance threshold of 0.33 has the minimum FRR at 0.01 FAR for UBIRISv.2. If the distance of comparing two iris templates was less than the threshold, the two templates belong to the same iris (match), but if the distance was greater than the threshold, there will be no match.

Conclusion

In this chapter, the complete iris recognition framework proposed in this thesis is described, with experimental settings and results. The recognition system was tested on the whole UBIRISv.1 database (1877 images), and the result was FRR = 5.82% at FAR = 0%, and 1000 images randomly selected images from UBIRISv.2 and the result was FRR = 29.36 % at FAR = 1%.

Appendix B

Recently, a research paper about the stability of iris texture over years was published [106]. This paper criticizes the idea of iris texture stability on the basis of their experiments with three years' time interval. The authors found an increase of ~150% in the false rejection rate at a predefined decision threshold at one in two million false accept rate. Most of the researchers did their experiments on the free iris image databases, where different versions of iris images from the human subject have been captured in maximum three weeks' time intervals. Therefore, the recognition accuracies stated in this thesis as well as the results of the state-of-the-art methods does not count for iris textures variation over years.

A real world application of the iris recognition system at Dubai airport, from 2001 to 2013 with 1.5 trillion comparisons at zero false match as published by the UAE's Ministry of Interior on http://www.id.gov.ae/assets/eXQtYOeeFU.pdf.aspx, show that the system has been very robust over 12 years. Another remarkable success story is that of Afghani girl Sharbat Gula, when she was first photographed in a refugee camp in Pakistan during Soviet occupation by the National Geographic Network Photographer Steve McCurry (Figure 82).

Figure 82

The photograph was printed in 1985 on the cover page of National Geographic magazine, and it became a symbol for the Afghani conflict and the refugee situation worldwide. It was even linked to Leonardo Da Vinci's famous painting and called Afghan Mona Lisa. The photographer, with a search team from the National Geographic Network was trying to trace the Afghani girl without knowing her name or actual location as she was photographed in a refugee camp. During his search in Afghanistan many girls identified themselves falsely as the famous Afghan girl, but they were unable to identify the place where the photo was captured. In 2002, after the removal of the Taliban government, McCurry found a man who knew Gula's brother as he was in the same Pakistani camp 17 years earlier. When the team finally located Gula with the help of her brother, they met a mother of three children, aged 29 years. When McCurry first saw Shrbat Gula, he had doubts about her identity as her face details had become completely different (Figure 83).

To verify her claim, the National Geographic team sent both her photos to Prof. Daugman at the University of Cambridge. Daugman ran his iris recognition system [11] for both eyes and got a Hamming Distance of 0.24 for her left eye, and 0.31 for her right eye. This confirmed her identity after 17 years. This story proves that the human iris texture is stable over years and rules out any claims that say that the iris texture is not stable over years.

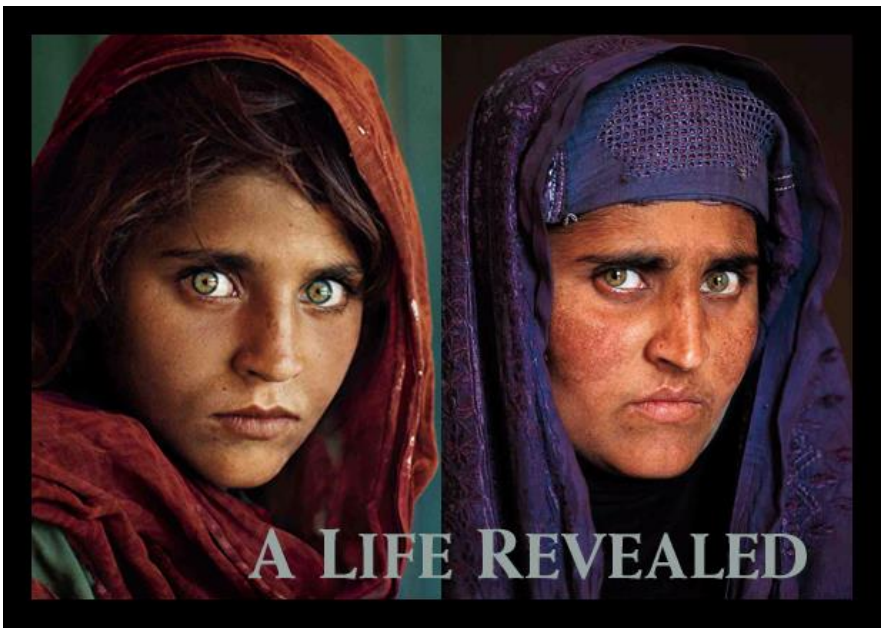

Figure 83

Appendix C

Segmentation

```
function Segmentation_23_9_2012()

clc;
clear all;
close all;

try

        close all
        i=108;
   % [file,path]=uigetfile('*.jpg;*.jpg');
filename=['1 (',num2str(i),').jpg'];
        set(gcf, 'Position', get(0, 'ScreenSize'));
        fontSize = 10;

         [Img storedColorMap] = imread(filename);
         subplot(2, 3, 1);

               imshow(Img);

        red=Img(:,:,1);
        green=Img(:,:,1);
        blue=Img(:,:,1);
       % imshow(red);
        Mask=(red>180 & green>180 & blue>180);

        structuringElement = strel('disk', 8);
     Mask = imclose(Mask, structuringElement);
 %       pause
%        return


         H_S_V = rgb2hsv(Img);
        hImage = H_S_V(:,:,1);
        sImage = H_S_V(:,:,2);
        vImage = H_S_V(:,:,3);
            Hue_Low = 0.2;
            Hue_High = .8;
            Saturation_Low = 0.0;
            Saturation_High = 0.5;
            Value_Low = 0.0;
            Value_High = 0.32;
        hueMask = (hImage >= Hue_Low) & (hImage <= Hue_High);
        saturationMask = (sImage >= Saturation_Low) & (sImage <=
Saturation_High);
        valueMask = (vImage >= Value_Low) & (vImage <= Value_High);
     Filter_Img = uint8(hueMask & saturationMask & valueMask);
```

```
      Filter_Img = cast(Filter_Img, class(Img));
       subplot(2, 3, 2);
        imshow(Filter_Img,[]);
      %imshow(Filter_Img,handles.axes3);


            Filter_Area = 1500;
      %  TheImageBeforeFilte=Filter_Img;
      Filter_Img = uint8(bwareaopen(Filter_Img, Filter_Area));
      structuringElement = strel('disk', 24);
      Filter_Img = imclose(Filter_Img, structuringElement);


        subplot(2, 3, 3);
        imshow(Filter_Img,[]);

      Filter_Img = uint8(imfill(Filter_Img, 'holes'));


         blobMeasurements = regionprops(Filter_Img, 'all');
        size1=size([blobMeasurements.Image]);

       xSize=size1(1);
       ySize=size1(2);
       if xSize >10 && ySize >10
          BlobAreas = [blobMeasurements.Area];
              BlobCenter=[blobMeasurements.Centroid];

              BlobRadius= sqrt((BlobAreas/pi));
              radiou=[BlobCenter(1)+BlobRadius,BlobCenter(2)];
              FpupilCenter= fix(BlobCenter);
             FPupilRadius=fix(BlobRadius);
              Filter_Img=addcircle(Filter_Img, FpupilCenter,
FPupilRadius);
                  Filter_Img = uint8(imfill(Filter_Img, 'holes'));

          Filter_Img = cast(Filter_Img, class(Img));
      masked = Filter_Img .* Img(:,:,1);
      maskedG = Filter_Img .* Img(:,:,2);
      maskedB = Filter_Img .* Img(:,:,3);
      maskedImg = cat(3, masked, maskedG, maskedB);


       x_axes=BlobCenter(1)+BlobRadius+20;
      x_axes = fix(x_axes);
      y_axes=fix(BlobCenter(2));

      [l w]=size(redMask)
while (redMask(y_axes,x_axes) >0)

          x_axes =x_axes+1;
end
```

```
outerCircle=PubpilSegcirclecrop(Img,BlobCenter(1),BlobCenter(2),x_a
xes,y_axes);

             red=outerCircle(:,:,1);

         redMask=(red<160);
        Filter_Img = uint8(imfill(redMask, 'holes'));

          Filter_Img = cast(Filter_Img, class(outerCircle));
      masked = Filter_Img .* outerCircle(:,:,1);
      maskedG = Filter_Img .* outerCircle(:,:,2);
      maskedB = Filter_Img .* outerCircle(:,:,3);
      maskedImg = cat(3, masked, maskedG, maskedB);


       red=maskedImg(:,:,1);
       % imshow(red);
         redMask=(red>80);
     Filter_Area = 2000;
     %   TheImageBeforeFilte=Filter_Img;
      Filter_Img = uint8(bwareaopen(redMask, Filter_Area));
      %  Filter_Img = uint8(bwareaopen(redMask, Filter_Area));
structuringElement = strel('disk', 8);
 Filter_Img = imclose(Filter_Img, structuringElement);
       Filter_Img = uint8(imfill(Filter_Img, 'holes'));


         irisMesurment = regionprops(Filter_Img, 'all');

         IrisArea = [irisMesurment.Area];
        %  blobMeasurements = regionprops(Filter_Img, 'all')
        %  if BlobAreas>10
              IrisCenter=[irisMesurment.Centroid];

              IrisRadius= sqrt((IrisArea/pi))
           %   radiou=[IrisCenter(1)+IrisRadius,IrisCenter(2)];
              FCenter= fix(IrisCenter);
             FIrisRadius=fix(IrisRadius)
         %     Filter_Img=addcircle(Filter_Img, FCenter,
IrisRadius);
                Filter_Img = uint8(imfill(Filter_Img, 'holes'));

  Filter_Img = cast(Filter_Img, class(maskedImg));
      masked = Filter_Img .* maskedImg(:,:,1);
      maskedG = Filter_Img .* maskedImg(:,:,2);
      maskedB = Filter_Img .* maskedImg(:,:,3);
      maskedImg = cat(3, masked, maskedG, maskedB);
        Iris_Circle_without_pupil=rgb2grey(maskedImg);
 Iris_Circle_without_pupil=double(Iris_Circle_without_pupil)
```

Normalization

For Daugman's Rubber Sheet Model matlab code download

http://www.csse.uwa.edu.au/~pk/studentprojects/libor/

Curvelet Features

For Curvelet full matlab code download http://www.curvelet.org/

Template Match

```
function ReadFromText2(temp)


for i=classno   % class
for n=1:1000    % img
try

res= fopen(['templete match\' num2str(i) '_1 (' num2str(n)
').jpg.txt'],'wt');
fid1=fopen(temp,'r');
   r1=textscan(fid1,'%n')
for j=1:22
    for k = 1:5
        try
        fid2=fopen(['curvelet\' num2str(j) '\1 (' num2str(k)
').jpg.txt'],'r');
        r2=textscan(fid2,'%n');


te1=(r1(:,:));

te2=(r2(:,:));

a=5120
```

```
diff = imabsdiff(te1,te2);
count=0;
for n =1:a
    if diff(n)<10
        count=count+1;
    end
end
count
count=count/a
count=1-count

if (count <0.33)
    clc
    fprintf('found    in class   : %d\n' , j);
    return
end
s=sum(diff);
s=s/a;
 diff= diff/a;
fprintf(res,'%d\n',count);
fclose (fid2);
        catch ME
        end
    end
end
clear n

clear diff
clear count
clear te2
fclose(res);
clear r2
clear res
 catch ME

end
```

```
end

end
end
```

ROC curve

Where D1 is the distance between the features of the iris compared with the whole database. D2 is the binary mask where 1 means the same human subject and 0 for the other subjects images.

```
xval=[0.001:0.01:1];

[FAR,Ver,T] = PERFCURVE(D2,1-D1,1,'XVals',xval);
R_FAR_Ver_T=[FAR';Ver';T'];

plot(T,Ver,'--rx');
xlabel('T');
ylabel('Ver');

figure,plot(T,FAR,'--rx');
xlabel('T');
ylabel('FAR');

figure,plot(FAR,Ver,'--rx');
xlabel('FAR');
ylabel('Ver');

[FAR,FNR,T] = PERFCURVE(D2,1-D1,1,'YCrit','FNR');

figure,plot(FNR,FAR,'--rx');
```

```
xlabel('FNR');
ylabel('FAR');

figure,plot(T,FNR,'--rx');
xlabel('T');
ylabel('FNR');

[FAR,FNR,T] = PERFCURVE(D2,1-D1,1,'XCrit','FNR','YCrit','FPR');
figure,plot(T,FNR,'--rx');
xlabel('FNR');
ylabel('FAR');
```

Appendix D

General Terminology in Image Processing

Histogram Equalization: is a process to adjust the pixels intensity over image to enhance the contrast. The process remaps the narrow tonal representation of pixels over the image to a wider representation of tones to enhance the separation between different tonal regions.

Image Binarisation: is a process of converting each pixel in a given image to one bit either 0 or 1 according to a particular threshold value, if the pixel value is grater that the threshold then convert to 1, otherwise convert to 0.

Dilation: is fundamental to morphological image processing. The dilation is an operation that thickens or grows the object element in a binary image. The grow process is controlled by the shape of the structuring elements as follows:

$$A \oplus B = \bigcup_{b \in B} A_b$$

where A is the image and B is the structuring element of A. If the structuring B has a centre point (Disk shape element) on the origin, the dilation process of A by B can be defined as thickening the points covered by B when the centre of B moves inside the border of image A.

Erosion: is fundamental to morphological image processing. The Erosion is an operation that shrinks the object element in a binary image. The shrink process is controlled by the shape of the structuring elements as follows:

$$A \ominus B = \bigcap_{b \in B} A_{-b}$$

where A is the image and B is the structuring element of A. If the structuring B has a centre point (Disk shape element) on the origin, the Erosion process of A by B can be defined as shrinking the points covered by B when the centre of B moves inside the border of image A.

Retinex Filter: stand for (Retina and Cortex) used to enhance images with poor brightness and illumination and make the images lighter. The method of Retinex mimic the human eye biological operation, where the camera devices fail to capture the small details in dark environments. More details on Retinex algorithm description in [39].